

Development and Applications of a Full-Stress Flowband
Model For Ice Using the Finite Volume Method

Stephen F. Price

A dissertation submitted in partial fulfillment of
the requirements for the degree of

Doctor of Philosophy

The University of Washington

2006

Program Authorized to Offer Degree: Earth and Space Sciences

University of Washington
Graduate School

This is to certify that I have examined this copy of a doctoral dissertation by

Stephen F. Price

and have found that it is complete and satisfactory in all respects,
and that any and all revisions required by the final
examining committee have been made.

Chair of the Supervisory Committee:

Howard B. Conway

Reading Committee:

Howard B. Conway

Charles F. Raymond

Edwin D. Waddington

Date: _____

In presenting this dissertation in partial fulfillment of the requirements for the doctoral degree at the University of Washington, I agree that the library shall make its copies freely available for inspection. I further agree that extensive copying of this thesis is allowable only for scholarly purposes, consistent with "fair use" as prescribed in the U.S. Copyright Law. Requests for copying or reproduction of this dissertation may be referred to ProQuest Information and Learning, 300 North Zeeb Road, Ann Arbor, MI 48106-1346, 1-800-521-0600, to whom the author has granted "the right to reproduce and sell (a) copies of the manuscript in microform and/or (b) printed copies of the manuscript made from microform."

Signature _____

Date _____

University of Washington

Abstract

Development and Applications of a Full-Stress Flowband
Model For Ice Using the Finite Volume Method

Stephen F. Price

Chair of the Supervisory Committee:
Professor Howard B. Conway
Earth and Space Sciences

A transient, two-dimensional, thermomechanical, ice-flow model is formulated in order to accurately model the flow field in regions of transitional flow, where all terms in the stress-equilibrium equations are important. The model solves the non-steady, advective-diffusive heat equation and the equations for ice flow in plane strain using the Finite Volume Method. A unique aspect of the model is the use of an orthogonal, curvilinear coordinate system, which simplifies discretization of the governing equations and the implementation of boundary conditions.

The model is applied to three different regions of transitional flow for which a full stress model is necessary to describe the flow field. In the first study, the flow and thickness history of Siple Dome, a local ice divide in West Antarctica, is constrained using forward modeling to match observations obtained near the dome summit. Results indicate that stable divide flow started 3 thousand years ago and that the dome thinned 350 meters from 15-14 thousand years ago. Thinning may have occurred in response to a period of rapid sea-level rise (meltwater pulse 1A) that occurred around the same time.

In the second study, the model is used to investigate how basal sliding, stresses in the ice, and frictional melting interact to allow a slow-to-fast sliding transition to migrate upstream over time. A positive feedback, which allows the transition to move tens of ice thicknesses upstream over short timescales (~10 years), is ultimately limited by topographic diffusion. The feedback also increases

the magnitude and upstream-propagation speed of perturbations to the ice thickness.

In the third study, the model is used to simulate the flow of Mount St. Helens crater glacier as it was squeezed between a newly expanding lava dome and the crater wall in early 2005. The glacier, which contains a large fraction of rock debris, was monitored extensively during the squeezing event. Those observations serve as targets for flow modeling in which the bulk-glacier density and the flow enhancement factor are treated as free parameters. Results indicate that ice containing 15-30% rock debris is between 5 and 10 times stiffer than clean glacier ice.

TABLE OF CONTENTS

	Page
List of Figures	v
List of Tables	vii
Chapter 1: Introduction	1
Background	1
Motivation and Goals	1
Organization	3
Chapter 2: A Full-Stress, Thermomechanical Flowband Model Using the Finite Volume Method Part I: Model Development and Validation	6
Summary	6
Introduction	6
Governing Equations	8
Conservation of momentum	8
Conservation of Energy	9
Constitutive relation	9
Boundary and Initial Conditions	11
Numerical Solution.....	14
Finite Volume Method	14
The pressure-correction method	18
General solution procedure	19
Orthogonal, Curvilinear Coordinate System.....	21
Initial coordinate system	22
The fundamental equation for orthogonal trajectories	23

Scale factors	25
Model Validation.....	27
Comparison to analytical solutions.....	27
Comparison to previous work	28
Conclusions	29

Chapter 3: A Full-Stress, Thermomechanical Flowband Model Using the Finite
Volume Method Part II: Application to the Flow and Thickness
History of Siple Dome, West Antarctica 44

Summary.....	44
Introduction.....	45
Previous Work.....	46
Modeling Approach.....	48
History of proximity to flow-divide.....	50
Ice-thickness history	52
Evolution of ice-flow enhancement.....	53
Divide scouring.....	55
Model Results and Sensitivity.....	56
Acceptable match.....	56
Sensitivity to the onset of divide-flow	57
Sensitivity to thickness change	58
Sensitivity to flow enhancement	59
Sensitivity to divide scouring	61
Sensitivity to accumulation-rate history.....	61
Discussion	61
Preferred history	61
Synthesis.....	64
Conclusions	66

Chapter 4: Upstream Propagation of Sliding Transitions: Feedbacks Between Sliding, Longitudinal-Stress Gradients, and Frictional Melting	80
Summary	80
Introduction	81
Flow Model	82
Model Description	82
General Solution Method	84
Basal Motion	85
Boundary Conditions, Initial Conditions, and Assumptions	87
Perturbing the Equilibrium Models	88
Results	89
Discussion	90
Evolution of Geometry and Stress Fields: Reference Model	90
Evolution of Melting Rate: Reference Model	92
Evolution of Geometry and Stress Fields: Linked Model	93
Evolution of Melting Rate: Linked Model	95
Evolution of Melting Rate: All Models	95
Large-Scale Model Response	97
Synthesis	98
Conclusions	103
 Chapter 5: Modeling the Dynamic Response of a Crater Glacier to Lava-Dome Emplacement: Mt. St. Helens, Washington, U.S.A.	 117
Summmary	117
Introduction	118
Field Setting	119

Flow Model.....	120
Model description	120
General solution method	122
Changes in flowband width	123
Resistance from valley sidewalls	124
Initial conditions	125
Boundary conditions	126
Other observational constraints	127
Results	128
Discussion.....	131
Conclusions.....	132
Chapter 6: Conclusions	141
References	149
Appendix A: Discrete, Orthogonal, Curvilinear Coordinate System	160
Appendix B: Non-Steady and Advective Terms	167
Appendix C: Pressure-Correction Method	172
Appendix D: Flowband Adaptation	179
Appendix F: Uncertainty in Surface Temperature History at Siple Dome and the Resulting Uncertainty in Modeled Temperatures	181

LIST OF FIGURES

Figure Number	Page
2.1 Staggered grid used in heat and momentum balance models	31
2.2 Finite volume centered at P and neighboring volumes	32
2.3 Curves of constant \hat{z} in (x,z) space.	33
2.4 Final grid of (\hat{x},\hat{z}) coordinate curves in (x,z) space	34
2.5 Variables involved in calculation of coordinate system	35
2.6 Final grid of (\hat{x},\hat{z}) coordinate curves in (\hat{x},\hat{z}) space	36
2.7 Definition of variables needed for calculation of the scale factor $h_{\hat{x}}$	37
2.8 Comparison of analytically and numerically calculated velocity fields.....	38
2.9 Modeled velocity shape functions at a flow divide	39
3.1 Siple Dome location map	67
3.2 Surface temperature and accumulation-rate histories for Siple Dome	68
3.3 Modeled (lines) and observed (dots) variables at the Siple Dome core site.....	69
3.4 Map showing the favored value of the present-day enhancement factor	70
3.5 Velocity shape functions at Siple Dome divide	71
3.6 Map of flow enhancement at Siple Dome over time	72
3.7 Model sensitivity to starting time of divide-flow	73
3.8 Model sensitivity to magnitude of ice-thickness change	74
3.9 Model sensitivity to timing of ice-thickness change	75
3.10 Model sensitivity to flow enhancement	76
3.11 Model sensitivity to timing of flow enhancement	77
3.12 Model sensitivity to the rate of divide scouring	78
3.13 Model sensitivity to the accumulation-rate history	79
4.1 Shear strain-rate versus shear stress in basal layer	105
4.2 Softness parameter as a function of frictional melting rate	106
4.3 Time series of the longitudinal-stress gradients for the reference model	107
4.4 Stress balance and melting rate for the reference model	108
4.5 Evolution of the melting rate for the reference and linked models	109

4.6	Time series of longitudinal-stress gradients for the linked model	110
4.7	Stress balance and melting rate for the linked model	111
4.8	Temporal evolution of the melting rate for all models	112
4.9	Shift of melt-rate profile after a perturbation to the melting rate	113
4.10	Thinning rate as a function of time upstream from the perturbation	114
4.11	Relative magnitude and timing of thinning for reference and linked models	115
4.12	Thinning rate as a function of distance upstream from the perturbation	116
5.1	Field setting of Mount St. Helens crater glacier	133
5.2	Horizontal speed of east crater glacier GPS stations	134
5.3	Surface elevation profiles along the glacier centerline in Figure 1.....	135
5.4	Model-observation elevation misfit for various models on all days.....	136
5.5	Model fit to observed horizontal velocities at ELE4	137
5.6	Misfit between modeled and observed elevations on day 193	138
5.7	Model fit to observed surface elevations	139
5.8	Horizontal velocity, strain rate, and stress on day 50 (21, February 2005)	140
A.1	Illustration of discrete orthogonality at interface $(x,z)_{i,j}$	165
A.2	Section of a curvilinear grid demonstrating integration procedure.....	166

LIST OF TABLES

Table Number	Page
2.1 Variables used in heat and momentum balance models	40
2.2 Constants and other model parameters	42
2.3 Variables used when creating orthogonal, curvilinear-coordinate system	43

ACKNOWLEDGEMENTS

This dissertation would not have been possible without the help of many people on both the professional and personal sides of my life. On the professional side, I would especially like to thank Howard (Twit) Conway and Ed Waddington who have been involved with all aspects of this work and who worked hard to help bring me to the University of Washington in the first place. I thank Twit for his encouragement, support, help with writing and organization, and for being an endless source of good ideas and background material, many of which have helped to provide context and relevance for this work. I thank Ed for getting me started with flow modeling, for his continued help in developing my flow model, and for help clarifying my thinking on many topics over the past few years. His meticulous attention to details greatly improved the writing in this dissertation. I also want to thank Charlie Raymond. His comments and suggestions during numerous discussions have helped to clarify the thinking and interpretation of many different topics I've worked on over the past few years. His work on the energy balance of ice streams served as an inspiration for the work in Chapter 4 of this dissertation. My old colleagues at NASA Goddard Space Flight Center, Bob Bindschadler and Christina Hulbe, also deserve special thanks for their contributions to early work that is further developed here and for offering opportunities, support, and encouragement for my graduate and post-graduate career. I am very thankful to them for the interest they have taken in my career and the input they have provided over the years. My entire committee, Howard Conway, Ed Waddington, Ron Merrill, Bob Bindschadler, Charlie Raymond, and Cecelia Bitz also deserve special thanks for accommodating my somewhat rushed schedule during my last few months of school.

The work on Siple Dome, presented in Chapter 3, is guided in part by the previous contributions of my University of Washington coauthors and by the work of previous University of Washington glaciology students. In particular, I relied heavily on the work of Nadine Nereson (Ph.D. 1998) and Erin Pettit (Ph.D. 2003).

Over the years, my officemates and fellow glaciology graduate students have provided much in the way of support, camaraderie, and commiseration. Among them, I would like to thank Bob Hawley, Michelle Koutnik, Joe MacGregor, Lars Karloff, Hans Christian Steen-Larsen, Throstur Thorsteinsson, and fellow 7th floor glaciology students Ginny Catania, Ben Smith and Erin Pettit. I would also like to thank Tom Neumann for helping me debug my heat balance model and for many helpful discussions over the past few years about modeling in general. I also thank Al Rasmussen, Kenichi Matsuoka, Ian Joughin, Dale Winebrenner, Steve Warren, Bernard Hallet, and Eric Steig for their support and input over the past few years.

Outside of the University of Washington community, I would like to thank Matt Spencer and Richard Alley from Penn State and Annie Schilla and Jim White from The University of Colorado. In addition to providing the accumulation rate and surface temperature histories that are a crucial part of the work on Siple Dome, they contributed greatly to this work with helpful discussions during emails too numerous to count. I thank them for sharing their data and their ideas with me. Thanks also to Joe Walder from the USGS Cascades Volcano Observatory for the opportunity to work with him on the modeling of Mount St. Helens glacier. As with my other co-authors, I learned a lot about writing, organization, context, and presentation from Joe. On the practical side of things, Christina Hulbe and Mike Price deserve a special note of thanks for providing me with computer time when it was desperately needed.

While at the University of Washington, I have been lucky to have a large network of family and friends. I would like to thank everyone in Portland, Bellingham, Olympia, Seattle, Everett, Bend, Orcas Island, and Anchorage for their support. I would especially like to thank my parents, my brothers and sister, and my relatives in Washington D.C for their support and encouragement during my time in and out of graduate school over the last ten years. Steve and Noel Nelson deserve special thanks for all their help during the past year while Aimee and I

finished graduate school and welcomed a new baby into our lives. We couldn't have done it without their help.

Finally, I want to thank my wife Aimee for her support, encouragement, love, patience, and understanding over the past five years and especially over the past six months. I can't imagine how different my time in Washington would have been without her optimism, bad jokes, love, and friendship. I also thank Maya for opening my eyes again to all the interesting things in life that we take for granted as adults, like dandelions, flies in the window, balloons, and airplanes.

This work was supported by NSF grants OPP-0125610 and OPP-0087345.

DEDICATION

For Aimee and Maya

INTRODUCTION

Background

While the systems of equations describing the controls on the earth's climate system – conservation of mass, energy, and momentum – are readily derived from first principles, they may be difficult or impossible to solve analytically, particularly at the level of individual processes. Numerical-modeling techniques have improved our ability to solve these difficult problems without greatly oversimplifying them. With vast increases in computing power, speed, and accessibility over the last forty years, computer modeling has emerged as one of the most powerful tools for studying the earth's climate system.

This generalization applies to studies of the cryosphere, and, in particular, to the field of glaciology. One aspect of glaciology is the study of how glaciers react to changes in their boundary conditions, for example increases in air temperature or changes in sea level. Because glacier ice can be treated as an incompressible fluid, its behavior is readily described by well-known principles of continuum and fluid mechanics. In turn, computer modeling and numerical techniques are ideal tools with which to solve the governing equations that describe fluid flow and heat transfer within a glacier without reverting to oversimplifications that would cause one to miss, or misunderstand, important physical processes.

Motivation and Goals

The broad motivation for this work is to study a range of glaciological problems for which often-neglected terms in the stress-equilibrium equations, in particular longitudinal stresses, are of particular importance. A common simplification applied to ice-flow modeling is the “shallow-ice approximation” (Hutter, 1983), which follows from the observation that, in many regions of an ice sheet or glacier, velocity and stress gradients are orders of magnitude larger in the vertical direction

(perpendicular to the glacier bed) than in the horizontal direction (along or across-flow). For flow in a vertical slice through the ice sheet, this simplification allows one to solve for the horizontal velocity field by considering only two terms in the stress-equilibrium equations, the driving stress (the downslope-oriented fraction of the ice overburden) and the basal-shear stress, which is assumed to oppose all of the driving stress. From the incompressibility condition, one can then derive the vertical-velocity field and, having both components of the velocity field, one can predict the change in surface shape at some future time step. In turn, by successively predicting the glacier surface shape at future time steps, one can study evolution of a glacier under some set of boundary conditions.

Unfortunately this modeling scheme will provide inaccurate results (i.e. inaccurate velocity fields, and thus inaccurate glacier evolution) for any region of an ice sheet or glacier in which other terms in the stress-equilibrium equations are important. This negates the use of such models for studying portions of an ice sheet or glacier that are often the most interesting, for example at ice divides, at sliding-no-sliding transitions, or in any region where along- or across-flow gradients in ice speed are significant over distances comparable to the ice thickness. For this reason, the current trend in ice-flow modeling (see review paper by Alley and others, 2005) is towards the development and application of full-stress models.

The first goal of this dissertation is to develop a new, two-dimensional, thermo-mechanical flow model that does not make common simplifying assumptions with respect to the governing equations: the model should solve the full, two-dimensional momentum equations describing ice flow in plane strain. It should also include terms to account for the effects of converging or diverging flow. The second goal of this dissertation is to apply that model to a number of glaciological problems that could not (or rather should not) be approached using more simple flow models.

Organization

This dissertation is organized in the form of six chapters. Chapter 1 provides introductory material, Chapters 2 through 5 are written as complete manuscripts to be submitted for publication, and Chapter 6 provides a review of overall conclusions and prospects for future work. The flow model is developed in Chapter 2 and then applied to three different studies in Chapters 3, 4, and 5. For all of these studies, a more simple flow model would be inappropriate. All chapters in manuscript form are written with coauthors from The University of Washington and/or from other external institutions (the “we” referred to below).

Chapter 2 describes the construction and validation of the new flow model. Like other two-dimensional, full-stress flow models (e.g. Hvidberg, 1996), the model consists of three interacting submodels: (1) a heat-balance model, (2) a stress-balance model, and (3) a surface-evolution model. The first solves the non-steady, two-dimensional, advective-diffusive heat equation to determine the ice temperature, the second solves the stress-equilibrium equations for a power-law viscous, low-Reynolds number fluid to determine the two-dimensional velocity field, and the third predicts changes in the domain geometry based on evolution of the free surface. Unlike previous models, this model solves the heat and momentum balance equations using the “Control Volume Method” (Patankar, 1980), or the “Finite Volume Method” (FVM; Versteeg and Malalasekera, 1995). The FVM, somewhat intermediate to the Finite Difference and Finite Element Methods, is suitable for numerically solving many types of conservation equations (e.g. the heat-balance equation and the stress-equilibrium equations) in their generic form, that is, without resorting to simplification. At the time of this writing, no known previous authors have employed this method of ice flow modeling, making this effort unique. Also unique is the use of a curvilinear, orthogonal coordinate system that simplifies both the discretization of the governing equations and the implementation of boundary conditions. A significant portion of the background material on model development is presented here as appendices. When Chapter 2 is submitted as a manuscript, that same material will also be included as appendices.

Chapter 3 is intended as a companion paper to Chapter 2 and a first application of the new flow model. In Chapter 3, we use the model to constrain the flow and thickness history of Siple Dome, a local ice dome and inter-ice-stream ridge in West Antarctica. Our approach is to simultaneously match numerous observational datasets from the dome using forward modeling in which we vary key physical processes within the model. Flow models that employ the shallow-ice approximation fail near a flow divide because the surface slope, and thus the driving stress, approach zero. As a result, the stress-equilibrium equations are dominated by longitudinal stresses and a full-stress flow model is needed to accurately model the flow field near a divide. The full-stress nature of the new flow model then becomes crucial to the interpretation presented here. In addition, the thermo-mechanical nature of the model proves crucial; a key, diagnostic constraint on the timing and magnitude of thinning at Siple Dome comes from matching the temperature profile measured in the borehole near the divide.

In Chapter 4, we use the new model to investigate a very different type of problem, one involving fast flow through basal sliding. In regions where the sliding speed changes from slow to fast along flow, there is the potential for a positive feedback between longitudinal-stress gradients, basal sliding, and frictional melting. This feedback could allow slow-to-fast sliding transition regions, such as those that occur at the heads of ice streams and outlet glaciers, to migrate upstream over time. This topic is of considerable interest because the headward growth of an ice stream or outlet glacier increases its ability to draw down the interior regions of an ice sheet. We use the model to gain insight into how such sliding transitions might change over time as a result of this feedback and what physical processes control and limit the feedback. We also make predictions for how the timescale for the upstream propagation of perturbations is affected by this feedback, relative to flow models that account for the inland propagation of perturbations through the mass and stress balance alone. Interestingly, the two seemingly unrelated topics discussed in this chapter and in Chapter 3 share some common ground in their

conclusions. Again, because of the central importance of longitudinal stresses, the full-stress nature of the new flow model makes this study possible.

Chapter 5 focuses on a unique and timely glaciological problem that is, at first glance, somewhat of a novelty. In late 2004, volcanic activity in the Mount St. Helens crater resumed, and a new lava dome began growing. A horseshoe-shaped glacier, which began forming in the volcano crater after the 1986 eruption, was quickly split in two by the newly expanding lava dome. From early- to mid-2005, the dome continued to grow eastward, squeezing the eastern half of the glacier against the crater wall like a vice. The U.S. Geological Survey Cascades Volcano Observatory closely monitored the glacier during this time. Observations indicate that the squeezing event induced very large normal strain rates in the glacier, both along and across flow, so that simplified flow models would not accurately describe evolution of the glacier during the squeezing event. The glacier is composed of a mixture of ice and rock debris, the volume fraction of which is constrained by observations. We use the new flow model, data from the squeezing event, and observations on the debris content of the glacier to reproduce the glacier's response during the squeezing event. In doing so, we place bounds on the enhancement factor required to match observations of the glacier's evolution. An important distinction between this work and laboratory studies of the deformation of debris-laden ice is that the latter is limited to silt- and sand-sized debris. Because we use an actual glacier with a more realistic distribution of debris sizes (from silt- and sand-sized grains up to large boulders), our inferred rheological parameters are likely to be more representative of debris-laden ice in a natural setting.

**A FULL-STRESS, THERMOMECHANICAL FLOWBAND MODEL
USING THE FINITE VOLUME METHOD PART I:
MODEL DEVELOPMENT AND VALIDATION**

Portions of the material in this chapter were originally presented as posters at the 10th annual WAIS workshop held in Sterling, VA, on September 20-23, 2003 and at the AGU-CGU joint meeting held in Montreal, Canada, on May 17-21, 2004. This chapter is a draft for the first part of a two-part manuscript with University of Washington co-authors E.D. Waddington and H. Conway.

SUMMARY

A thermomechanical ice-flow model is formulated using the Finite Volume Method. Separate submodels solve for the full, 2-dimensional momentum equations, the advective-diffusive heat equation, and evolution of the free surface. A unique aspect of the method is the use of a boundary fitted, orthogonal, curvilinear-coordinate system, which simplifies the implementation of boundary conditions, leads to a straightforward discretization scheme, and results in banded sparse-coefficient matrices that can be inverted directly, rather than through iterative methods. For simple boundary conditions and geometries, the model output compares well with analytical solutions. For more complicated boundary conditions and geometries, the model output compares well with full-stress solutions obtained by previous authors.

INTRODUCTION

When modeling the flow of large ice masses, a number of simplifications are often employed. The most common of these is the so-called “shallow-ice”

approximation; the effects of horizontal-stress gradients are ignored under the assumption that the thickness of the ice sheet, H , is small compared to its lateral extent, L (e.g. Fowler and Larson, 1978; Hutter, 1981). This approximation is valid for portions of the ice sheet that deform primarily through simple shear but not for regions of transitional flow, where additional components of the stress tensor contribute significantly (or dominantly) to the deformation. Regions in an ice sheet where longitudinal stress gradients are particularly important include ice divides (Raymond, 1983), areas where basal relief varies significantly over distances of order H (Budd 1970a, 1970b; Whillans and Johnsen, 1983), and the tributary regions upstream from the ice streams (Price and others, 2002).

Previous authors have used both Finite-Difference and Finite-Element Methods (FDM and FEM, respectively) to construct two-dimensional (2D), full-stress or “higher-order” flow models, which account for terms in the 2D momentum equations that shallow-ice models omit (Raymond, 1983; Hvidberg, 1996; Pattyn, 2002). The Finite-Volume Method (FVM; also referred to as the “control volume method” (Patankar, 1980; Versteeg and Malalasekera, 1995)) is another generally applicable method for solving the full, 2D momentum equations without resorting to higher-order approximations. To our knowledge, it has not been previously applied to ice flow. Here, we use the FVM to formulate a new, time-dependent, thermomechanical flowband model in orthogonal, curvilinear coordinates. We first present the governing equations and the solution method. We then briefly discuss the construction and application of the coordinate system. Simple domain geometries and boundary conditions are then used to test the model output against analytical solutions. For more complicated geometries and boundary conditions we compare the model output with the work of previous authors. In part II of this paper (Chapter 3), we apply the model to Siple Dome, a well-studied interstream ridge in West Antarctica. In that paper, our goal is to better constrain its flow and thickness history over the last ~40 ka.

GOVERNING EQUATIONS

Conservation of momentum

Consider a Cartesian coordinate system with the x -axis oriented along-flow, the y -axis oriented across flow, and the z -axis vertical and perpendicular to the other two. Conservation of linear momentum along the coordinate direction x_i is expressed by

$$\frac{\partial(\rho u_i)}{\partial t} + u_j \frac{\partial(\rho u_i)}{\partial x_j} = \frac{\partial}{\partial x_j} \left(\eta \frac{\partial u_i}{\partial x_j} \right) - \frac{\partial P}{\partial x_i} + \rho g_i \quad (i = x, y, z), \quad (2.1)$$

(summation over repeat indices is implied in Equation (2.1) and for the remainder of the paper) where u_i are the components of the velocity vector in the coordinate directions x , y , and z , P is the mean-compressive stress, ρ is the fluid density, η is the effective viscosity, and g is the acceleration due to gravity.

For ice flow, accelerations are generally assumed negligible and the Reynolds number is on the order of $\sim 10^{-16}$. In this case, the non-steady and advective terms on the left-hand side of Equation (2.1) are ~ 0 giving

$$0 = \frac{\partial}{\partial x_j} \left(\eta \frac{\partial u_i}{\partial x_j} \right) - \frac{\partial P}{\partial x_i} + \rho g_i. \quad (2.2)$$

The incompressibility condition is

$$\frac{\partial u_i}{\partial x_i} = 0. \quad (2.3)$$

For flow in plane strain, Equation (2.2) gives expressions for the along-flow component of velocity, u , and the vertical component of velocity, w . These two

scalar equations, along with the two-dimensional incompressibility condition, are used to solve for the horizontal and vertical velocity fields and the unknown pressure field. We discuss the solution procedure below and in further detail in Appendix C.

Conservation of energy

Conservation of energy is expressed by the non-steady, advective-diffusive heat equation,

$$\frac{\partial \theta}{\partial t} + u_i \frac{\partial \theta}{\partial x_i} = \frac{1}{\rho C} \frac{\partial}{\partial x_i} \left(k \frac{\partial \theta}{\partial x_i} \right) + \frac{\sigma_{ij} \dot{\epsilon}_{ij}}{\rho C}, \quad (2.4)$$

where the density for ice is assumed constant. In Equation (2.4), θ represents the ice temperature and $C(\theta)$ and $k(\theta)$ represent the specific heat and thermal conductivity, respectively. The left-hand side of Equation (2.4) accounts for non-steady and advective terms. The right-hand side accounts for the diffusive and internal source terms.

Constitutive relation

A generally used constitutive relation for ice is Nye's generalization of Glen's flow law (Nye, 1957),

$$\tau_{ij} = B(\theta) \dot{\epsilon}_e^{\frac{1-n}{n}} \dot{\epsilon}_{ij}, \quad (2.5)$$

where τ_{ij} is the deviatoric-stress tensor, $\dot{\epsilon}_e$ is the strain-rate tensor, and $B(\theta) = A(\theta)^{1/n}$ is the inverse rate factor. The rate factor, $A(\theta)$, follows an Arrhenius relation for temperatures more than about 10°C below the melting point, $A(\theta) = A_0 \exp\left(-\frac{Q}{R\theta}\right)$

(Paterson, 1994, p. 91). The flow-law exponent, n , is usually taken to be 3. The effective strain rate, $\dot{\epsilon}_e$, is related to the second invariant of the strain-rate tensor

$$2\dot{\epsilon}_e^2 = \dot{\epsilon}_{ij}\dot{\epsilon}_{ij}, \quad (2.6)$$

for which individual strain-rate components are given by

$$\dot{\epsilon}_{ij} = \frac{1}{2} \left(\frac{\partial u_i}{\partial x_j} + \frac{\partial u_j}{\partial x_i} \right). \quad (2.7)$$

The deviatoric-stress is given by the full stress minus the mean-normal stress,

$$\tau_{ij} = \sigma_{ij} - \frac{1}{3} \sigma_{kk} \delta_{ij} = \sigma_{ij} + P \delta_{ij}, \quad (2.8)$$

where δ_{ij} is the Krönecker delta (or identity matrix) and P is defined as the mean normal compressive stress.

Equation (2.5) can also be written in the more general form,

$$\tau_{ij} = 2\eta \dot{\epsilon}_{ij}, \quad (2.9)$$

where

$$\eta = \frac{1}{2} B(\theta) \dot{\epsilon}_e^{\frac{1-n}{n}} \quad (2.10)$$

is the temperature and strain-rate dependent effective viscosity (A list of variables used in formulation and solution of the heat and momentum balance models is given in Table 2.1).

BOUNDARY AND INITIAL CONDITIONS

The heat- and momentum- balance equations are parabolic and elliptic, respectively, in which case the normal gradient or the value of u , w , and θ must be specified at each boundary. Where stress is specified at a boundary, the traction vector must be continuous and the normal and tangential gradients in u (or w) must be specified along with the pressure. The heat balance equation also requires an initial condition.

Our model employs an orthogonal, curvilinear, boundary-fitted coordinate system in which coordinate directions are exactly parallel and perpendicular to domain boundaries (the coordinate system is discussed further below and in Appendix A). As a result, cross terms do not arise in the expressions for the boundary conditions, simplifying their numerical implementation.

The upper surface experiences atmospheric pressure. Wind stress is assumed negligible. Continuity of the traction vector, T_i , across the interface is expressed by

$$T_i = \sigma_{ij}n_j = (\tau_{ij} - P\delta_{ij})n_j = -P_{atm}n_i \quad (2.11)$$

where P_{atm} is the atmospheric pressure and n_i are the components of the surface normal vector (surface tension is neglected). For a boundary-fitted coordinate system, $n_i=[0,1]^T$ on the upper surface and Equation (2.11) gives

$$\tau_{zx} = 2\eta\dot{\epsilon}_{zx} = \eta\left(\frac{\partial u}{\partial z} + \frac{\partial w}{\partial x}\right) = 0 \quad (2.12)$$

and

$$\tau_{zz} = 2\eta\dot{\epsilon}_{zz} = 2\eta\frac{\partial w}{\partial z} = P - P_{atm}. \quad (2.13)$$

Equations (2.12) and (2.13) provide boundary conditions for the surface-normal and tangential velocity gradients,

$$\left. \frac{\partial u}{\partial z} \right|_{sfc} = - \left. \frac{\partial w}{\partial x} \right|_{sfc} \quad (2.14),$$

and

$$\left. \frac{\partial w}{\partial z} \right|_{sfc} = \frac{P_{sfc} - P_{atm}}{2\eta_{sfc}} \quad (2.15),$$

and for the mean compressive stress at the interface,

$$P_{sfc} = 2\eta \left. \frac{\partial w}{\partial z} \right|_{sfc} + P_{atm}. \quad (2.16)$$

At the lower boundary we specify $u=w=0$ (i.e. ice frozen to the bed).

At the domain sides, the boundary-normal component of velocity, and thus the flux, is specified through a shape function, $\chi(z)$. In steady state, the balance flux from the flow divide ($x=0, u=0$) to the “eastern” boundary is given by

$$u(z)_e = \bar{u}_e \chi(z), \quad (2.17)$$

where the column-averaged velocity, \bar{u}_e , is given by

$$\bar{u}_e = \frac{1}{H_e} \int_0^e b(x) dx. \quad (2.18)$$

H_e is the ice thickness at $x=e$, the position of the eastern boundary. For the initial solution, $\phi(z)$ is a modified form of the standard, isothermal shape function (e.g. Raymond, 1983; Hvidberg, 1996) that gives a velocity profile more appropriate for

a polar glacier. Once a converged velocity solution has been found using an initial estimate for $\chi(z)$, $\chi(z)$ is re-calculated from a velocity profile several ice-thicknesses inside of the domain. To ensure that the representation of the flow field at a lateral boundary does not affect the solution, domain boundaries are extended ~ 20 ice thicknesses past the area of interest within the domain.

For heat-balance calculations, the temperature gradient at the base of a bedrock layer beneath the ice is specified according to

$$\frac{\partial \theta}{\partial z} = -\frac{Q_{geo}}{k_r}, \quad (2.19)$$

where θ is the temperature, Q_{geo} is the geothermal flux, and k_r is the thermal conductivity at the base of the bedrock layer. Here, we take Q_{geo} and k_r as constant in time. At the surface, temperature is specified as a function of time and distance along flow,

$$\theta_s = \theta_s(x, t). \quad (2.20)$$

If temperature at the ice-bed interface reaches the pressure-melting point, the fraction of Q required to maintain pressure-melting is conducted upwards into the ice. Any geothermal flux in excess of this leads to basal melting, at which point the vertical velocity at the bed is set to the melting rate. At the lateral boundaries, the advective-heat flux is orders of magnitude larger than the diffusive-heat flux, which is set to zero. An initial temperature field in the ice is specified using the analytical solution for steady-state flow at an ice divide (Hooke, 1998, p. 72, Equation (2.6.24)). The geothermal flux and bedrock conductivity are used to extrapolate basal temperatures into the bedrock layer by assuming steady-state temperatures there. All of the boundary conditions described above are implemented numerically using methods similar to those described in Versteeg and Malalasekera (1995).

Initial viscosity and velocity fields are derived using reasonable approximations. The initial temperature field determines an initial rate-factor field, from which the vertical shearing rate, $\frac{\partial u}{\partial z}$, is calculated using the laminar flow approximation (Hooke, 1998, p. 49, Equation 5.4). The horizontal velocity field is obtained by integrating the vertical shearing rate from the bed to the surface, explicitly accounting for higher shearing rates near the bed due to warm, soft ice. The initial vertical velocity field is then estimated from continuity. An initial value for the effective viscosity is calculated based on the initial rate-factor field and a characteristic value for the effective strain rate ($\sim 10^{-3}$ - 10^{-4} a $^{-1}$).

NUMERICAL SOLUTION

Finite Volume Method

The governing equations are solved using the Finite Volume Method (FVM), which is particularly well suited to solving flow problems in which several or all terms in the stress equilibrium equations are important. We discuss the FVM briefly below and in greater detail in Appendices C and D. Complete descriptions are given in texts by Patankar (1980) and Versteeg and Malalasekera (1995).

Like the FDM, the FVM solves the governing equations on a structured grid. Like the FEM, the FVM solves the integral (or “weak”) form of the governing equations, and so lends itself naturally to non-uniform grid spacing. A restriction to the method is that the grid must be orthogonal and, for the purposes of illustration, we initially assume a rectangular domain in Cartesian coordinates (below, we extend the method to arbitrarily shaped domains in orthogonal, curvilinear coordinates). To avoid “checkerboard” pressure and velocity solutions, the grid is staggered: u and w calculation volumes are offset one-half grid space from P and θ calculation volumes (Figure 2.1).

Both of the governing conservation equations considered here (Equations (2.1) and (2.4)) can be written in the more general form,

$$\frac{\partial(\rho\phi)}{\partial t} + u_i \frac{\partial(\rho\phi)}{\partial x_i} = \frac{\partial}{\partial x_i} \left(\Gamma \frac{\partial\phi}{\partial x_i} \right) + S, \quad (2.21)$$

which is a non-steady, advective-diffusive conservation equation for the scalar variable ϕ with source term S and conductivity Γ . Equation (2.21) is the general form of the partial-differential equation solved by the FVM. If we equate the scalar variable ϕ in Equation (2.21) to the horizontal component of velocity, u , the conductivity with the effective viscosity, η , and the source term with the last two terms on the RHS of Equation (2.2), we obtain an equation for the conservation of linear momentum in the x direction (i.e. Equation (2.2) in which the imbalance between the pressure gradient and body force define the source term). Integrating this equation over the quadrilateral volume in Figure 2.2 we obtain

$$\eta_e \frac{\partial u}{\partial x} \Big|_e \Delta z_p - \eta_w \frac{\partial u}{\partial x} \Big|_w \Delta z_p + \eta_u \frac{\partial u}{\partial z} \Big|_u \Delta x_p - \eta_d \frac{\partial u}{\partial z} \Big|_d \Delta x_p + S_{Int} = 0. \quad (2.22)$$

In Equation (2.22) and below subscripts E , W , U , and D refer to values at *volume centers* adjacent to the volume centered at P . Likewise, subscripts e , w , u , and d refer to values at adjacent *interface centers* (Figure 2.2). An important point to note is that, in its integrated form, our governing equation no longer requires the assumption of a constant effective viscosity.

The momentum source term in Equation (2.22) is the integrated imbalance between pressure gradients and the body force acting in the x direction,

$$S_{Int} = -(P_e - P_w) \Delta z_p + \bar{B}_x \Delta x_p \Delta z_p, \quad (2.23)$$

where $\overline{B}_x = \rho g_x$ is the mean body force acting over the u calculation volume with center (x_P, z_P) . P_e and P_w refer to the pressures at the east and west *interfaces* of this u calculation volume, which are the centers of adjacent P and T calculation volumes (Figures 2.1 and 2.2). For the moment, we take these pressures to be known. We discuss their calculation below.

Equations (2.22) and (2.23) express the balance of momentum fluxes across the east and west interfaces of the volume centered at (x_P, z_P) . To proceed further, we must specify how the interface gradients in u will be approximated. A convenient property of an orthogonal-coordinate system is that these gradients can be quantified using piecewise-linear profiles and the values of u in the neighboring volumes directly to the east (U_E), west (U_W), above (U_U), and below (U_D) (without an orthogonal-coordinate system, additional cross terms would be required to quantify the gradients). In this case, Equation (2.22) becomes

$$\eta_e \left(\frac{u_E - u_P}{\delta x_e} \right) \Delta z_P - \eta_w \left(\frac{u_P - u_W}{\delta x_w} \right) \Delta z_P + \eta_u \left(\frac{u_U - u_P}{\delta z_u} \right) \Delta x_P - \eta_d \left(\frac{u_U - u_P}{\delta z_u} \right) \Delta x_P + S_{int} = 0, \quad (2.24)$$

in which the values of δx and δz are defined in Figure 2.2.

From Equation (2.24), we define the following coefficients:

$$a_E = \frac{\eta_e \Delta z_P}{\delta x_e}, \quad a_W = \frac{\eta_w \Delta z_P}{\delta x_w}, \quad a_U = \frac{\eta_u \Delta x_P}{\delta z_u},$$

$$a_D = \frac{\eta_d \Delta x_P}{\delta z_d}, \quad a_P = a_E + a_W + a_U + a_D. \quad (2.25, \text{a-e})$$

The interface viscosities in Equation (2.25), η_u , η_d , η_e , and η_w are analogous to the interface thermal conductivities, k , in the discretized form of the heat Equation (2. and the interface conductivities, Γ , in the discretized form of the general equation). In general, the interface “conductivity” (η , k , or Γ) may be a function of

the dependent variable (e.g. $\eta(u)$, $k(\theta)$, $\Gamma(\phi)$), which is calculated at volume centers and assumed to prevail over its entirety. For two neighboring volumes with differing conductivities, the correct interface conductivity (the one resulting in the appropriate boundary flux) is given by the *harmonic* (rather than the *arithmetic*) mean of conductivities at adjacent volume centers (Patankar, 1980). The viscosity at interface e is then given by

$$\eta_e = \left[\alpha \eta_E^{-1} + (1 - \alpha) \eta_P^{-1} \right]^{-1}, \quad (2.26)$$

where $0 \leq \alpha \leq 1$ is a weighting factor given by

$$\alpha = \frac{\delta x_{e-}}{\delta x_e} \quad (2.27)$$

(see Figure 2.2).

With all terms in Equation (2.25) defined, the differential Equation (2. Equation (2.21)) becomes the algebraic equation

$$a_p u_p = a_E u_E + a_W u_W + a_U u_U + a_D u_D + \bar{B}_x \Delta z_p \Delta x_p - (P_e - P_w) \Delta z_p, \quad (2.28)$$

which can be written as

$$a_p u_p = \sum_1^m a_l u_l + S_{int}. \quad (2.29)$$

In Equation (2.29) S_{int} is as defined above and the subscript m denotes a “neighboring” volume (for a 2D coordinate system, $m=4$). The domain is discretized by $r \times c$ individual volumes, resulting in $r \times c$ equations like Equation (2.29). To allow for the implementation of boundary conditions, a row or column of “dummy” volumes are included in the east and west most columns of the coefficient arrays a_E and a_W and in the upper and lower most rows of the coefficient

arrays a_U and a_D . With boundary conditions included, Equation (2.29) gives $r \times c$ linear equations in $r \times c$ unknowns and can be rearranged to

$$\mathbf{A} \bar{u} = \bar{s}. \quad (2.30)$$

\mathbf{A} is a sparse matrix containing the coefficients in Equation (2.25) along the appropriate diagonals, \bar{s} is a vector of source terms and \bar{u} is the solution vector of horizontal velocity components. A similar set of equations is constructed to solve for the vertical velocity field. Any appropriate method may be used to solve Equation (2.30). Here, we use subroutines native to the *Matlab*© software package. Because the orthogonal-coordinate system allows for a straightforward discretization of the governing equations, \mathbf{A} is banded with non-zero elements along only five of the diagonals and can be inverted directly (\mathbf{A} is “pentadiagonal”). This presents an advantage over some FEM discretization schemes which lead to a “fuzzy” banded coefficient matrix and require iterative methods for inversion.

Unlike the momentum balance equations, the non-steady and advective terms in the heat balance equation cannot be neglected and require additional considerations. These are discussed in Appendix B. Briefly, a high-order, up-winding scheme, weighted by the Peclet number, partitions the interface flux into its advective and diffusive components. Forward time stepping of the heat balance equation is handled in a fully implicit manner.

The pressure-correction method

In general, the pressure in Equation (2.23) is not known *a priori*. The FVM solves for the pressure and velocity fields sequentially using an iterative “pressure-correction” method (Patankar, 1980). We discuss the method in detail in Appendix C. In summary, the horizontal and vertical velocity fields are solved for based on a guessed pressure field (through equations like Equation (2.30)). Using these

velocity field estimates, the continuity equation is integrated over each individual volume to find its associated mass source (or sink). This mass source, which must eventually be annihilated to satisfy continuity, is used to calculate a correction to the local pressure and velocity fields. The corrected velocity field satisfies continuity both locally (within each volume) and globally (over the entire domain). The corrected pressure field then serves as a new initial guess from which updated u and w fields, an updated mass source, and updated corrections are calculated. Iterations continue in this manner until the mass source in each volume is ~ 0 . At this point the associated pressure and velocity corrections are also 0 and the u , w , and P fields satisfy continuity. The calculation proceeds to the true velocity and pressure fields by way of a number of continuity satisfying fields.

General solution procedure

Our coupled, thermomechanical model is similar to that of Hvidberg (1996) in that it consists of 3 interacting submodels: (1) the heat-balance model, (2) the momentum-balance model, and (3) a surface-evolution model. At each time step, the domain geometry and the boundary and initial conditions allow for calculation of an associated velocity field. The velocity field serves as an input to the heat-balance model, through which an updated temperature field is calculated. The velocity field also determines the updated domain geometry through evolution of the free surface. The new temperature field and domain geometry are then used as inputs for calculating the velocity field at the proceeding time step.

The ice viscosity is a non-linear function of the velocity field (through Equations (2.6), (2.7), and (2.10)), making the momentum-balance equations non-linear. This non-linearity is treated iteratively: an initial guess for the viscosity is used to calculate an initial velocity field, from which updated effective-strain rate and effective viscosity fields are calculated. Iteration continues until both the velocity and viscosity fields converge. The iteration on the effective-viscosity occurs simultaneous to the pressure-correction iteration discussed above.

Examination of Equation (2.14) indicates that the free surface boundary condition on u requires that the value of w is known. Similarly, Equation (2.15) indicates that the boundary condition on w requires that P be known and Equation (2.16) indicates that the boundary condition on P requires that w be known. Because the values for u , w , and P are not solved for simultaneously, this problem is also treated through iteration. For example, Equation (2.14) simply uses the value of w predicted during the previous iteration. As the viscosity, pressure, and velocity fields converge over the course of iteration, the differences between current and previous estimates for u , w , and P vanish and the boundary conditions in Equations (2.14)-(2.16) become self-consistent.

The heat-balance source term in Equation (2.4) is calculated from the converged stress and strain rate fields at any time step. Here, we make the simplifying assumption that the dominant shear and strain rate components are σ_{zx} and $\dot{\epsilon}_{zx}$. While k and C in Equation (2.4) are functions of temperature, they vary in a minor and approximately linear manner over the range of temperatures expected in a polar ice sheet. We use standard relations (Table 2.2) to calculate their values based on the temperature field from the previous time step and, in doing so, account for the non-linearity in Equation (2.4). In the upper ~ 100 m of the ice column, we use simple analytical expressions to account for thermal properties in firn (Paterson, 1994, p.14).

During model “spin up” from initial conditions, 10^1 - 10^2 iterations of the momentum-balance model are necessary to obtain a converged velocity field. As the temperature, velocity, and effective viscosity fields converge (i.e. solutions at the present time step become similar to those from the previous time step), the required number of iterations generally decreases to $\leq 10^1$. Solutions to the momentum equations conserve volume locally and globally to within machine accuracy ($O \sim 10^{-12}$). Because the number of iterations required to obtain a converged velocity solution is always greater than that required to obtain a converged temperature solution (1 iteration), the heat-balance model is run at each time step.

The model domain consists of two layers, an ice layer sitting atop a bedrock layer. Within the ice layer, the heat and momentum equations are solved. Within the bedrock layer, the heat equation alone is solved for the case of no advection. The bedrock layer is specified so that its minimum thickness equals the maximum ice thickness at the start of a model run. Its geometry and thermal properties are held constant over time. The calculated velocity field and the specified accumulation rate determine changes in the shape of the ice-layer domain through evolution of the free surface. When describing ice flow over a frozen ice-bed interface with horizontal velocities of $\sim 1-10 \text{ m a}^{-1}$, we update the surface at 20-year time steps. Small interpolation errors during regridding preclude absolute volume conservation: for steady-state boundary conditions (surface temperature, accumulation rate, and geothermal flux), a $\sim 1 \times 40 \text{ km}$ domain allowed to evolve over 10^5 a experiences a fractional volume change of $\sim 10^{-5}$ ($\sim 10^{-3} \%$). The equivalent (erroneous) rate of ice thickness change is $\sim 10^{-7} \text{ m a}^{-1}$. These errors could be further reduced by adjusting the grid spacing and/or by iterating on the momentum equations until the mass source within each volume becomes smaller than some arbitrarily chosen number.

ORTHOGONAL, CURVILINEAR COORDINATE SYSTEM

So far, our discussion of the FVM has been in the context of a rectangular domain in 2-D, Cartesian coordinates. This discussion is easily extended to 2D, curvilinear domains provided that those domains are described by an orthogonal coordinate system. Once a suitable coordinate system has been constructed, the formulation described above is altered by multiplying terms involving length, area, and volume by the appropriate combination of scale factors (analogous to the scale factors relating polar and Cartesian coordinates). We now focus on the task of constructing such a coordinate system for 2D domains with arbitrarily shaped upper and lower boundaries (here, profiles of the surface and basal topography). Below, we give a

general discussion of the coordinate system and its construction. Additional details are discussed in Appendix A.

Initial coordinate system

The coordinate system, constructed using the method of orthogonal trajectories (Eiseman, 1982), requires an initial coordinate system of the form

$$\mathbf{r}(x, z) = \mathbf{r}(x, z(x, \hat{z})). \quad (2.31)$$

The position vector in a Cartesian reference frame, \mathbf{r} , has components x and z , which we have been non-dimensionalized with some relevant length scale, L . A “stretched” vertical coordinate, \hat{z} , is given by

$$\hat{z} = \frac{z - b(x)}{s(x) - b(x)}, \quad (2.32)$$

where $s(x)$ and $b(x)$ describe the scaled surface and bed elevation profiles, respectively (A list of variables used in calculation of the coordinate system is given in Table 2.3). The \hat{z} coordinate ranges from 0 along $b(x)$ to 1 along $s(x)$. Rearranging Equation (2.32) for z gives

$$z(x, \hat{z}) = \hat{z} \cdot [s(x) - b(x)] + b(x). \quad (2.33)$$

By holding \hat{z} constant and varying x in Equation (2.33), a curve is traced in (x, z) space. For j values of \hat{z} from 0 to 1, Equation (2.33) traces out j such curves, each one connecting points with equal fraction of the domain thickness (Figure 2.3). This forms one set of coordinate curves, the $\hat{x}(x, z)$ coordinate curves, in the new, curvilinear coordinate system. The set of coordinate curves perpendicular to these,

the \hat{z} coordinate curves, completes the new coordinate system (Figure 2.4). We now discuss a method for defining this second set of coordinate curves.

The fundamental equation for orthogonal trajectories

The set of \hat{z} coordinate curves, or lines of constant \hat{x} , is found using the method of orthogonal trajectories (Eiseman, 1982). The method employs the surface metric,

$$\bar{g}_{lk} = g_{ij} \frac{\partial x_i}{\partial y_l} \frac{\partial x_j}{\partial y_k}, \quad (2.34)$$

which is the rule for changing from one set of planar surface coordinates, (x_1, x_2) , to another, (y_1, y_2) . The metric attached to the (y_1, y_2) (orthogonal, or *final*) coordinates) is given by \bar{g}_{lk} and the metric attached to the (x_1, x_2) (non-orthogonal, or *initial*) coordinates is given by g_{ij} . The surface metric expresses the relationship between tangent vectors to coordinate curves according to

$$g_{ij} = \mathbf{e}_i \cdot \mathbf{e}_j, \quad (2.35)$$

where \mathbf{e}_i is the tangent vector in coordinate direction x_i given by

$$\mathbf{e}_i = \frac{\partial \mathbf{r}}{\partial x_i} \quad (2.36)$$

(note that \mathbf{e}_i is *not* necessarily a unit vector). Any orthogonal, planar coordinate system must meet the requirement that

$$g_{12} = \mathbf{e}_1 \cdot \mathbf{e}_2 = 0. \quad (2.37)$$

Expanding Equation (2.34) with $(x_1, x_2) = (x, \hat{z})$ associated with g_{ij} (the non-orthogonal, *initial* coordinates) and $(y_1, y_2) = (\hat{x}, \hat{z})$ associated with \bar{g}_{ik} (the orthogonal, *final* coordinates) gives

$$\frac{\partial x}{\partial \hat{z}} = \frac{-g_{12}}{g_{11}}. \quad (2.38)$$

Eiseman (1982) refers to Equation (2.38) as the “fundamental equation for orthogonal trajectories”. In Appendix A we show that the RHS of Equation (2.38) is given by

$$-\frac{g_{12}}{g_{11}} = -\frac{\mathbf{e}_1 \cdot \mathbf{e}_2}{\mathbf{e}_1 \cdot \mathbf{e}_1} = \frac{(\hat{z} \cdot (s' - b') + b')(s' - b')}{1 + (\hat{z} \cdot (s' - b') + b')^2}, \quad (2.39)$$

in which primes denote derivatives w.r.t. x . For any value of \hat{z} between 0 and 1, Equation (2.39) is solely a function of the surface and bed profiles in the initial, non-orthogonal coordinate system.

To obtain the set of coordinate curves perpendicular to the \hat{x} coordinate curves, Equation (2.38) is integrated between curves of constant \hat{z} . As an example, consider the initial point $(x_{(0,0)}, z_{(0,0)})$, where the subscripts refer to coordinates along the \hat{x} and \hat{z} coordinate curves, respectively (Figure 2.5). Our initial point is the intersection of the lowermost domain boundary, $b(x)$, along which $\hat{z}=0$, and the leftmost domain boundary, along which $\hat{x}=0$. Our goal is to find the coordinates in (x, z) space where the \hat{z} coordinate curve originating at $(x_{(0,0)}, z_{(0,0)})$ intersects with the next \hat{x} coordinate curve, the point given by $(x_{(0,\Delta\hat{z})}, z_{(0,\Delta\hat{z})})$. Integrating Equation (2.38) from $\hat{z}=0$ to $\hat{z}=\Delta\hat{z}$ gives

$$x_{(0,\Delta\hat{z})} = x_{(0,0)} + \int_0^{\Delta\hat{z}} \frac{\partial x}{\partial \hat{z}} d\hat{z}, \quad (2.40)$$

which is the desired x coordinate. The corresponding z coordinate, $z_{(0,\Delta\hat{z})}$, is obtained by solving Equation (2.33) with $x=x_{(0,\Delta\hat{z})}$ and $\hat{z}=\Delta\hat{z}$. To define the next segment of the \hat{z} coordinate curve one continues on, this time starting at $x_{(0,\Delta\hat{z})}$ and integrating from $\hat{z}=\Delta\hat{z}$ to $\hat{z}=2\Delta\hat{z}$ (for the moment, we assume constant grid spacing in the \hat{x} and \hat{z} directions). The entire coordinate curve is constructed when the last segment, that spanning $\hat{z}=1-\Delta\hat{z}$ and $\hat{z}=1$, has been constructed. To build the entire grid, we continue by integrating along the \hat{z} coordinate curve starting at $(x_{(\Delta\hat{x},0)}, z_{(\Delta\hat{x},0)})$, then along the curve starting at $(x_{(2\Delta\hat{x},0)}, z_{(2\Delta\hat{x},0)})$, and so on. The grid is complete when the final curve, that originating at $(x_{(1,0)}, z_{(1,0)})$, has been constructed. When complete, each grid point (coordinate curve intersection) in (\hat{x}, \hat{z}) space is described by a corresponding grid point in (x, z) space. In practice, the initial coordinate, the integrand, and the integration limits in Equation (2.40) are row vectors and the entire suite of \hat{z} coordinate curves is integrated simultaneously. Because the grid is discrete, rather than continuous, additional considerations are necessary to ensure orthogonality at grid point intersections. This and other details of the integration procedure are discussed further in Appendix A.

Scale factors

Figures 2.4 and 2.6 show an orthogonal, curvilinear grid in the (x, z) domain and its counterpart in the (\hat{x}, \hat{z}) domain. Lengths, areas, and volumes in the two coordinate systems are related through a set of scale factors. For an arbitrarily shaped domain, there are no analytical expressions for the scale factors. Instead, they are calculated from the curvilinear grid geometry in the (x, z) domain and the grid spacing in the (\hat{x}, \hat{z}) domain.

The unit vector and scale factor along the \hat{x} coordinate direction are related according to

$$\hat{\mathbf{e}}_{\hat{x}} = \frac{\partial \mathbf{r}}{\partial \hat{x}} \left\| \frac{\partial \mathbf{r}}{\partial \hat{x}} \right\|^{-1} = \frac{\partial \mathbf{r}}{\partial \hat{x}} \frac{1}{h_{\hat{x}}}, \quad (2.41)$$

where \mathbf{r} is the position vector in the (x, z) domain and $\|\mathbf{x}\|$ denotes the magnitude of the vector \mathbf{x} . Equation (2.41) expresses the unit vector $\hat{\mathbf{e}}_{\hat{x}}$ in terms of its components in the (x, z) coordinate system. The scale factor, $h_{\hat{x}}$, relates length in the (x, z) domain to length along the \hat{x} coordinate direction. In discrete form, it is given by

$$h_{\hat{x}} = \left\| \frac{\partial \mathbf{r}}{\partial \hat{x}} \right\| \approx \left[\left(\frac{\Delta x}{\Delta \hat{x}} \right)^2 + \left(\frac{\Delta z}{\Delta \hat{x}} \right)^2 \right]^{\frac{1}{2}} \quad (2.42)$$

(Figure 2.7). The values for $\Delta \hat{x}$ and $\Delta \hat{z}$ are given by the grid spacing in the (\hat{x}, \hat{z}) domain, which is specified prior to integration of Equation (2.38). A similar expression gives the scale factor along the \hat{z} coordinate direction.

The scale factors relate lengths, areas, and volumes in the (x, z) , or real domain, to those in the (\hat{x}, \hat{z}) , or calculation domain. For example, the RHS of Equation (2.21), expressed in the calculation domain and with $i = \hat{x}$, becomes

$$\frac{1}{h_{\hat{x}}} \frac{\partial}{\partial \hat{x}} \left(\Gamma \frac{1}{h_{\hat{x}}} \frac{\partial \phi}{\partial \hat{x}} \right) + S, \quad (2.43)$$

where the $\partial \hat{x}$ now refers to a partial derivative w.r.t. the (\hat{x}, \hat{z}) coordinate system. In practice, scale factors are simply included as additional factors when defining the coefficients in Equation (2.25). In the calculation domain, the coefficient a_E from Equation (2.25) becomes

$$a_E = \frac{h_{\hat{z}}}{h_{\hat{x}}} \frac{\eta_e \Delta \hat{z}}{\delta \hat{x}_e}, \quad (2.44)$$

where $\Delta\hat{z}$ and $\delta\hat{x}_e$ are the analogues of Δz and δx_e from Figure 2.1 but in the (\hat{x}, \hat{z}) coordinate system.

MODEL VALIDATION

Comparison to analytical solutions

For simple domain shapes and boundary conditions, steady-state, analytical solutions are available for validating model output. Results from the heat-balance model are compared to the 1-D, analytical solution for steady-state flow at an ice divide, which assumes (1) a linearly decreasing vertical-velocity field, (2) no horizontal advection, and (3) temperature independent thermal properties (Hooke, 1998, p. 72, Equation (2.6.24)). We specify these conditions and a constant accumulation rate and geothermal flux on a 1000 m thick rectangular slab discretized by a 100 finite volumes in the vertical. A steady-state temperature solution is approximated by forward-time stepping 10^6 a at 10^3 a time steps. For this simple test case involving advection, the model and analytical solution agree to within $<10^{-3}$ K. As an approximate test of the 2D solution, we compare model and analytical solutions for steady-state heat conduction within an annulus of constant conductivity. Temperature is prescribed on the outer radius and heat flux is prescribed on the inner radius. In this case, there should be no heat flux in the radial direction. Our 2D model temperature field agrees with the analytical temperature field to within $\sim 10^{-12}$ K. This is not a rigorous test of the 2D temperature solution since we have still only approximated a 1D temperature field. It does, however, confirm that there is no spurious conductive heat flux within the model when we consider a 2D, curvilinear domain.

Solutions from the momentum-balance model are compared to steady-state, analytical solutions to the Navier-Stokes equations including: (1) Poiseuille, or

“pipe”, flow (here, flow between two parallel, rigid plates), (2) flow in a parallel-sided slab on an inclined plane with Newtonian viscosity and (3), similar to (2) but with a power-law viscosity. Because an infinite length in the along- and across-flow directions is assumed in all cases, w should be 0 everywhere and u should vary only as a function of the vertical coordinate. Case (1) involves specifying the analytical solution for u on the domain sides and no slip ($u=w=0$) at the top and bottom boundaries. Cases (2) and (3) involve specifying a stress-free upper boundary, no slip on the bottom boundary, and the analytical solution for u at the domain sides. The solutions are calculated on a 20×30 grid for a scaled domain with a 1:100 aspect ratio. Figure 2.8 shows maps of the calculated, normalized u fields. Overlain on each map is the analytical shape function for the solution (solid line) and a model solution from near the center of the model domain (dots). In all cases, w is everywhere fractionally $\sim 10^{-14}$ - 10^{-8} relative to u . Because a finite number of piecewise-linear segments must approximate the continuous, analytical solution presented at the domain boundary, minor differences between the analytical and numerical solutions do occur. As the number of finite volumes used for discretization increases (i.e. as the grid resolution increases), these differences approach zero.

Comparison to previous work

A more taxing test of the momentum-balance model is given by examining the modeled velocity fields at, and near to, a flow divide. Here, we present results for three cases, (1) isothermal flow in plane strain, (2) isothermal flow along a linearly widening flowband (Appendix D discusses several minor alterations to the model for the case of a flowband of non-unit width), and (3), thermomechanically coupled flow in plane strain. In all cases, the velocity fields are approximately steady-state: surface temperature and accumulation were held constant and the surface shape was allowed to evolve until the rate of thickness change was $\leq 10^{-6}$ m a⁻¹.

Figure 2.9 shows horizontal and vertical velocity shape functions from the model for the three cases noted above. For all cases, the shape functions show the same general patterns. At and near to the divide, the horizontal velocity shape functions are more linear and the vertical velocity shape functions are more parabolic in shape, relative to profiles off of the divide. The reasons for this have been discussed in detail by previous authors (e.g. Raymond, 1983). For isothermal plane strain, the model indicates that the zone of “divide-flow” (the region over which vertical velocity shape functions differ from those on the flank) is $\sim 1\times$ the ice thickness in width (Figure 2.9a). This is in good agreement with the work of previous authors (Raymond, 1983; Hvidberg, 1996). For an isothermal flowband that widens linearly by a factor of 15 at a distance of 20 ice thicknesses, the width of the divide-flow zone increases to $\sim 4\times$ the ice thickness (Figure 2.9b). This result agrees well with isothermal, axisymmetric flow modeling done by Hvidberg (1996). Finally, in Figure 2.9c we show velocity shape functions for thermomechanically-coupled flow in plane strain. This result is also in good agreement with the previous work of Hvidberg (1996).

CONCLUSIONS

We have presented a new, two-dimensional, full-stress numerical ice-flow model for two-dimensional domains with variable width. The model is similar to that of Hvidberg (1996) in that it consists of three interacting submodels; a heat-balance model, a momentum-balance model, and a surface-evolution model. Governing equations are solved with the FVM, which is intermediate to the more commonly used FEM and FDM methods; it solves the integral form of the governing equations but on a structured grid with non-uniform spacing. An important advantage to the method is that no terms in the governing equations need be omitted (for example, longitudinal-stress gradients and “bridging effects” (Van der

Veen and Whillans, 1989)). Temperature and velocity fields from the model compare well with analytical solutions and with the work from previous authors.

A unique aspect of the model is the use of a curvilinear, orthogonal coordinate system for the description of arbitrarily shaped domains. The coordinate system provides some clear advantages over structured and unstructured grids that are non-orthogonal. First, coordinate directions are everywhere parallel and perpendicular to domain boundaries, which simplifies the implementation of boundary conditions. Second, because of the orthogonal nature of the grid, discretization of the governing equations leads to banded sparse matrices that may be inverted directly, rather than through iterative methods. The method for constructing the coordinate system is relatively straightforward and could be adapted for use with other solution methods that require a structured grid.

The method described here does have limitations. While the FVM method is easily extended to three-dimensions, there are very few 3D, orthogonal, curvilinear coordinates systems. Furthermore, there is no straightforward way to construct a 3D, orthogonal, curvilinear coordinate system for an arbitrarily shaped domain. While some time savings is afforded by our coefficient matrices, which can be inverted directly, the iterative nature of the pressure-correction method requires that numerous smaller matrices be inverted in sequence, rather than inverting for the velocity and pressure fields simultaneously in one big matrix. Finally, using the model in a predictive sense requires that the domain be regrided at every time step. Depending on the size of the time step used, regriding can make up a substantial portion of the total model run time.

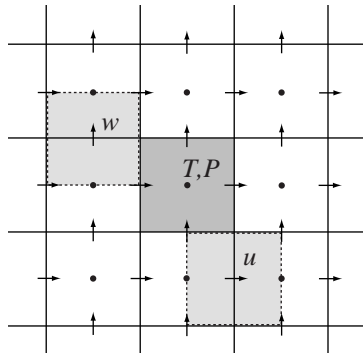


Figure 2.1: Staggered grid used in heat and momentum and balance models. u (w) calculation volumes are offset $1/2$ grid space in the horizontal (vertical) direction from T and P calculation volumes. Velocity volume centers are T and P interface centers, and vice versa.

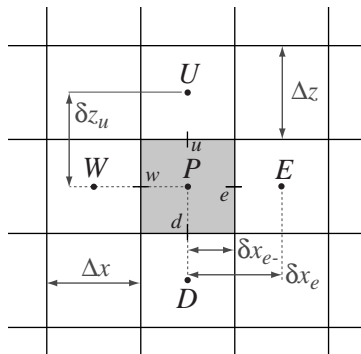


Figure 2.2: Finite volume centered at P and neighboring volumes. Neighboring volumes are centered at points to the east, west, up, and down (E , W , U , and D , respectively) and have interfaces at points e , w , u , and d . Other variables are discussed in text.

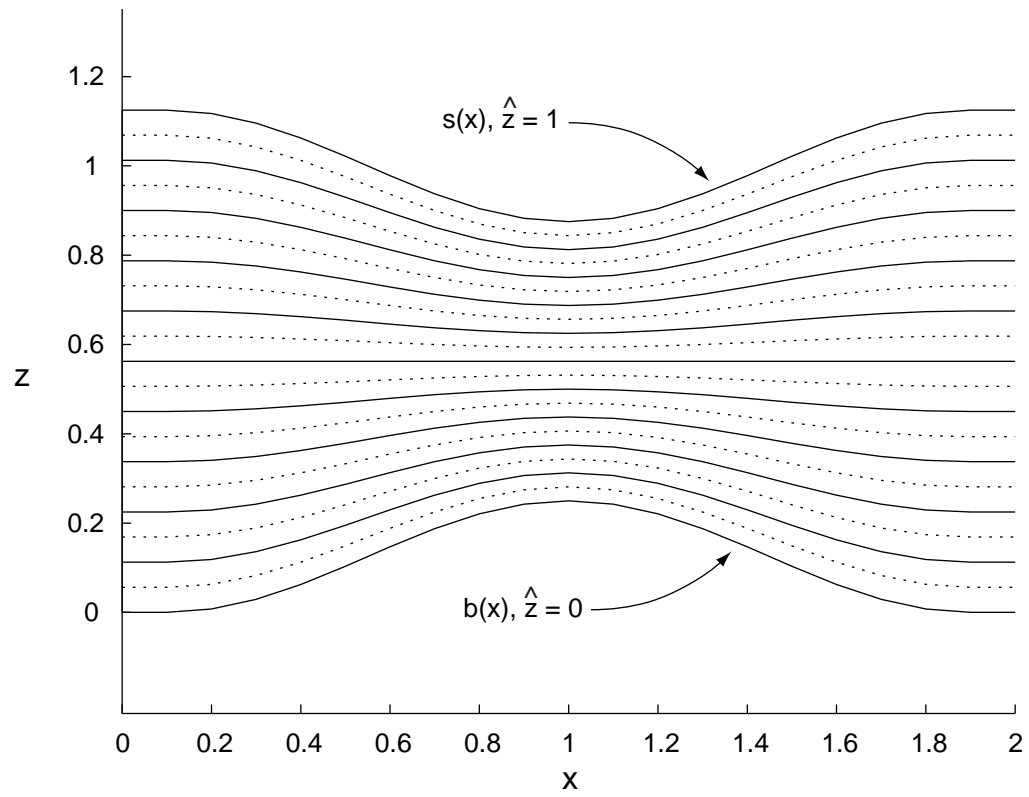


Figure 2.3: Curves of constant \hat{z} in (x, z) space. Ultimately, these make up the set of \hat{x} coordinate curves.

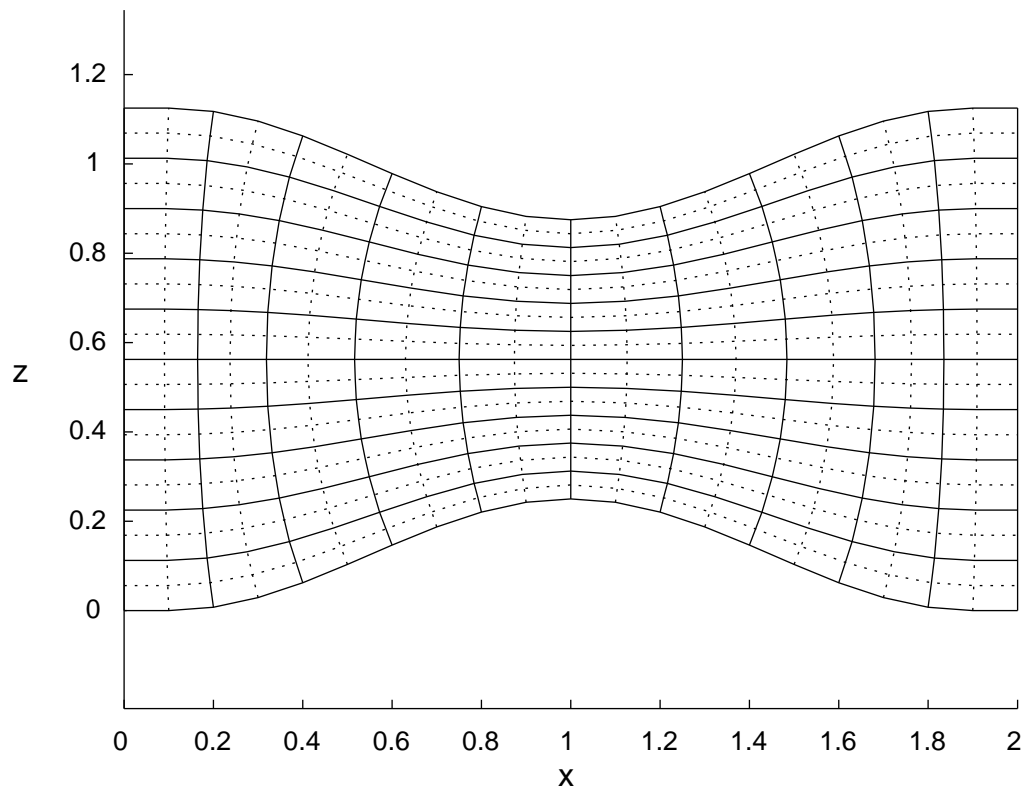


Figure 2.4: Final grid of (\hat{x}, \hat{z}) coordinate curves in (x, z) space. Solid lines denote volume boundaries. Volume and interface centers points lie along dashed lines.

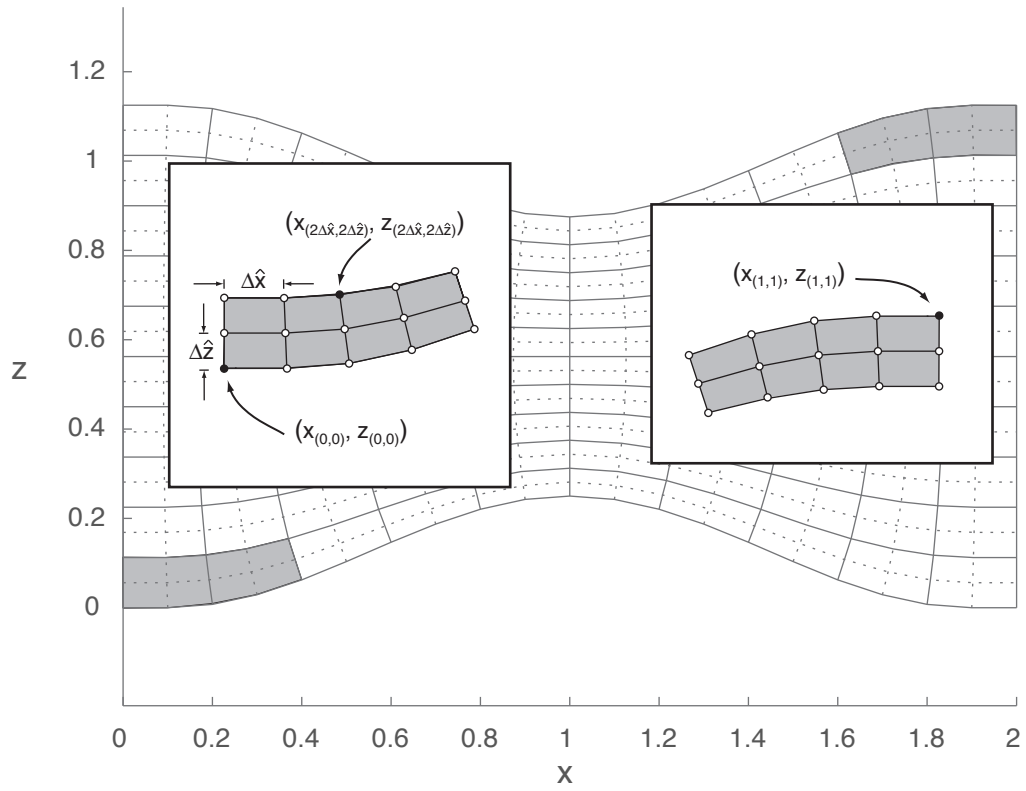


Figure 2.5: Variables involved in the calculation of the coordinate system.

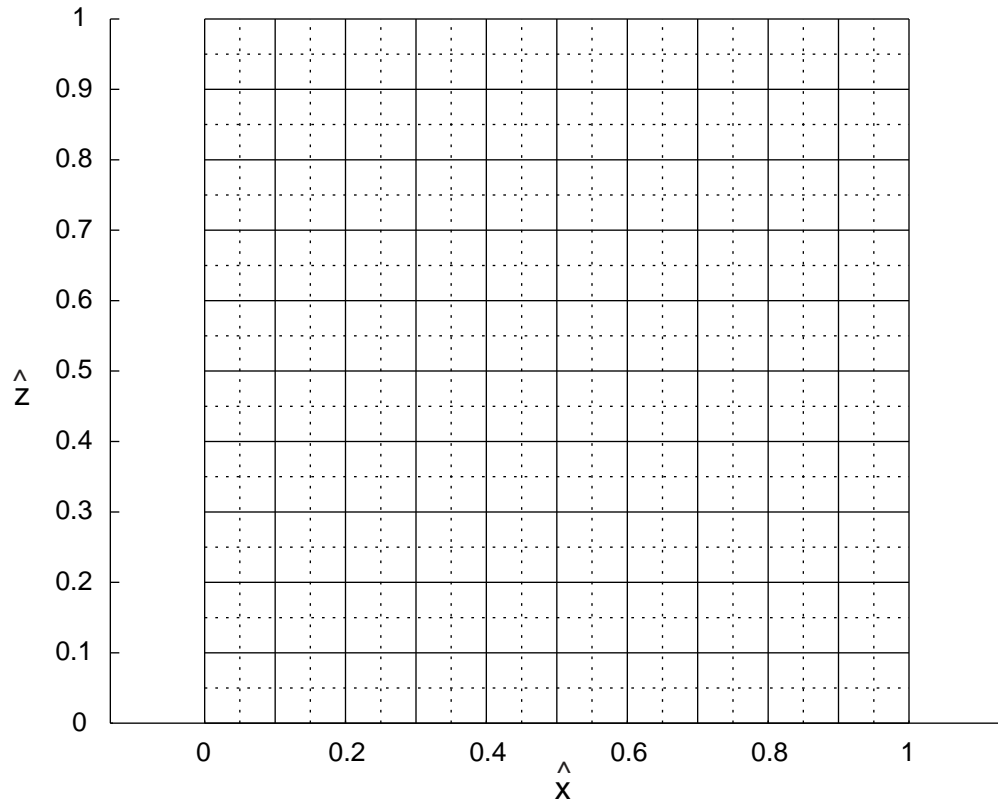


Figure 2.6: Final grid of (\hat{x}, \hat{z}) coordinate curves in (\hat{x}, \hat{z}) space. Solid lines denote volume boundaries. Volume and interface center points lie along dashed lines.

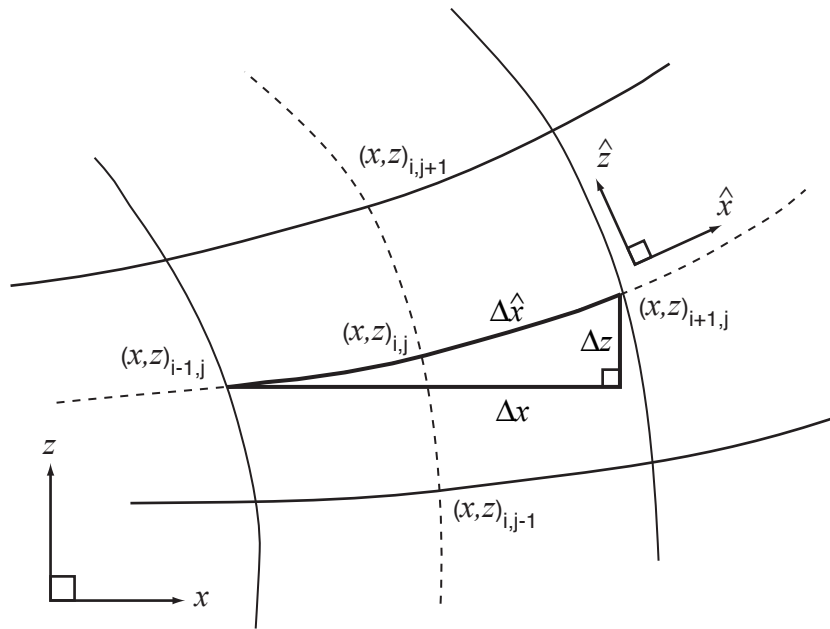


Figure 2.7: Definition of variables needed for calculation of the scale factor $h_{\hat{x}}$.

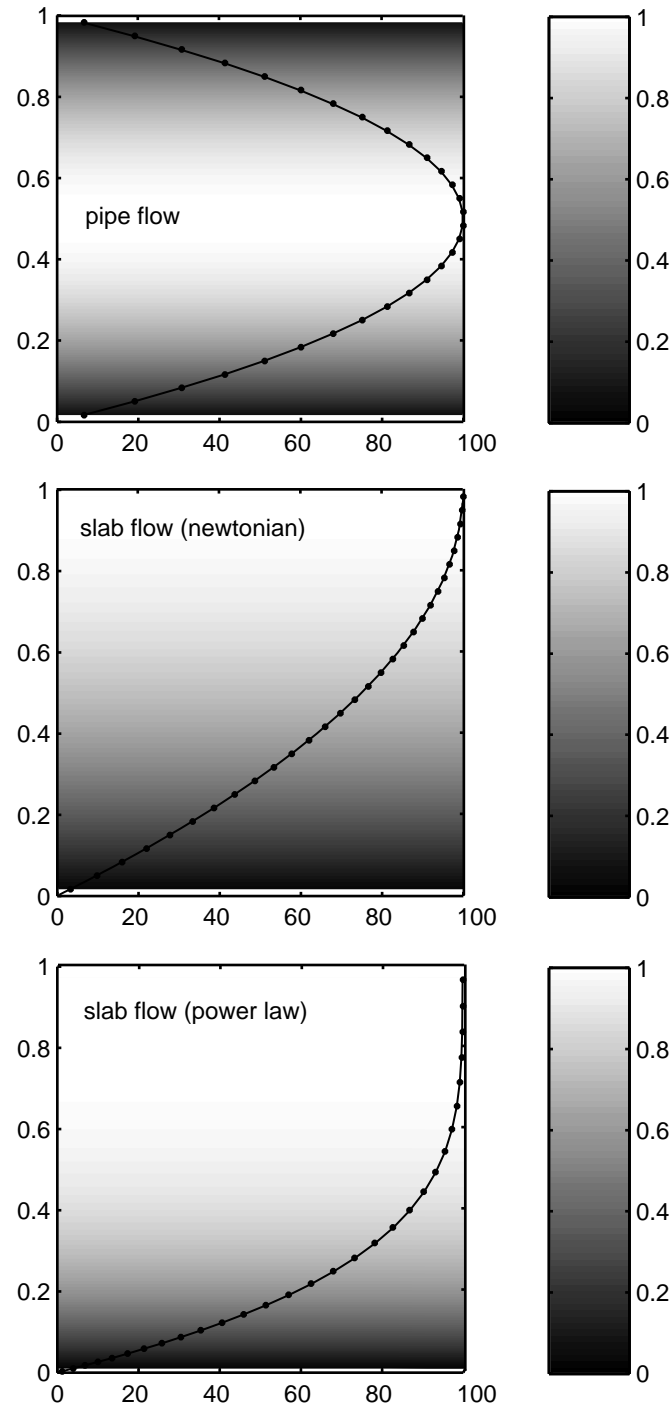


Figure 2.8: Comparison of analytically and numerically calculated velocity fields. Non-dimensional, 2-dimensional u fields (greyscale) for (a) Poiseuille flow, (b) isothermal, Newtonian viscous slab flow, and (c) isothermal, power-law viscous slab flow. Solid lines are normalized vertical profiles (i.e. shape functions) based on analytical solutions. Dots are normalized velocity profiles from the model, taken from profiles near $x=50$.

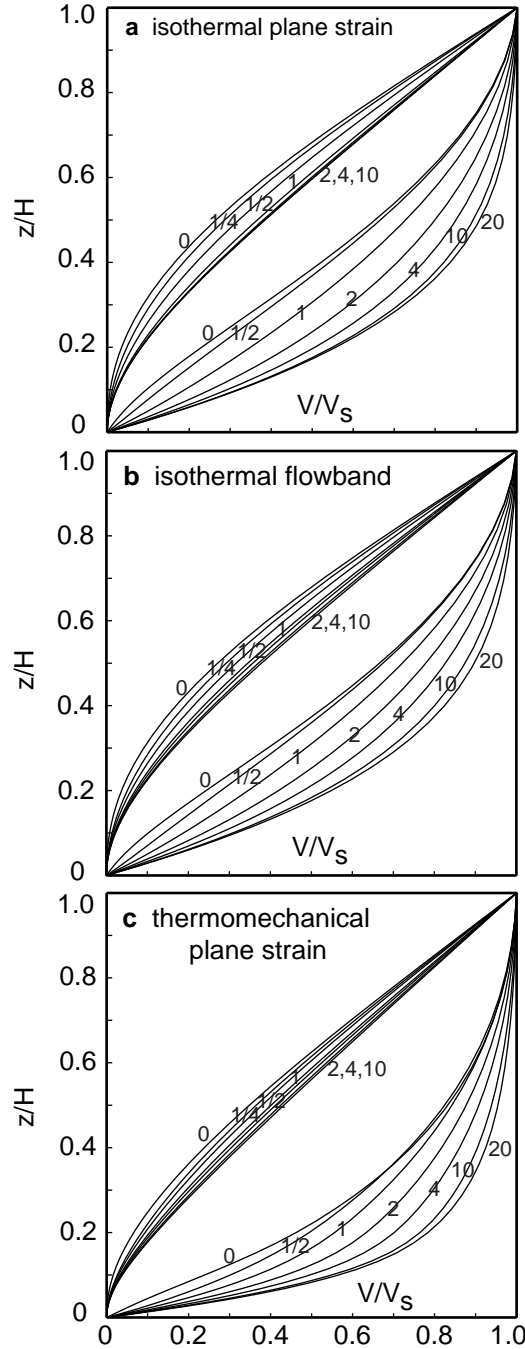


Figure 2.9: Modeled velocity shape functions at a flow divide. Horizontal (u) and vertical (w) velocity fields normalized by the surface velocity and plotted as a function of normalized vertical coordinate for (a) isothermal plane strain, (b) an isothermal flowband widening linearly downstream, and (c) thermomechanical plane strain. Different lines denote distance from the flow divide in units of ice thickness (0, 1/2, 1, 2, 4, 10, and 20 ice thicknesses for u , 0, 1/4, 1/2, 1, 2, 4, and 10 ice thicknesses for w).

Table 2.1. Variables used in heat and momentum balance models.

Symbol	Variable	Units
A	Temperature-dependent rate factor	$\text{Pa a}^{1/3}$
\mathbf{A}	pentadiagonal, banded, sparse-coefficient matrix	—
a_K	generic FVM coefficient at volume center K ($K=P,E,W,U,D$)	a
α	weight factor for calculating interface diffusivities	—
B	Inverse rate factor	$\text{Pa a}^{1/3}$
\bar{B}_i	volume-mean body force	N m^{-3}
b	generic, non-steady, advective-diffusion equation source term	$\phi \text{ m}^{-3} \text{ a}^{-1}$
\dot{b}	Ice-equivalent accumulation rate at surface	m a^{-1}
β	interpolation weight across time step Δt	—
D_k	diffusive mass-flow rate at interface k ($k=e,w,u,d$)	$\text{kg m}^{-1} \text{ a}^{-1}$
d_p^u, d_p^w	pressure and velocity correction proportionality constant	$\text{m a}^{-1} \text{ Pa}^{-1}$
$\Delta x_K, \Delta z_K$	dimensions of individual volume at K ($K=P,E,W,U,D$)	m
δ_{ij}	Krönecker delta or identity matrix	—
$\delta x_k, \delta z_k$	distance between volume centers across face k ($k=e,w,u,d$)	m
$\dot{\epsilon}_{ij}$	strain-rate tensor	a^{-1}
$\dot{\epsilon}_e$	effective strain-rate	a^{-1}
F_k	advective mass-flow rate at interface k ($k=e,w,u,d$)	$\text{kg m}^{-1} \text{ a}^{-1}$
Γ	diffusivity for generic FVM equation	—
H	ice thickness	m
J_i	combined advective and diffusive flux in direction i	flux
λ	pressure-correction relaxation factor	—
n_i	Cartesian surface-normal vector	—
η	effective viscosity	Pa a
η_k	effective viscosity at volume interace k ($k=e,w,u,d$)	Pa a
P	pressure	Pa
P_{atm}	atmospheric pressure	Pa
P_{sfc}	surface pressure	Pa
P_k^*	guessed pressure at interface k ($k=e,w,u,d$)	Pa
P_k'	pressure correction at interface k ($k=e,w,u,d$)	Pa
Pe_k	Peclet number at interface k ($k=e,w,u,d$)	—
ϕ	scaler solution to generic FVM equation	—
S	source term for generic FVM equation	—
S_{Int}	volume-integrated source term for generic FVM equation	—
σ_{ij}	full stress tensor	Pa
T_i	traction vector	Pa
t	time	a
τ_{ij}	deviatoric stress tensor	Pa

Table 2.1: continued

θ	temperature	K
θ_s	surface temperature	K
\bar{u}_k	column-averaged velocity at finite volume face k ($k=e,w,u,d$)	m a^{-1}
u,v	horizontal and vertical components of velocity	m a^{-1}
u_K, w_K	velocity at velocity-volume centerpoint, K ($K=P,E,W,U,D$)	m a^{-1}
u_k^*, w_k^*	guessed velocity at interface k ($k=e,w,u,d$)	m a^{-1}
u_k', w_k'	velocity correction at interface k ($k=e,w,u,d$)	m a^{-1}
\hat{u}_k, \hat{w}_k	pseudo velocity at interface k ($k=e,w,u,d$)	m a^{-1}
W	flowband width	m
x,z	horizontal and vertical coordinates (Cartesian)	m
\hat{x}, \hat{z}	horizontal and vertical coordinates (orthogonal, curvilinear)	—

^aHeat and momentum balance equations have different coefficient definitions.

Table 2.2. Constants and other model parameters.

Symbol	Constant	Value	Units
A_0	flow-law constant ($\theta > 263$ K)	6.26 ^a	$10^{10} \text{ Pa}^{-3} \text{ a}^{-1}$
A_0	flow-law constant ($\theta \leq 263$ K)	1.3 ^a	$10^5 \text{ Pa}^{-3} \text{ a}^{-1}$
C	specific heat	b	J kg^{-1}
g	gravitational acceleration	9.81	m s^{-2}
k	conductivity	c	$\text{W K}^{-1} \text{ m}^{-1}$
L	characteristic length scale	1015	m
n	power-law exponent	3	—
Q	activation energy ($\theta > 263$ K)	139 ^d	10^3 J mol^{-1}
Q	activation energy ($\theta \leq 263$ K)	60 ^d	10^3 J mol^{-1}
Q_{geo}	geothermal flux	70 ^e	10^{-3} W m^{-2}
R	universal gas constant	8.314	$\text{J mol}^{-1} \text{ K}^{-1}$
ρ	density of ice	918	kg m^{-3}

^a (Paterson, 1994, p.86,97)

^b $C(\theta) = 152.5 + 7.12 \cdot \theta$ (*ibid*, p.205)

^c $k(\theta) = 9.828 \cdot \exp(-0.0057 \cdot \theta)$ (*ibid*)

^d (*ibid*, p.86)

^e (Engelhardt, 2004; Gary Clow, personal comm.. 2005)

Table 2.3. Variables used when creating orthogonal, curvilinear-coordinate system.

Symbol	Variable	Units
\mathbf{r}	position vector Cartesian reference frame	m
\mathbf{e}_i	tangent vector to coordinate curve x_i	—
$\hat{\mathbf{e}}_{\hat{i}}$	unit vector along orthogonal coordinate direction \hat{i}	—
s	surface elevation profile in Cartesian reference frame	m
b	bed elevation profile in Cartesian reference frame	m
\hat{z}	stretched vertical coordinate in Cartesian reference frame and vertical coordinate in curvilinear, orthogonal reference frame)	—
\hat{x}	horizontal coordinate in curvilinear, orthogonal reference frame	—
$\Delta x, \Delta z$	horizontal and vertical distance between gridpoints in the non-orthogonal reference frame.	m
$\Delta \hat{x}, \Delta \hat{z}$	horizontal and vertical distance between gridpoints in the orthogonal reference frame.	—
g_{ij}	surface metric for non-orthogonal reference frame	—
\bar{g}_{ij}	surface metric for orthogonal reference frame	—
$h_{\hat{i}}$	scale factor relating length in non-orthogonal reference frame to length along orthogonal coordinate direction \hat{i}	—

**A FULL-STRESS, THERMOMECHANICAL FLOWBAND MODEL
USING THE FINITE VOLUME METHOD PART II:
APPLICATION TO THE FLOW AND THICKNESS
HISTORY OF SIPLE DOME, WEST ANTARCTICA**

Portions of the material in this chapter were originally presented orally at the 11th annual WAIS workshop held in Sterling, VA, on September 29 through October 2nd, 2004. This chapter is a draft of the second half of the two-part manuscript started in Chapter 1 with University of Washington co-authors H. Conway and E.D. Waddington.

SUMMARY

We use a two-dimensional, full-stress, thermo-mechanical flowband model to investigate Holocene histories of ice thickness and ice flow at Siple Dome in West Antarctica. Measurements obtained from an ice core and borehole near the ice divide as well as measurements of radar-detected internal stratigraphy are used as targets for modeling. Models that only account for the climate history (accumulation rate and temperature) and assume a constant ice thickness yield a poor match to observations. Histories of ice dynamics (ice thickness, ice-divide location, ice-flow enhancement) also need to be included to obtain a reasonable match to observations. Our favored model specifies 350m of thinning at Siple Dome between 15,000 and 14,000 years ago, onset of divide flow 3,000 years ago, and non-trivial ice-flow enhancement for the past 30, 000 years. The timing of thinning is coincident with a 20 m rise in global sea level about 14,500 years ago. We speculate that increased activity of the surrounding ice streams associated with the pulse of sea-level rise initiated rapid drawdown of Siple Dome.

INTRODUCTION

The thickness and extent of the West Antarctic Ice Sheet (WAIS) has decreased considerably since the Last Glacial Maximum (LGM) (Bindschadler, 1998; Conway and others, 1999). Near the ice sheet margins, terrestrial and marine geologic studies have been used to constrain the ice-thickness history (Denton and others, 1991; Ackert and others, 1999; Anderson and others, 2002; Stone and others, 2003). However the thickness history of the interior of the ice sheet has no such constraints. Improved understanding of past configuration of the interior of the ice sheet is needed to: (1) assess the WAIS contribution to Holocene sea-level change; (2) assess whether the ice sheet has come into equilibrium with modern climate or if further changes are expected; (3) help determine the activity of ice streams during the LGM; (4) provide initial conditions and constraints for large-scale, predictive ice-sheet models.

Reconstructions of the Ross Sea Embayment based on evidence from moraines alongside East Antarctic outlet glaciers suggest that ice was 700 m thicker at Siple Dome during the LGM (Denton and others, 1991; Denton and Hughes, 2002). Analysis of the total-gas content from the Byrd ice core (NBY; Figure 3.1) was used to infer that ice there was both 200 m thinner (Raynaud and Lebel, 1979; Raynaud and Whillans, 1982) *and* 400-500 m thicker (Jenssen, 1983) at the LGM and during the early Holocene. Analysis of stable isotopes from the same core suggested that ice at Byrd was 500 m thicker at the LGM (Grootes and Stuiver, 1986).

Recent work suggests more modest thickening of the WAIS interior during the LGM. Moraine limits on Mt. Waesche (MW, Figure 3.1), a deglaciated volcano about 300 km northwest of Byrd, are dated at 10k yrs BP (10,000 yrs before present) and suggest the ice was only ~45 m thicker (Ackert and others, 1999). Steig and others (2001) adjusted the stable isotope record from the Byrd core to account for the advection of isotopically light ice from upstream; they suggest that ice at Byrd was about 200 m thicker than present during the early Holocene.

About 800 km downstream from Byrd, analysis of the internal stratigraphy of Roosevelt Island indicates that Roosevelt Island (RI, Figure 3.1) was ~300 m thicker than present 3 ka ago (Conway and others, 1999, Martin et al., 2006). Stone and others (2003), who used ^{10}Be exposure-age dating to determine when buried mountain flanks near the Ford Ranges (FR, Figure 3.1) were first exposed to cosmic rays, found that ice 80 km inland was ~200 m thicker than at present during the LGM.

Here we use geophysical data from Siple Dome (SDM, Figure 3.1) to further constrain the magnitude and timing of Holocene ice-thickness changes in the Ross Sea Embayment. Siple Dome, a 1000-m thick inter-ice-stream ridge, was the site of a deep ice coring effort during the 1990's. A primary goal of this project was to assess the history of ice dynamics of the region (U.S. Ice Core Working Group, 1992). We use data from the ice core, together with ancillary geophysical data from the region, to constrain the output of a two-dimensional, full-stress, thermomechanical ice-flow model.

We review results from previous work at SDM and briefly discuss our modeling approach. More details of the model are given in a companion paper (Price and others, Chapter 2). We then use the model to find a set of boundary conditions that give a reasonable fit to the observations and we explore the sensitivity of our results to perturbations from this best-fit scenario. Finally, we discuss our results in context of other studies.

PREVIOUS WORK

A 1000-m long ice core recovered from a site ~1/2 km south of the present-day flow divide at SDM has been dated by counting annual layers to a depth of 515 m (Taylor and others, 2005), and by correlating measurements of occluded CH_4 with measurements from the well-dated GISPII ice core from Greenland (Brook and others, 2005). Subsequent to coring, depth-profiles of temperature (Engelhardt,

2004) and sonic velocity (G. Lamorey, pers. comm.) were measured down the borehole.

Coincident with the coring effort, glaciological studies focused on quantifying the geometry, flow field, and mass balance of SDM. Calculations of the flux divergence from measurements of surface velocities and ice thickness (Nereson, 1998), direct measurements of submergence velocities (Hamilton, 2002), and depth-profiles of the vertical strain rate (Hawley and others, 2004; Zumbege and others, 2005), all indicate that the divide is currently near steady-state but the flanks are thinning at a rate of 25 to 50 mm a⁻¹.

Ice thickness and internal-layer stratigraphy across SDM were obtained using ground-based radio-echo sounding (Jacobel and others, 1996; 2000). Nereson and others (2000) used a kinematic ice-flow model, constrained by the pattern of the internal layers, to conclude that (1) the layer-pattern is consistent with an orographic pattern of precipitation (i.e. driven by the presence of the divide) that has prevailed for most of the Holocene, and (2) the flow divide has migrated northward at a rate of ~0.5 m a⁻¹ for the past several thousand years. Based on the first conclusion, Nereson and others (2000) inferred that SDM has been a locally elevated feature for most of the Holocene. They also concluded that no large-scale thickness changes have taken place at SDM over the past 2 ka. Thickness changes prior to 2 ka BP, however, could not be ruled out.

Waddington and others (2005) used a time-dependent, 1-D ice-flow model to explore the range of possible histories of accumulation and ice dynamics at SDM. They focused on the past 25 ka (the upper 700 m of the core) and used the model to investigate combinations of ice-thickness, divide-position, and accumulation-rate histories that matched the observed age-depth profile. Combinations with physically unrealistic accumulation-rate histories were rejected. They concluded that SDM was between 200 and 400 m thicker at the LGM, and that thinning likely took place between 16 and 2 ka BP.

MODELING APPROACH

Our approach is similar to that of Waddington and others (2005) but as well as matching the depth-age relationship, we also use the observed temperature profile and the shape of radar-detected isochrones (including the surface topography) as targets for modeling. We use a two-dimensional, full-stress thermo-mechanical flowband model (Price and others, Chapter 2) that solves the two-dimensional momentum-balance equations (i.e. plane strain) and the two-dimensional, advective-diffusive heat equation using the Finite Volume Method. When solving the momentum equations, we make the simplifying assumption that $\rho(x,z,t)=\rho_{\text{ice}}$. When solving the heat equation, the density and thermal properties in a 60 m-thick firn layer are accounted for using approximations summarized by Paterson (1994, p.14). The domain for the momentum equations includes ice within 20 km north and south of the present-day flow divide. The domain for the heat equations includes an additional 1.5 km-thick layer of bedrock beneath the ice. Bedrock elevations, based on measurements of surface elevation and ice thickness (Raymond and others, 1995) are held constant throughout the model run; isostatic rebound is not taken into account.

We start by assuming that climate (accumulation rate and surface temperature) during the last interglacial (120 ka BP) was similar to today. Then we run the model forward in time using the histories shown in Figure 3.2. The accumulation-rate history is supported by work of Spencer (2005) back to 30 ka BP. Thus, we restrict our analysis to the past 30,000 years. Prior to that time we extrapolate linearly back to the modern value at 120 ka BP. The surface temperature history comes from the interpretation of stable isotopes along the ice core (Schilla and others, in prep.). Geothermal flux is assumed constant (0.071 W m^{-2} , based on measurements and calculations by G. Clow (pers. comm.) and Engelhardt, 2004).

We then use the model and the observations to explore the effects of different combinations of ice-dynamic histories (ice thickness and ice-divide location). In steady state, ice flux at the lateral boundaries balances accumulation integrated over the surface; domain volume is held constant over time but the surface shape is allowed to vary. To force thinning at a desired rate and time, ice flux at the lateral boundaries is increased relative to the balance flux. Similarly, to force migration of a flow divide, the boundary flux is changed asymmetrically.

At the end of each 120 ka run, model results are compared with observations. Internal layers (isochrones), modeled by tracking particles initially at the surface through the evolving velocity field, are compared with the observed internal layers (Jacobel and others, 1996, 2000) and with the observed age-depth profile (Brook and others, 2005; Taylor and others, 2005). The model surface shape is compared with the present-day surface shape (Raymond and others, 1995) and the model temperature field is compared to the present-day temperature profile measured down the borehole (Engelhardt, 2004).

To illustrate the relative effects of past climate and ice dynamics on the present-day characteristics of the ice sheet, we generate a reference state in which the model is forced solely by the climate (accumulation and surface temperature) history shown in Figure 3.2. The reference state assumes that ice dynamics have remained unchanged; that is, the core site has been a flow-divide for the past 120 ka, there has been no flow enhancement, and there have been no changes in ice thickness.

Comparison of the reference-state model with observations (Figure 3.3) shows that the model-observation misfit is acceptable for the surface shape, less acceptable for the age-depth profile, poor for the temperature-depth profile, and poor for the divide-bump-amplitude profile beneath the divide (hereafter, “bump-amplitude profile”). To reduce the misfit, we include the effects of ice dynamics in the model: (1) the timing of initiation of divide flow, and divide migration; (2) the magnitude and timing of ice-thickness changes; (3) ice-flow enhancement. An

additional process that affects the evolution of the stratigraphy is the amount and timing of wind scouring of accumulation at the divide.

History of proximity to flow-divide

Isochrones beneath a stable divide that is frozen to its bed are arched upwards because of the unique stress, strain-rate, and viscosity fields that exist beneath a flow divide (Raymond, 1983); for a given depth, ice beneath a divide is older than beneath a flank and the age-depth profile at a divide is older than at a flank site of similar thickness. Similarly, relatively less vertical advection at a divide leads to warmer ice there than beneath a flank of similar thickness (Paterson and Waddington, 1986; Dahl-Jensen, 1989). As a flow divide migrates away from a fixed position, the velocity field at that position transitions from divide-like to flank-like. In turn, the age-depth profile there will become younger and the temperature-depth profile will become cooler, relative to the case of a stationary divide. Divide migration will also “smear” an existing divide bump laterally, decreasing its amplitude and tilting its axis in the direction of migration (Nereson and Waddington, 2002).

To quantify the effects of divide-proximity on internal layer shape, we plot the divide-bump amplitude as a function of depth (the “bump-amplitude profile”). The amplitude and the depth of its maximum are primarily functions of the time elapsed since the initiation of divide flow; for two sites of similar thickness, the maximum bump amplitude is larger, and occurs deeper, at the site experiencing divide flow for longer. We define the bump amplitude for any layer relative to some datum and, as in previous work (Conway and others, 1999; Pettit and others, 2003; Martín and others, 2006), we define that datum by a spline fit to the layer shape outside of the region affected by divide flow.

Flow divergence beneath a divide acts to separate particles that were in close proximity at the surface. This presents a challenge when tracking particle trajectories to obtain an accurate description of deep (old) layers; particle paths originate in a narrowly focused region near the flow divide but any divide motion

results in those particles being advected (horizontally) out of the model domain. This complication, inherent in any explicit particle-tracking scheme, makes it difficult to account for all possible transitions between divide and flank flow. We avoid this complication by accounting for only two of the many possible transitions between flank and divide flow: (1) a flank that becomes a divide instantaneously, and (2) a divide that migrates laterally late in the model run (near the present, in which case horizontal advection has only a minor effect on shallow layers).

The first transition requires a small modification of the layer-tracking sub-model but no changes to the flow model. In the model, a divide exists near the core site at all times. Prior to the onset of divide flow, however, the true layer shapes in the divide region (within a distance of about ± 5 ice-thicknesses from the divide) are replaced by a spline fit to the layer shapes outside of this region; the layer-tracking model treats layers beneath the divide as if they experienced flank flow rather than divide flow (the age-depth profile for this “false” flank is identical to that for a true flank site). After the onset of divide flow, this constraint is removed and new and pre-existing layers are everywhere advected through the true flow field.

An instantaneous change from flank to divide flow is accounted for in the layer-tracking model but not in the flow model. This simplification biases the model temperature field (it is too warm because it assumes that a divide has always been in place). In steady state, however, the temperature difference between the divide and a flank of similar thickness is ≤ 0.5 K, which is similar to the uncertainty associated with matching the observed temperature profile (see Appendix); the consequence of the simplification is within our tolerance for matching observations. Model temperature profiles shown below are an average of those at the divide and at a nearby flank site of similar thickness.

The second type of transition, divide migration occurring late in a model run, is handled in a physically realistic manner; migration is forced by increasing the mass flux at one lateral boundary and decreasing it by an equal amount at the opposite boundary. The change in flux needed for a desired rate of migration is found through experiments. We specify divide migration for the past 2 ka, based on

work by Nereson and others (1998b). The velocity field itself changes during this transition so there are no additional complications with the interpretation of the modeled temperature field.

Ice-thickness history

The ice-thickness history has a strong influence on the characteristics (depth-age relationship, depth-temperature relationship and pattern of internal stratigraphy) of the ice sheet that we observe today. For example, consider two ice domes X and Y that are the same thickness today. Dome X has remained constant while dome Y was thicker in the past. Annual layers at dome Y have undergone more thinning than those at dome X, so (if the histories of accumulation were the same at both sites) there are more annual layers within a given depth interval at dome Y than at dome X. As a result, the age at a given depth at dome Y is older than the age at the same depth at dome X.

The depth-amplitude profile is also affected by the ice-thickness history. Assuming that divide flow started far in the past but simultaneously at domes X and Y, thinning of dome Y enhances the difference between divide and flank-flow regimes relative to dome X; the response to thinning at the divide and flanks is nonlinear. As a result, the bump amplitude and the depth of its maximum will be relatively larger at dome Y.

The temperature profile is affected by thickness changes in a complex way. Considering domes X and Y again, and assuming the same climate history and the same geothermal flux, dome Y, initially thicker than dome X, was also better insulated and thus warmer at all heights above the bed. The steady-state temperature profile at dome X is maintained, but the temperature profile at dome Y depends on both the initial temperature field and on the magnitude and duration of thinning, which increases the vertical advection of cold surface ice. Either a large thickness change over a long period of time or a small thickness change over a short period of time could result in a temperature profile today that is cooler at dome Y than at dome X, even though it was initially warmer.

Ice-thickness changes at the margins propagate up to the divide, and the surface topography adjusts to a new steady state that is consistent with the new thickness distribution and the climate. Under modern conditions at SDM, the time required for surface readjustment is approximately 700 a (Nereson and others, 1998a); the modern surface shape has a memory of thickness changes within the past 700 a but it is insensitive to thickness changes prior to 700 a ago.

Here, we assume that SDM was at least as thick and likely thicker than today during the last glacial period. In the model, thinning at the margins is initiated by increasing the flux relative to the balance flux. When thinning occurs, we specify that the average rate of thinning over the domain is constant.

Evolution of ice-flow enhancement

Measurements along the ice core and observations down the borehole indicate that the lower ~200 m of the column consists of large interlocking ice crystals. Ice temperature in this depth-range is warmer than -10°C (Figure 3.3a), and it is likely that the ice has been dynamically recrystallized (Diprinzio and others, 2005). From 200 to 300 m above the bed, ice-crystal size decreases and the c-axis fabric becomes tightly oriented about the vertical. This region is likely composed of ice-age ice that has not yet undergone recrystallization.

A rigorous incorporation of ice-crystal properties, their influence on the flow field, and their evolution in time and space is beyond the scope of this work. Here, we instead parameterize the mechanical effects of the evolving ice-crystal fabric through a scalar enhancement factor, $E(x,z,t)$ (hereafter simply E). Relative to isotropic ice, the “lower layer” at SDM (0 to 200 m from the bed) is isotropically stiff. The “upper layer” (200 to 300 m off the bed) is stiff to vertical compression, soft to horizontal shear, and thus anisotropic (Pettit, 2003). This combination effectively results in a “false bed”; the majority of deformation in the ice column takes place above the lower layer (Pettit, 2003). We use $E < 1$ for stiff ice and $E > 1$ for soft ice, but a single value for E cannot be used to represent ice-flow that is soft to horizontal shear and stiff to vertical compression. To get around this problem we

use the following procedure to approximate ice-crystal properties in the upper layer: near the divide, vertical compression (and longitudinal extension) dominates over horizontal shear; the opposite holds true away from the divide. Based on experimental work by Jun and others (1996), Wang and Warner (1999) presented a method to calculate E for steady-state flow in tertiary creep. E_C and E_S , the enhancement factors for flow experiencing *only* vertical compression or *only* horizontal-shear strain, bound the values of E ; that is, for combined compression and shear, $E_C < E < E_S$. Following this approach, for each time step we calculate a stiff value ($E < 1$) for ice near the divide (where vertical compression dominates) and a soft value ($E > 1$) for ice on the flanks (where horizontal shear dominates). In between, E varies smoothly according to the relative contribution of vertical compression to the total strain (Figure 3.4).

Values for E_C and E_S are chosen so that our modeled, modern-day, vertical-velocity shape function at the divide is a good match to that from a steady state model of SDM that accounted for the effects of ice-crystal properties (Pettit, 2003). Figure 3.5a shows the vertical-velocity shape function from modeling of Pettit (2003), our approximation of that shape function (derived from our favored map of E - Figure 3.4), and several other shape functions for reference. Figure 3.5b shows horizontal-velocity shape functions at locations 1, 2, and 10 ice-thicknesses from the divide. These are also very similar to those from Pettit (2003) with the exception that our “false bed” effect is slightly more pronounced. Away from the divide, we constrain E by choosing E_C and E_S so that the modeled present-day surface shape matches the observations.

The evolution of ice-crystal properties is not known, so we start by assuming that a weak, c-axis-oriented fabric initially developed in ice-age ice and that ice that is now 700-800 m below the surface is a remnant of this initially much thicker layer. On-going strain rotates the c-axes of crystals in this layer towards the vertical, strengthening the crystal fabric. The fabric in this layer is “reset” at depth due to dynamic recrystallization at temperatures warmer than about -10°C . Following this scenario, a thick layer of ice-age ice with a weak c-axis fabric

evolves over time into a thin, deep layer with a strong c-axis fabric. Near the bed, recrystallization continually resets the c-axis fabric.

Using this as a framework, we calculate E using the following assumptions: (i) no significant flow enhancement ($E=1$) occurs prior to 30 ka BP. Starting at 30 ka BP, flow enhancement strengthens over time; E_C and E_S change linearly from a value of unity to the present-day values (those that result in the E field shown in Figure 3.4). (ii) when $E \neq 1$, the lower $\sim 20\%$ of the ice column always consists of recrystallized ice. This assumption is reasonable because model results for the range of thicknesses examined here indicate that the -10°C isotherm is always close to $\sim 0.2 \times H$ off of the bed, regardless of the total column thickness. (iii) the transition from ice-age ice to Holocene-age ice occurred 18k yrs ago. This timing comes from interpretation of the depth-profiles of stable isotopes and age measured at SDM. For ice younger than 18 ka BP we set $E=1$. Ice older than 18 ka BP is forced to evolve through time so that the scalar enhancement factors today are consistent with those shown in Figure 3.4. Figure 3.6 shows maps of our favored scalar enhancement at various times during the model run.

Divide Scouring

Near topographic divides, removal of snow by wind scouring can be significant (Fisher and others, 1983). Spatial variations in accumulation affect the vertical velocity field, which affects the age-depth and the temperature-depth profiles. Relative to a non-scoured divide, annual layers beneath a divide that has been subjected to scouring are thinner (making the age-depth profile older), causing upwarping of layers beneath scoured divides (Vaughan and others, 1999). Here, we implement scouring in a manner similar to that used by Nereson and Waddington (2002); the spatial reduction in accumulation rate is described by one cycle of a cosine-bell curve centered on the divide. We estimate the amplitude of the curve (the scouring rate at the divide) by running the model to find values that best fit the observed bump-amplitude profile.

MODEL RESULTS AND SENSITIVITY

Using the approach discussed above, we have run many forward models using a prescribed climate history (Figure 3.2) and various combinations of ice-dynamic histories. Many combinations of ice-thickness, the timing of the onset of divide flow, and divide scouring can match the observations. We reduce the dimensionality of the problem by specifying the divide migration rate based on work by Nereson et al., (1998b), and we search for a model result that yields an “acceptable” match to observations (other combinations of model results may also lead to acceptable solutions).

Figure 3.3 shows observations (filled circles), and results from our preferred model (solid-black lines). The histories that provide this match are:

- (1) divide flow starting 3 ka ago and northward migration of the divide 2.5 ka ago;
- (2) total thinning of 350 m from 15 ka to 14 ka ago;
- (3) flow enhancement becoming non-trivial ($E \neq 1$) 30 ka ago and changing thereafter as described in the text above;
- (4) divide-scouring, at a rate of 2.5 mm a^{-1} , starting 3 ka ago (coincident with the onset of divide flow) and continuing today.

Below we discuss what we deem to be an “acceptable” match, and we also investigate the sensitivity of our preferred model to perturbations to the time of onset of divide flow, to the magnitude and timing of thinning, to the flow enhancement caused by fabric-evolution, to divide scouring, and to the accumulation-rate history.

Acceptable match

Age-depth relationship: Uncertainties in the observed age-depth profile at SDM increase with depth and we use uncertainties given by Taylor and others (2005) and

Brook and others (2005) to define an “envelope” of uncertainty, which is shown in the age-depth misfit figures (Figures 3.7a, 3.8a, 3.9a, 3.11c, 3.12c, 3.13c). We assume that this uncertainty envelope is representative of the 1σ uncertainty. Although our goal is to find models that fit the observations within this envelope, we are unable to fit all observations to this level of acceptability (Figure 3.3c). Possible reasons for this are discussed below.

Temperature-depth relationship: We do not attempt to match the temperature profile in the upper 200 m (Figure 3.3a). Variations in temperatures in this upper 200 m have been attributed to recent (past 1.5 ka) changes in surface temperature (Engelhardt, 2004) but there is no evidence for such changes in the proxy surface temperature record (Schilla et al, in prep.). Further, this signal is not observed in other temperature profiles from nearby borehole (G. Clow, unpublished data). Deeper than 200 m, we accept models when the magnitude of the temperature difference between the model and observations is $\leq 0.5^\circ\text{C}$ (see Appendix).

Bump-amplitude profile: Based on uncertainties associated with picking the depth of radar-detected layers and with defining the amplitude of bumps (Figure 3.3b), we accept a misfit in the profile amplitude of 5 m and a mismatch in the depth of the amplitude maximum of 100 m.

Surface shape: When fitting the surface shape (Figure 3.3d), we accept a misfit of magnitude 5 m. Over 20 km, the distance from the divide to the domain edge, this translates into a slope error of $\sim 2.5 \times 10^{-4}$, which is $<5\%$ of the mean, modern-day slope over the same distance.

Sensitivity to the onset of divide-flow

Figure 3.7 shows results from our preferred model (divide flow starting 3 ka BP) and results for divide flow starting at 6 ka and 1.5 ka BP. In all cases, northward migration of the divide starts after 2.5 ka BP, and scouring of accumulation at the divide is coincident with divide flow. Misfits for the present-day surface shape and temperature profile are not shown because they are insensitive to the onset of divide flow. The misfit for the bump-amplitude profile (Figure 3.7b) illustrates

clearly the sensitivity to the onset-time; both the maximum amplitude of the bump and the depth of the maximum increase with time. Although our preferred timing for onset (3 ka ago) provides the best fit to observations, evolution of the bump amplitude profile is also sensitive to the evolution of flow-enhancement (discussed below).

Sensitivity to thickness change

Figure 3.8 shows results for our preferred model (thinning of 350 m) and results for 250 m and 450 m of thinning prescribed between 15 ka 14 ka BP. Misfits for the present-day surface shape and bump-amplitude profile are not shown because they are insensitive to thinning that long ago¹. Figure 3.9 shows the same misfits for total thinning of 350 m, occurring during the early (20-15 ka, 20-12 ka, 15-14 ka BP), middle (15-10 ka and 15-2 ka BP), and late (7-2 ka BP) Holocene.

In Figure 3.8a, the range of thinning specified does not affect the age-depth relationship in the upper section of the ice column. However the modeled ages that include 250 m of thickness change are too young at depth (more than about 600 m below the surface), while those that include 450 m of thickness change are too old (Figure 3.8a). The model that assumes 350 m of thinning is a reasonable compromise.

For the reference state (no change in thickness since the LGM), temperatures at the bed are more than 3°C colder than observed (Figure 3.3a). The misfit can be reduced if we assume ice was thicker in the past (the bed was better insulated from the cold atmosphere). Figure 3.8b shows that the misfit improves significantly for models that include thicker ice in the past; results show that the bed is still too cool if we assume the ice was just 250 m thicker in the past but the match improves if we assume the ice was 450 m thicker than present. There is,

¹ Based on our work and previous studies by Nereson and others (1998b) and Pettit (2003), thinning of SDM ended more than 2k yrs ago. Thinning prior to ~700 yrs ago has minimal influence on the present-day surface profile. Likewise, results indicate that divide flow ban after most of the thinning had occurred and so the choice of thinning history has a minor influence on the bump-amplitude profile.

however, a tradeoff: histories that include large past-ice thickness require higher rates of thinning in order to reach the modern thickness. This thinning increases advection of cold ice to depth. The deeper section of the SDM temperature profile (Figure 3.3a) is remarkably linear, suggesting moderate thinning and/or that thinning occurred long ago.

Figure 3.9b compares results for thinning from 15-14 ka BP with those for thinning from 15-2 and 7-2 ka BP. For the latter two cases, the age-depth profile is too old at all depths and the temperature profile is too cold (Figure 3.9, crosses and asterisks). For models with thinning from 20-12, 20-15, 15-14, and 15-10 ka BP, the fit to the temperature-depth profile is acceptable and similar. For thinning from 20-12 and 20-15 ka BP, deep ice is too young (Figure 3.9a, squares and diamonds). For thinning from 15-14 ka BP, the misfit is mostly within the error envelope or very near to it (Figure 3.9a, circles). For thinning from 15-10 ka BP all but one of the misfit values are within the range of error (Figure 3.9a, triangles). Although we are unable to match the observed profiles of temperature and age perfectly, the fit improves when thinning occurs early in the Holocene.

Sensitivity to flow enhancement

Figure 3.10 shows results from our preferred model and results for: (i) no enhancement ($E(x,z,t)=1$ everywhere); (ii) no enhancement in the upper column, but a stiff layer near the bed (a “false bed”); (iii) 50% greater contrast between E_c and E_s in the upper layer (to simulate a more tightly focused c-axis fabric).

For $E=1$, we are unable to find any combinations of ice-thickness, divide-flow onset time, and divide scouring that provide an acceptable match to the observations; the temperature profile is too cold (Figure 3.10a, dashed line); matching the bump-amplitude profile requires the onset of divide flow to be more than 3 ka ago, but matching the depth of the amplitude-maximum requires the onset of divide flow to be about 3 ka ago (Figure 3.10b, dashed line); the modeled age at depth is too young (Figure 3.10c, dotted line and squares).

Including a layer of stiff layer near the bed in the model decreases the mismatch to the temperature profile considerably (Figure 3.10a, dotted line). It also shifts the entire bump-amplitude profile upwards (Figure 3.10b, dotted). The age mismatch at depth is also decreased, although the modeled age at depth is still too young (Figure 3.10c, triangles). The stiff layer alone, however, results in a surface profile that is much too steep (Figure 3.10d, dotted line).

Including a parameterization for the effects of the evolution of the c-axis fabric on ice flow improves the fit to all observations. Increasing the contrast between E_c and E_s by 50%, to simulate a tighter c-axis fabric, has a small effect on the model mismatch to the measured temperature and bump-amplitude profiles (Figures 3.10a and 3.10b). The surface shape, however, is too shallow (Figure 3.10d, dash-dot line) and the age-depth profile is too old at depth (Figure 3.10c, crosses).

To examine model sensitivity to the history of E , we vary the “start” time, the time at which E takes on some non-trivial value, and the “end” time, the time at which E reaches its full, modern value (that shown in Figure 3.4). Figure 3.11 shows results from our preferred model (fabric evolution starts 30 ka BP) and results for cases where the start time is changed by ± 10 ka. Also shown are results for cases where the end time for E is changed from its favored value (today) to end times of 5 ka and 10 ka BP.

Results show that the longer enhancement has been active, the less total thinning and/or the less rapid thinning is required to fit the observed age-depth profile. This is because when the layer representing ice with a c-axis fabric is active, $E > 1$ results in preferential thinning of layers there². Stiff basal ice inhibits the vertical advection of cold surface ice, so that if enhancement is active for longer, the ice column is warmer than if enhancement is active for a short time or not at all. At SDM, this effect is small compared with the effect of ice thickness changes.

² Recall that, prior to the onset of divide flow at 3 ka BP, layers in the divide region are treated as if they experience flank flow. When a c-axis fabric is active, flow on the flank is “soft” to surface-parallel shear.

Sensitivity to divide scouring

Figure 3.12 shows results for our preferred model (divide-scouring of 25 mm a^{-1} when the divide is in place) and results for scouring of 12 and 50 mm a^{-1} (a factor of two change in either direction). Misfits for the age-depth profile, the temperature-depth profile, and the present-day surface shape are not shown because they are insensitive to the prescribed scouring; the rate of scouring is small compared to the accumulation rate (less than 3%) and scouring occurs over the past 3 ka only. Scouring has a small effect, but results show that increased local scouring at the divide causes the bump-amplitude to increase, and the position of the maximum shifts closer to the surface (Figure 3.12), as shown previously by Nereson and Waddington (2002).

Sensitivity to accumulation-rate history

Figure 3.13 shows the model-sensitivity to uncertainties in the accumulation-rate history. Spencer (2005) estimated a 2σ -uncertainty of 26% for his accumulation-rate history. Independent estimates of Holocene accumulation at SDM are within 10% of Spencer's values. Here we show the effects of changing the Spencer-accumulation history by $\pm 10\%$ of its mean value over the Holocene. We also show results for two cases where values of accumulation rate have been perturbed randomly by the estimated uncertainty.

DISCUSSION**Preferred history**

Although many combinations of ice-thickness, the timing of the onset of divide flow, and divide scouring can match the observations, some physically unrealistic possibilities can be eliminated. Results indicate that modestly thicker ice in the past is a requirement for fitting both the temperature- and age-depth profiles. While the

fit to the observed age-depth profile is somewhat dependent on the history of enhancement, the observed temperature profile introduces a firm constraint. A large past ice thickness results in temperatures that are too cold at all heights above the bed and, in particular, too cold at the bed. Also, a past ice thickness that is too large leads to temperatures at middle depths that are too cold, resulting in a temperature profile that is “bowed” with respect to the observed profile. A similar bowing occurs if thinning takes place too close to the present. On the other hand, if thinning occurred prior to ~10 ka BP, cold ice at middle depths is absent and model temperatures fit the observations better³.

Our modeled age-depth profile falls outside the envelope of uncertainty at several points (e.g. circles in Figure 3.7a): near the surface where we do not account for the effects of firn-densification, and so expect the model ages to be too old, and in the lower ~30% of the ice column. In the lower 30% of the ice column, the mismatches for thinning from 15-14 ka BP fall just outside of the 1 σ error envelope. For the case of thinning from 15-10 ka BP, the mismatch at ~3/4 depth is much larger. Overall, thinning from 15-14 ka BP results in a smaller overall mismatch to the observed depth-age profile.

Figure 3.3 shows that the age-depth profiles for the reference and favored models are similar, but the pattern of Raymond bumps beneath the divide is very different. This observation, along with Figures 3.7 and 3.8, demonstrates an important tradeoff: for the same accumulation-rate history, the age-depth profile at a divide can be matched either by changing the ice-thickness history, or by changing the length of time the divide has been in place, or by choosing some combination of the two. The relative contribution from each can be untangled if the divide age can be constrained. Here, that constraint is given by the bump-amplitude profile, which requires that divide flow at the core site started recently. Hence, thinning is required to fit the age-depth profile, in agreement with our interpretation based on fitting the temperature profile.

³ A characteristic, advective timescale for heat flow is given by $\tau = H \div \dot{b}$. For Siple Dome during the Holocene, $\tau \sim (10^3 \text{ a}) \div (10^{-1} \text{ m a}^{-1}) = 10^4 \text{ a}$.

Model results indicate that the effects of ice-crystal properties on flow, for example crystal fabric, must be included in order to match the observed bump amplitude profile. The observed bump-amplitude profile trends towards zero several hundred meters above the bed. Because the divide bump is a result of the difference between divide and flank flow regimes, this difference must then also trend towards zero several hundred meters above the bed. This behavior is difficult to mimic in the model without the false-bed effect. The general pattern of flow enhancement included in the modeling here, stiff ice near the bed overlain by a layer that deforms more easily in shear, has also been inferred in studies of ice stream tributaries near Byrd Station (Wang and others, 2003). A similar combination of basal layers has been hypothesized to exist near the bed of the East Antarctic Ice Sheet. That work, based on flow modeling constrained by ice-core measurements (Wang and Warner, 1999), and observations made using polarized, ice-penetrating radar (Fujita and others, 1999) suggest that this combination of basal layers may be widespread in both West and East Antarctica.

Results show that the effects of more thinning and more recent onset of divide flow offset one another when fitting the observed age-depth relationship (the converse is also true). Additional observations are needed to separate the effects of changes in ice thickness from changes in divide location. Depth profiles of temperature and bump amplitude provide additional constraints; at SDM the temperature-depth profile is more sensitive to ice-thickness change and the bump-amplitude profile is more sensitive to the divide history. This is partly because divide flow and thinning are not coincident for any length of time at SDM. Nevertheless, it is likely that the temperature-depth profile will always be more sensitive to the ice thickness history than to the history of flank-versus-divide flow: for the same ice thickness at SDM, the maximum temperature difference for a site experiencing exclusively flank versus exclusively divide flow is $\sim 0.5^{\circ}\text{C}$. This difference will be less for a divide that has experienced some combination of the two flow regimes during its history. In contrast, thickness changes of several

hundred meters have a significant influence (i.e. temperature differences of several °C) on both the basal temperature and the shape of the temperature-depth profile.

Synthesis

Previous work indicates that the ice sheet in the region of SDM has thinned since the LGM (Waddington and others, 2005; Denton and Hughes, 2002). Our work suggests ~350 m of thinning since the LGM, which is similar to the range of 200-400 m suggested by Waddington and others (2005), but less than half the amount of thinning required by the reconstruction of Denton and Hughes (2002). While the timing of thinning is not well known, the observed temperature profile provides a constraint that suggests most of the thinning took place early in the Holocene. Additional support for early Holocene thinning comes from recent studies: (i) comparison of the stable isotope histories from Byrd and SDM suggest that the relative elevation changed about 200m between 20 and 12 ka BP (Schilla and others, in prep.). This magnitude and timing of change is consistent with our results if the elevation of SDM decreased while that at Byrd remained unchanged during that time; (ii) Todd and others (2005) used exposure-age dating of lateral moraines of Reedy Glacier (RG, Figure 3.1) to estimate that ice was still about 250 m thicker than present at 14.2 ka BP. Roughly half of that 250 m thinned prior to ~7 ka BP and, of that half, most thinned prior to 9 ka BP.

Marine-geological evidence from the Ross Sea indicates that ice streams continued to flow during the last glacial period (Anderson and others, 2002). Results from experiments with a thermo-mechanical model of ice streams indicate that although ice-streams may have slowed down during the glacial period, they probably did not stagnate (Parizek and others, 2003). It is likely that post-LGM thinning at SDM occurred in response to acceleration and thinning of the surrounding ice streams. Increased flow rates could occur as Holocene warming penetrated to the bed of the ice streams; Parizek and others (2003) suggested that Holocene warming would reach the bed of the Ross Ice Streams sometime after 13 ka BP, several thousand years after our preferred start time for thinning.

Alternatively, acceleration and thinning of the ice streams could be a response to perturbations in basal stress at the grounding line caused by global sea-level rise.

Melt-water pulse 1A (MWP1A), a period of rapid sea-level rise of more than 20m at about 14.5 ka BP (Fairbanks, 1989), is a potential source for such forcing. Present-day observations show that perturbations near the grounding line of fast-flowing outlet glaciers and ice streams propagate rapidly upstream (Joughin and others, 2003; Rignot, 2002; Shepherd and others, 2001, 2002). Experiments using a depth-averaged, full-stress, flow model can reproduce observations from Pine Island Glacier in the Amundsen Sea sector of west Antarctica (Payne and others, 2004). In that model, significant thinning occurs as far as ~250 km inland in only 20 years. These results may be conservative with respect to the impact of MWP1A on ice-stream activity for several reasons: (i) in the model, the upstream limit of propagation (250 km inland) occurred at a slip/no-slip boundary that was prescribed in the model. In reality the boundary could probably migrate; (ii) the model examined the response to a single, step-wise perturbation near the grounding line whereas sea-level rise during MWP1A continued for several hundred years; (iii) in that model, the perturbation affected only the ice thickness. In reality, additional interaction between evolving stresses in the ice and basal conditions could lead to faster propagation and/or larger propagation distances (Price and others, Chapter 4).

Our thinning history is not necessarily inconsistent with previous work. Conway and others (1999) used a combination of geologic evidence from the Scott Coast and the Transantarctic Mountains, and glaciological data from Roosevelt Island to suggest that grounding line retreat began after ~8 ka BP and proceeded steadily to the present day. However the geologic constraints come from the western margin of the Ross Embayment; it is possible that grounding line retreat in the central sector occurred earlier. Internal stratigraphy of Roosevelt Island indicates that a stable divide did not exist there until ~3 ka BP. Conway and others (1999) interpreted this date as the time when the grounding line migrated past the island. An alternative explanation is that Roosevelt Island was a dome for much of

the Holocene but only after ~3 ka BP were conditions such that it froze to the bed, allowing a divide-bump to form. Interestingly, this timing is similar to our estimate for the time of the onset of divide-flow at SDM.

CONCLUSIONS

Our study shows how use of an ice flow model constrained by multiple datasets can help to unravel the history of an ice sheet. Waddington and others (2005) used the depth-age profile and flow modeling to determine a range of thickness-change and divide-flow histories that required reasonable accumulation-rate histories. Here, data on ice temperature add a strong constraint to the timing and magnitude of thinning, and data describing the spatial pattern of internal layers constrain the time at which a stable divide becomes frozen to the bed. The latter becomes important when trying to separate the competing effects of thickness change and divide-flow history on the age-depth profile.

Results indicate that ice-crystal properties have an important effect on the flow field and that these need to be accounted for in order to match the observations. This finding points to the need for improved understanding of the evolution of ice fabric in ice sheets, and the influence of fabric on ice flow.

Our preferred reconstruction calls for approximately 350 m of thinning at SDM. The timing of thinning (between 15 and 14 ka BP) is coincident with the time of melt-water pulse 1A, when global sea level increased by more than 20 m in a few hundred years. We suggest that the effects of the rise in sea level propagated rapidly inland and initiated thinning at SDM.

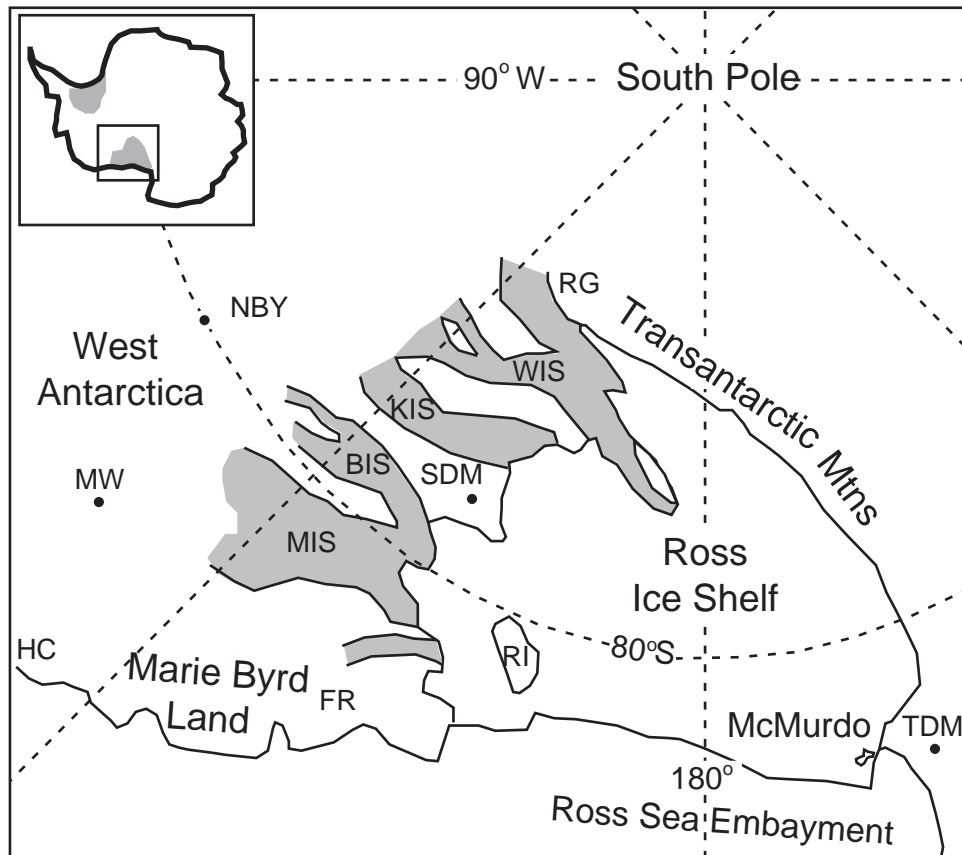


Figure 3.1: Siple Dome location Map. Siple Dome (SDM), Taylor Dome (TDM), Byrd Station (NBY), Mount Washche (MW), Ford Ranges (FR), Hobbs Coast (HC), Reedy Glacier (RG), Whillans (WIS), Kamb (KIS), Bindschadler (BIS), and MacAyeal (MIS) Ice Streams.

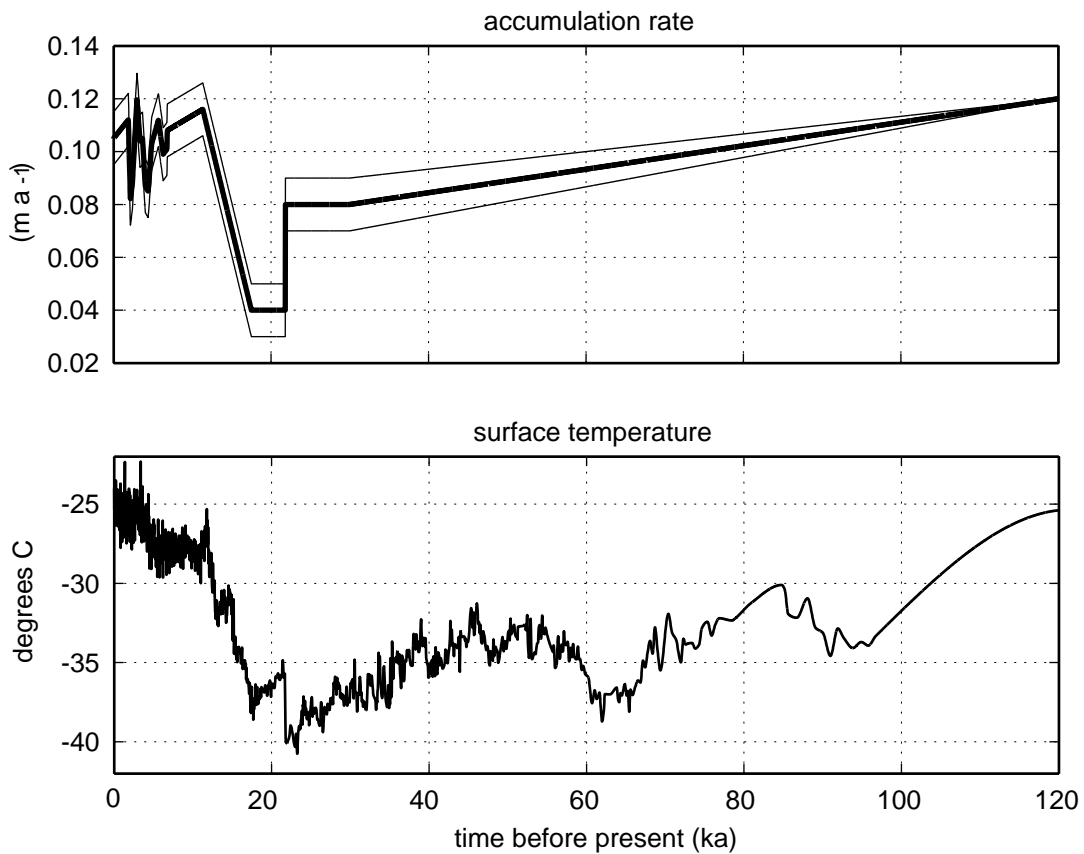


Figure 3.2: Surface temperature and accumulation-rate histories for Siple dome. (a) Surface temperature and (b) accumulation-rate histories used to force heat and momentum balance models. . Surface temperatures are from Schilla and others (in prep.) and accumulation rates are from Spencer (2005). In (b), the dashed lines denote the upper and lower bounds on the accumulation rate history, tested in Figure 13.

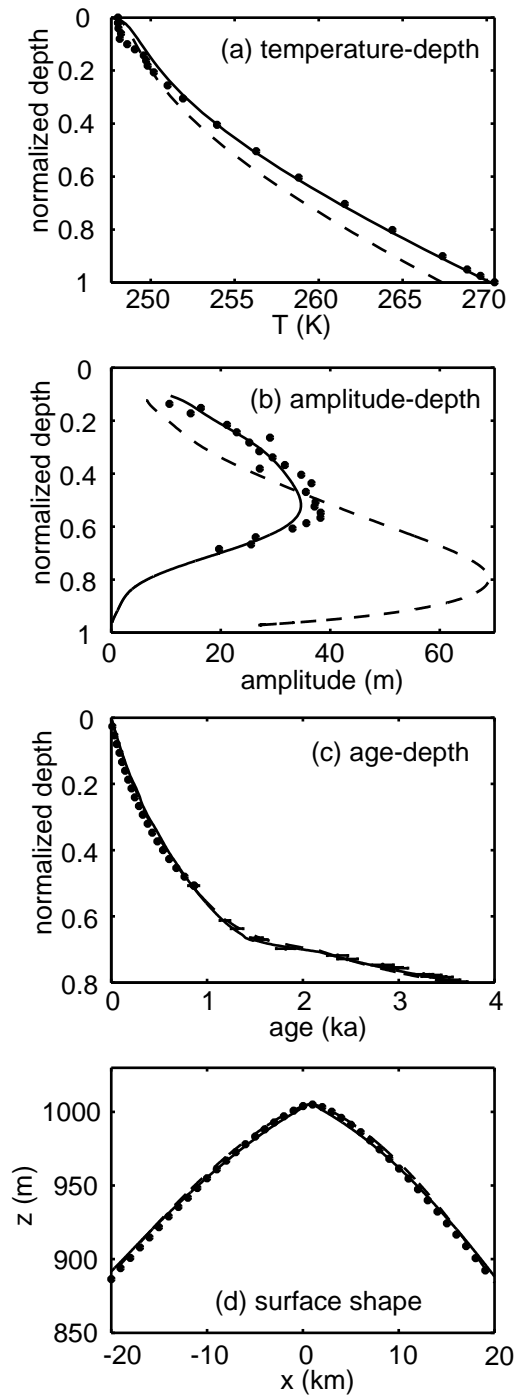


Figure 3.3: Modeled (lines) and observed (dots) variables at the Siple Dome core site. Solid and dashed lines represent results from the favored and reference models, respectively. (a) temperature-depth profile (b) amplitude-depth profile (observed layers from which we can estimate a divide-bump amplitude are limited to the region from $z/H \sim 0.1-0.7$) (c) age-depth profile (e) surface elevation.

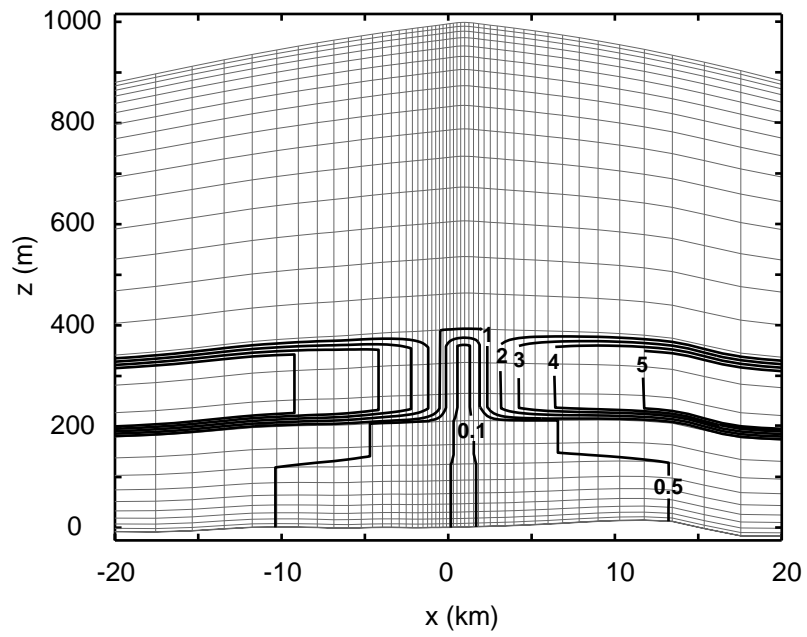


Figure 3.4: Map showing the favored value of the present-day enhancement factor.

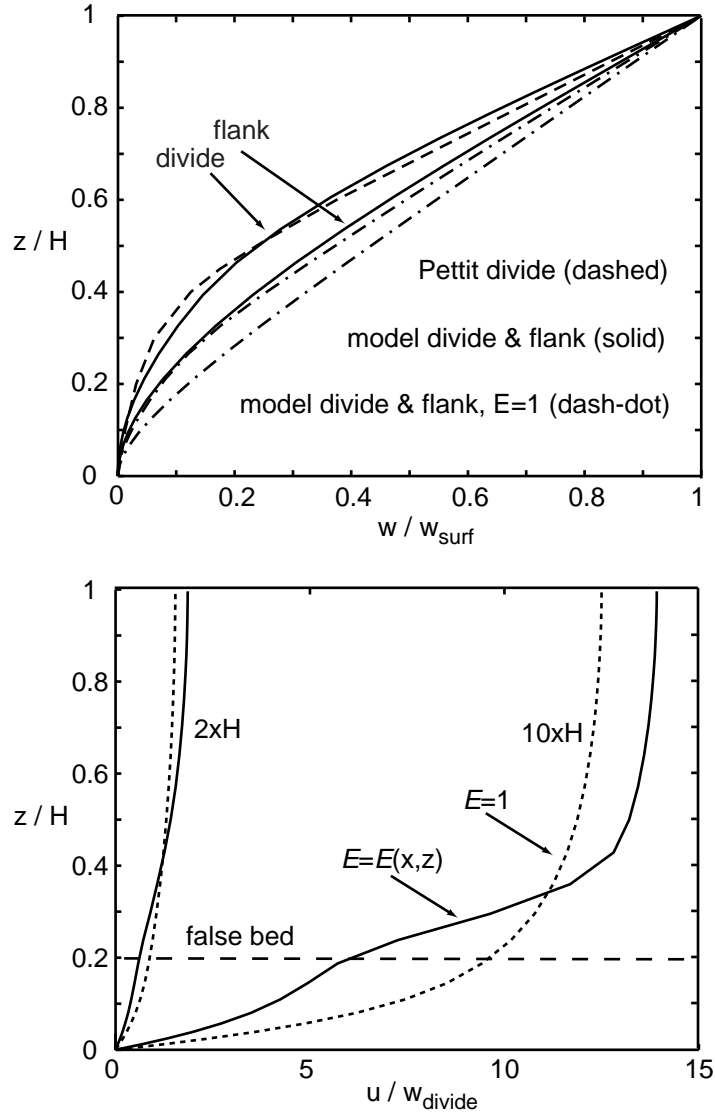


Figure 3.5: Velocity shape functions at Siple Dome divide. (a) Model vertical-velocity shape functions at the divide and flank for the favored values of E shown in Figure 4 (solid) and for the case of $E=1$ (dash-dot). The vertical-velocity shape function at the divide from Pettit (2003) is shown for comparison (dashed). (b) Model horizontal-velocity shape functions at horizontal distances of 1, 2 and 10x the divide-ice thickness. Dashed lines are for the case of $E=1$ and solid lines are for the case where E takes on the favored values.

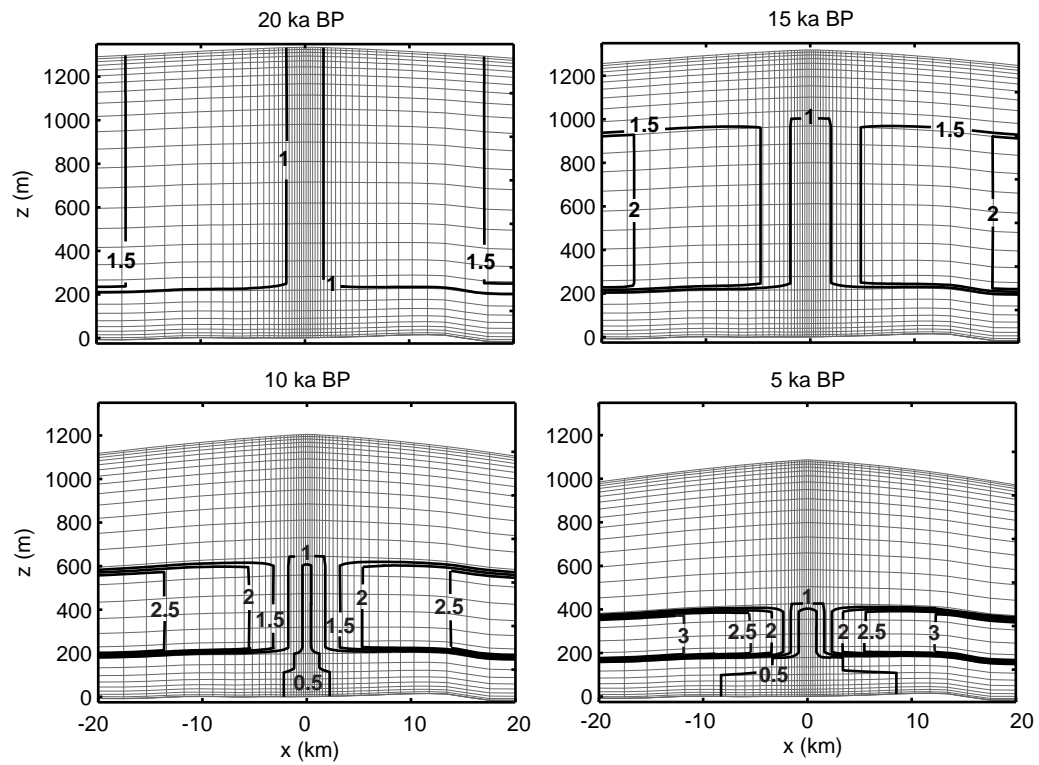


Figure 3.6: Map of flow enhancement at Siple Dome over time. Panels show enhancement factor at points in time subsequent to its initiation and prior to the present (the present-day enhancement field is shown in Figure 4).

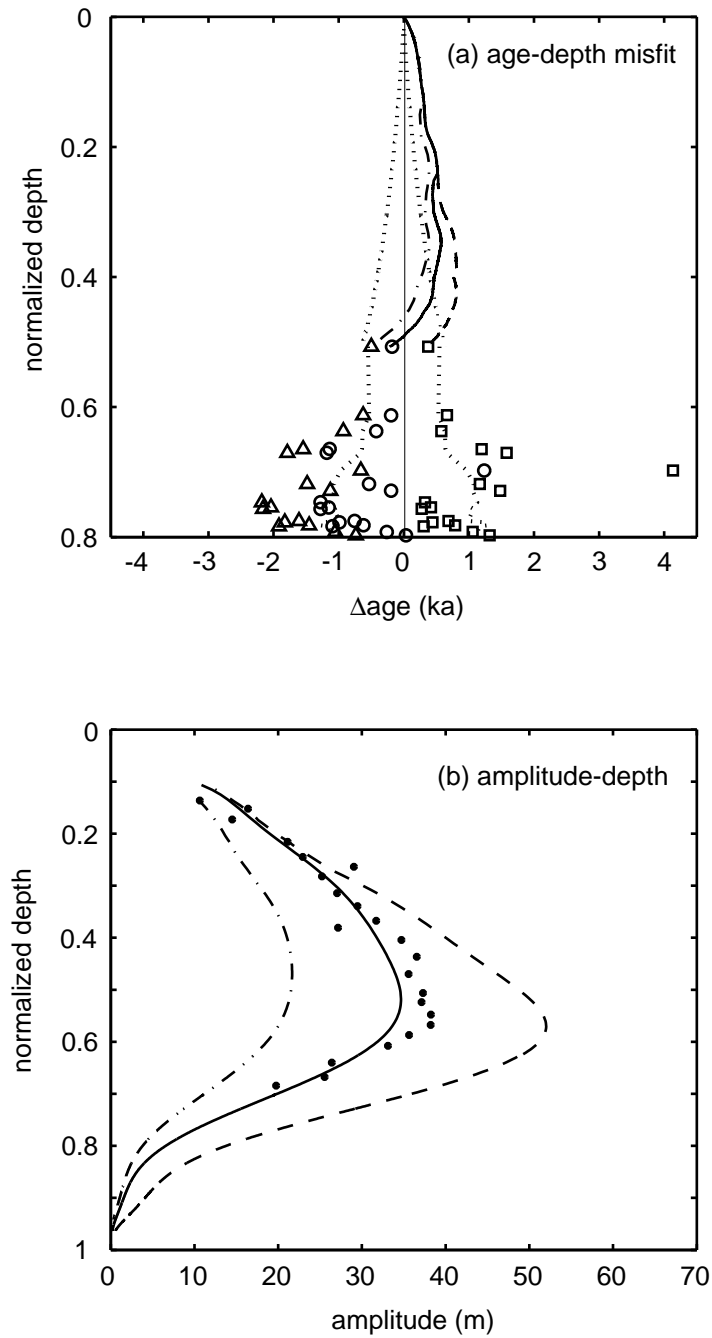


Figure 3.7: Model sensitivity to starting time of divide-flow. (a) Age-depth misfit for divide flow starting at 3 ka (solid line and open circles), 1.5 ka (dash-dot line and triangles), and 6 ka BP (dashed line and squares). (b) As in (a) but for the fit to amplitude-depth profile.

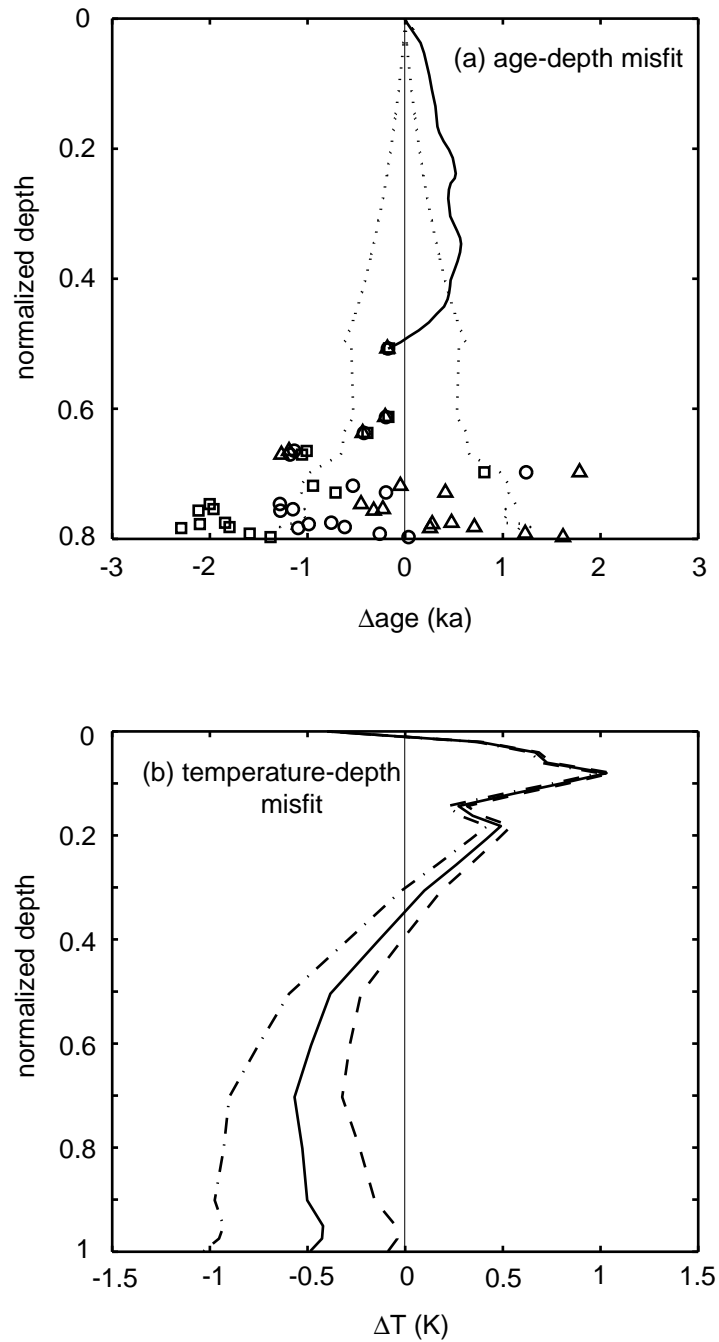


Figure 3.8: Model sensitivity to magnitude of ice-thickness change. (a) Age-depth misfit for thinning of 350 m (solid line and open circles), 250 m (dash-dot line and squares), and 450 m (dashed line and triangles). (b) Temperature-depth misfit for thinning of 350 m (solid), 250 m (dash-dot), and 450 m (dashed).

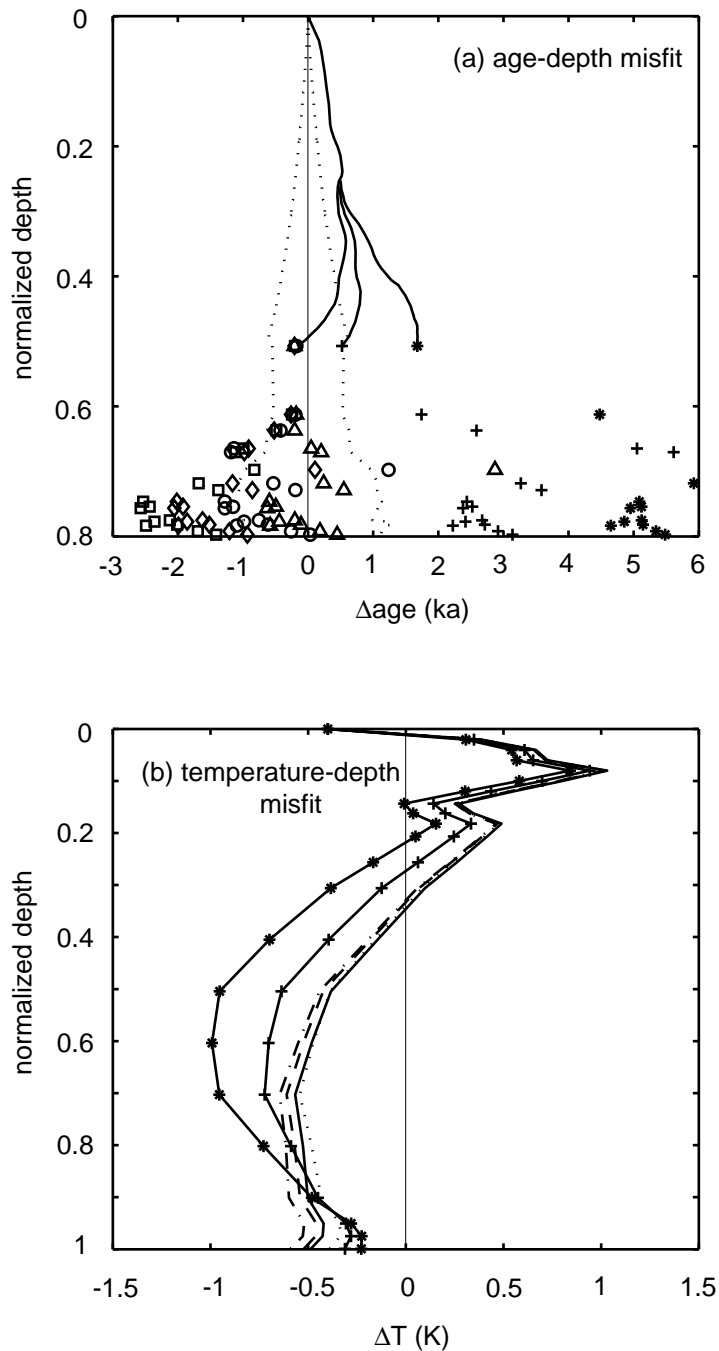


Figure 3.9: Model sensitivity to timing of ice-thickness change. (a) Age-depth misfit for thinning at 20-15 (dash-dot line and squares), 20-12 (dashed line and diamonds), 15-10 (dotted line and triangles), and 15-14 (solid line and circles), 15-2 (solid line and crosses), and 7-2 ka BP (solid line and asterisks). (b) Temperature-depth misfit for thinning at 20-15 (dash-dot line), 20-12 (dashed line), 15-10 (dotted line), and 15-14 (solid line), 15-2 (solid line with crosses), and 7-2 ka BP (solid line with asterisks).

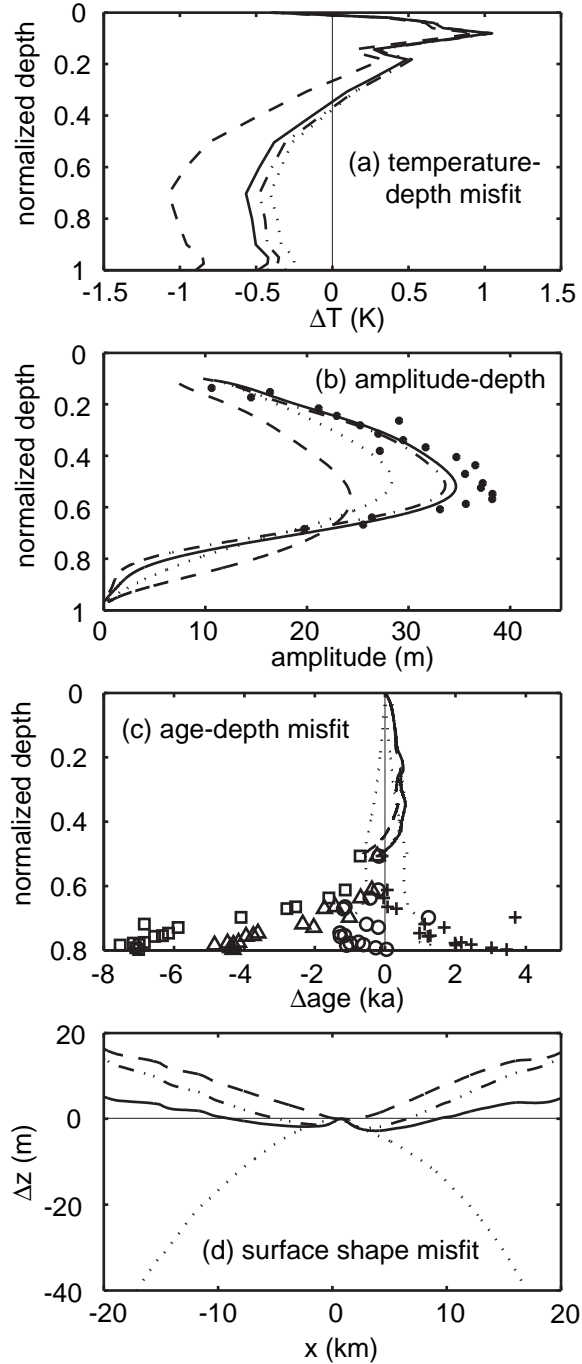


Figure 3.10: Model sensitivity to flow enhancement. (a) Temperature-depth misfit (solid=favored E, dashed E=1, dotted=stiff layer only, dash-dot=c-axis layer simulating "stronger" fabric), (b) As in (a) but for the bump-amplitude profile. (c) Age-depth misfit (circles=favored E, squares E=1, triangles=stiff, basal layer only, crosses=c-axis layer simulating "stronger" fabric) (d) As in (a) but for the surface-shape misfit.

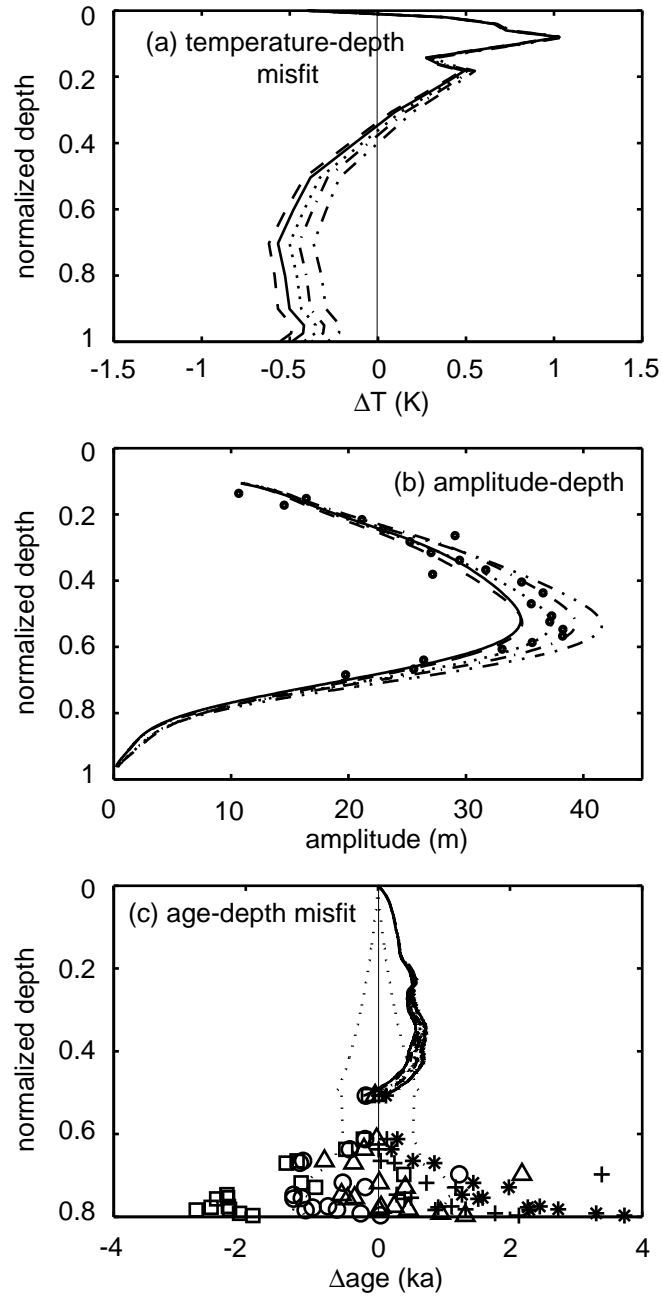


Figure 3.11: Model sensitivity to timing of flow enhancement. (a) Temperature-depth misfit (solid=favored, dashed=start 20 ka BP, dotted=start 40 ka BP, dash-dot=end at 5 ka BP, dot-dot-dash=end at 10 ka BP), (b) As in (a) but for the amplitude-depth profile. (c) Age-depth misfit (circles=favored, squares=start 20 ka BP, triangles=start 40 ka BP, crosses=end at 5 ka BP, asterisks=end at 10 ka BP).

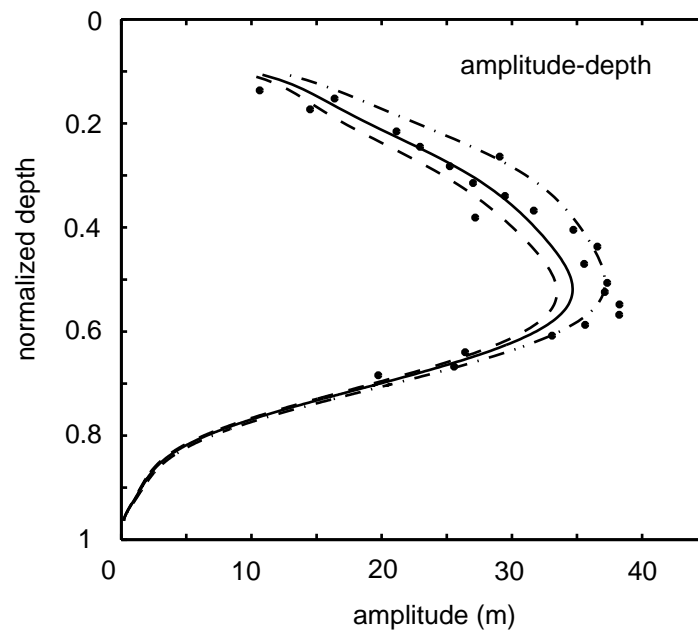


Figure 3.12: Model sensitivity to the rate of divide scouring. The amplitude-depth profile is shown for the case of scouring at a rate of 2x (dash-dot) and 0.5x (dashed) times the favored value of scouring at SDM (solid), which is 25 mm a⁻¹.

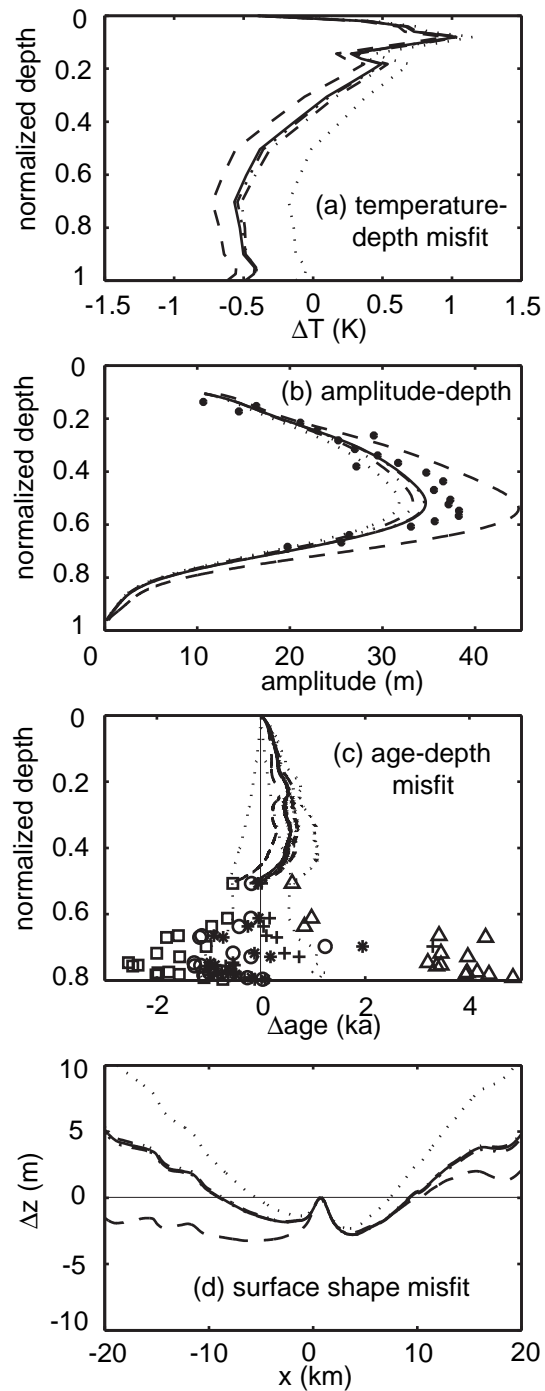


Figure 3.13: Model sensitivity to the accumulation rate history. (a) Temperature-depth misfit (solid=favored, dashed=favored+0.01 m a⁻¹, dotted=favored-0.01 m a⁻¹, dash-dot=first random history, dot-dot-dash=second random history), (b) As in (a) but for the bump-amplitude profile. (c) Age-depth misfit (circles=favored, squares=favored+0.01 m a⁻¹, triangles=favored-0.01 m a⁻¹, crosses=first random history, asterisks=second random history). (d) As in (a) but for the surface-shape misfit.

**UPSTREAM PROPAGATION OF SLIDING TRANSITIONS: FEEDBACKS
BETWEEN SLIDING, LONGITUDINAL-STRESS GRADIENTS, AND
FRICTIONAL MELTING**

Portions of the material in this chapter were originally presented orally at the 12th annual WAIS workshop held in Sterling, VA, on September 28 through October 21, 2005 and at the Fall AGU meeting held in San Francisco, CA, on December 5-9, 2005. This chapter is a draft manuscript with University of Washington co-authors H. Conway and E.D. Waddington and R.A. Bindshadler (NASA Goddard Space Flight Center, Greenbelt, MD).

SUMMARY

A two-dimensional, full-stress, transient ice-flow model is used to investigate the effects of a positive feedback between basal motion, frictional melting, and longitudinal-stress gradients in the overlying ice. A perturbation, initiated by allowing a fraction of the model domain to suddenly slide faster than its upstream counterpart, starts the feedback and allows the sliding transition to widen and migrate upstream over time. The speed and distance of upstream migration are dependent on the magnitude of the initial sliding perturbation and on the degree of nonlinearity assumed in the sliding relation that links basal shear stress to basal motion: a larger perturbation and/or a higher degree of nonlinearity lead to farther and faster upstream migration. Ultimately, upstream migration is controlled by changes in geometry, which limit rapid upstream propagation of the sliding transition through longitudinal-stress gradients. For models that include the feedback, the maximum thinning rate far upstream from the perturbation is larger in magnitude, and occurs earlier, than for models that propagate the perturbation through the mass and stress balance portions of the model alone. These differences

stem from the fact that the initial perturbation is temporarily sustained while it moves upstream when the feedback is accounted for.

INTRODUCTION

Discharge from the Greenland and Antarctic ice sheets is dominated by flow through large-outlet glaciers and ice streams. The impact these outlets have on ice-sheet mass balance is dependent upon many things including their length: a long outlet can draw down the interior regions of an ice sheet more effectively than a short one. With respect to ice-sheet mass balance, and hence changes in global sea level, this concept puts forth several important questions: first, what processes might allow ice streams and outlet glaciers to grow headward over time, and second, what rates, timescales, and ice-volume changes are associated with headward migration?

The fast speed of outlet glaciers and ice streams is due largely to fast motion (henceforth referred to as “sliding”) at, or very near, the ice-bed interface. Sliding, in turn, requires lubrication from basal meltwater, which is produced by geothermal heat and by frictional heat. The rate of frictional heating, which is proportional to the product of sliding speed and basal drag, is largest in regions where sliding and basal drag are intermediate (Raymond, 2000). This region generally coincides with the transition from slow to fast sliding, such as occurs in the ice-stream tributary regions and at the heads of outlet glaciers. A consequence of this transition is that longitudinal-stress gradients contribute significantly to the balance of forces (Price and others, 2002) and, in doing so, modulate basal drag, sliding, and frictional melting. This has important consequences that could allow for positive feedbacks between longitudinal-stress gradients, sliding, and frictional melting as follows: (1) An increase in sliding speed along-flow leads to a longitudinal-stress gradient that is supported by a local increase in basal drag upstream from the sliding transition. (2) The local increase in basal drag leads to a

local increase in frictional melting and potentially, (3) an increase in sliding and longitudinal-stress gradients upstream from the transition region (4) and an increase in drag and melting still farther upstream, allowing the sliding transition to propagate upstream over time. This upstream propagation of a slow-to-fast sliding transition is synonymous with inland migration of the head of an ice stream or outlet glacier.

Below, we incorporate a simple form of this feedback into a flow model with appropriate physics. Our goal is to take first steps towards quantifying the impact of this feedback on the evolution of an ice-sheet drainage for which (1) sliding is a significant fraction of the overall ice motion and (2) perturbations in sliding could initiate the feedback described above.

FLOW MODEL

Model Description

Our flowline model, based on the Finite Volume Method (FVM) (Patankar, 1980; Versteeg and Malalasekera, 1995), solves the full two-dimensional (2D) momentum equations. It is described fully in Price and others (in prep.). Here, we discuss relevant portions of the model including the governing equations, the general solution method, and the parameterizations that link stresses in the ice with frictional melting and sliding at the glacier base.

For viscous, low Reynolds-number flow, conservation of momentum in a 2D, Cartesian reference frame is expressed as

$$\rho g_i + \frac{\partial \sigma_{ij}}{\partial x_j} = 0, \quad (i, j = x, z), \quad (4.1)$$

where x and z are the along-flow and vertical-coordinate directions, and repeat indices imply summation. The first term on the left-hand side of Equation (4.1) is

the body force, the product of ice density, ρ , and the acceleration due to gravity in direction i , g_i . The second term is the stress divergence where the full stress tensor is given by

$$\sigma_{ij} = \tau_{ij} - P\delta_{ij}, \quad (4.2)$$

the deviatoric stress, τ_{ij} , minus the pressure, P . The constitutive relation linking deviatoric-stress and strain rate is given by

$$\tau_{ij} = 2\eta\dot{\varepsilon}_{ij}, \quad (4.3)$$

where ε_{ij} is the strain-rate tensor,

$$\dot{\varepsilon}_{ij} = \frac{1}{2} \left(\frac{\partial u_i}{\partial x_j} + \frac{\partial u_j}{\partial x_i} \right), \quad (4.4)$$

and η is the effective viscosity,

$$\eta = \frac{1}{2} B(T) \dot{\varepsilon}_e^{\frac{1-n}{n}}. \quad (4.5)$$

In Equation (4.4), u_i represents the components of the velocity vector, u or w , parallel to the x and z directions, respectively. In Equation (4.5), $B(T)$ is the temperature-dependent rate factor, n is the power-law exponent (taken equal to 3), and $\dot{\varepsilon}_e$ is the effective-strain rate, given by

$$2\dot{\varepsilon}_e^2 = \dot{\varepsilon}_{ij}\dot{\varepsilon}_{ij}. \quad (4.6)$$

The ice is assumed to be incompressible:

$$\frac{\partial u}{\partial x} + \frac{\partial w}{\partial z} = 0. \quad (4.7)$$

We solve Equation (4.1) in a boundary-fitted, orthogonal, curvilinear-coordinate system. The transformation between this system and a standard 2D Cartesian coordinate system is discussed in detail in Price and others (in prep.). The model solutions that we discuss below (e.g. stress fields) have been transformed back to a Cartesian coordinate system.

General Solution Method

Integrating Equation (4.7) over a single finite volume (i.e. a single grid cell) gives

$$\rho(u_D A_D - u_U A_U) + \rho(w_T A_T - w_B A_B) = 0, \quad (4.8)$$

where ρ is density; the subscripts U , D , T , and B refer, respectively, to the upstream, downstream, top, and bottom faces of a single cell; and A is the area of the relevant cell face: for example, $A_U = W_U \Delta z_U$, where W_U and Δz_U are the flowband width, here taken as unity, and height, respectively, at the upstream cell face. Equation (4.8) states that the net mass flux into and out of a volume sums to zero. Using Equations (4.2) through (4.6) in Equation (4.1) with an estimated pressure field we solve for estimated velocity fields u^* and w^* . Inserting these values into Equation (4.8) we obtain

$$\rho(u_D^* A_D - u_U^* A_U) + \rho(w_T^* A_T - w_B^* A_B) = S, \quad (4.9)$$

where S is non-zero because, in general, our initial estimate for the velocity field will not satisfy continuity. To satisfy continuity, the mass source (or sink) within each volume, S , is eliminated through an iterative pressure-correction method (Patankar, 1980). Briefly, a non-zero mass source specifies a pressure perturbation that improves upon the estimated pressure and velocity fields. Through Equation

(4.9), the updated velocity field leads to a further improvement in the estimate for the mass source (i.e. one with a smaller magnitude) and a further improvement to the estimated pressure perturbation. Simultaneously, the updated velocity field is used to update the estimated effective viscosity through Equations (4.4) and (4.5). Iterations continue until the solution has converged.

The converged velocity field is used to predict the change in the shape of the free surface (and thus the change in the domain geometry) at a future time step. Changes in domain geometry and the redistribution of mass within the (x,z) plane are accounted for when re-gridding the finite-volume mesh at the start of each time step.

Basal Motion

The frictional-melting rate, proportional to the product of sliding speed and basal drag, is given by

$$\dot{m} = \frac{u_b \tau_b}{\rho L_f}. \quad (4.10)$$

Here, the sliding speed, u_b , is defined as the horizontal velocity at the top of a basal layer of deforming, viscous fluid (e.g. till) for which the rate of shear deformation is given by

$$\dot{\epsilon}_{zx} = C \tau_{zx}^p. \quad (4.11)$$

C and p are the rate factor and the power-law exponent, analogous to A and n in the flow law for ice. For $p=1$, the basal layer has a Newtonian viscous rheology. For $p>1$, the fluid has a power-law viscous behavior. The inverse-flow law for the basal layer is given by

$$\tau_{zx} = D \dot{\epsilon}_{zx}^{1/p}, \quad (4.12)$$

where $D = C^{-1/p}$ is an inverse-rate factor (or “stiffness parameter”) with units of $\text{Pa a}^{1/p}$. For $p \gg 1$ in Equation 4.12, the magnitude of D essentially serves to define the yield strength of the basal layer (see Figure 4.1). Here, we investigate model behavior for $p=1$ and $p=3$. The case of $p=1$ gives an estimate for the model response when the sliding relation is least sensitive to perturbations in the stiffness parameter. The case of $p=3$ is chosen as representative of a non-linear sliding relation because it is intermediate between $p=1$ and $p \gg 1$: if the basal layer is very weak ($p \gg 1$) the resistance to basal motion comes from ice deformation around basal roughness elements and/or sticky spots that would tend to enforce $p=n$ (Raymond, 2000), where n was introduced in Equation 4.5.

We assume that $D = D(\dot{m})$: as the melting rate increases, the shear stress required to produce a given shear-strain rate in the basal layer decreases. This simplification is attractive because it allows us to avoid complications associated with the transport and storage of basal water, and there is support for its use with respect to the mechanics of subglacial till beneath the West Antarctic ice streams (e.g. Tulaczyk and others, 2000). Alternatively, such a relation would be appropriate in a region approaching, but not yet at, the “drainage limited” lubrication steady state of Raymond (2000; Figure 4b). This simply requires that, as basal-water production increases, further increases in water production (through frictional heating) exceed increases in drainage. An alternative model that is more generally applicable is one in which the strength of the basal layer at any time is a function of the total amount of water present at the bed. Such a model can include terms for the import, storage, and drainage of basal water in addition to its production. Below, we further discuss the implications of our assumption that $D = D(\dot{m})$ and the implications of how other assumptions might affect the results presented here.

When we refer to the bed “strength”, a reasonable physical interpretation is the yield stress, given by the stiffness parameter, D , in Equation (4.12) for the case of $p \gg 1$. The change in the stiffness parameter, ΔD , is assumed to start at some threshold melting rate \dot{m}_0 , takes place over a specified range of melting rate $\Delta \dot{m}$,

and ends at $\dot{m}_1 = \dot{m}_0 + \Delta\dot{m}$. For $\dot{m} < \dot{m}_0$ the stiffness parameter takes on one value and for $\dot{m} > \dot{m}_1$ it takes on a smaller value. For increasing melt rate in the range $\dot{m}_0 < \dot{m} < \dot{m}_1$, the stiffness parameter decreases smoothly from D to $D+\Delta D$ according to the shape of one half of a cosine bell curve (Figure 4.2). Below, when we refer to the “sliding transition” we are referring to the region over which the change in the stiffness parameter takes place.

Boundary Conditions, Initial Conditions, and Assumptions

The initial calculation domain is ~ 650 km long and varies in thickness from ~ 2000 m at its upstream end to ~ 400 m at its downstream end. Length scales were chosen to approximate those of large-scale ice-sheet drainage (for example, a West Antarctic ice stream). The upstream boundary of the calculation domain is a flow divide at which we specify a zero-flux boundary condition. The surface is specified as stress free, and a no-slip condition is specified at the base of the basal layer discussed above. We specify hydrostatic pressure at the downstream boundary in order to *not* have to specify the velocity, and hence the flux, there. Because the portion of the model domain on which we focus our attention here is far upstream from the downstream boundary (~ 350 km or $>200\times$ the mean ice thickness) the velocity field at the downstream boundary does not significantly affect our results.

All models start from an approximately steady state in which the accumulation rate, the stiffness parameter, and p are held steady and constant, and the rate of elevation change everywhere within the domain is $\leq 10^{-4}$ m a $^{-1}$. Because we wish to clearly isolate how evolution of frictional melting affects evolution of the basal-layer strength, we specify isothermal ice. In this case, there is no temperature-field calculation, and we assume that some minor, base melting exists and allows sliding to occur everywhere. The frictional melting rate above this base-melting rate defines time evolution of the basal-layer strength through evolution of the stiffness parameter, $D = D(\dot{m})$. Henceforth, when we discuss “melting rate” we specifically mean the melting rate resulting from frictional heating alone.

We do not include a parameterization to account for the effects of drag against valley sidewalls (in the case of an outlet glacier) or against slower-moving ice (in the case of an ice stream). Here, we mainly consider flow along the inland regions of an ice sheet where, although not negligible, these effects should to the overall stress balance in a minor way. In the discussion section below we consider how this omission would affect the results presented here.

Perturbing the Equilibrium Models

Below, we discuss the model response to a perturbation for two sets of tests. In one set, the feedback between stresses in the ice, frictional melting at the bed, and the strength of the basal layer is turned “off”; after an initial perturbation to the stiffness parameter, its spatial description remains fixed over time. In another set of tests, the feedback is turned “on” and the stiffness parameter evolves over time in response to the evolution of the melting rate, as described above.

The perturbation that we introduce is an instantaneous reduction in the stiffness parameter, and thus an instantaneous jump in sliding speed, over the downstream half of the model domain. First, we arbitrarily choose a point along flow and define the melting rate at that point as the threshold melting rate (\dot{m}_0 in Figure 4.2). For a given value of $\Delta\dot{m}$, this allows us to define \dot{m}_1 , and thus where on the melting-rate profile the non-zero gradient in the stiffness parameter begins and ends. Starting with the melting-rate profile from the steady-state, initial condition, we specify that everywhere $\dot{m} \leq \dot{m}_0$, the value of the stiffness parameter remains unchanged ($D_{\text{new}}=D_{\text{ini}}$), and everywhere $\dot{m} \geq \dot{m}_1$ the value of the stiffness parameter is reduced by some fraction of its initial value ($D_{\text{new}}=D_{\text{ini}}+\Delta D$). In between, the stiffness parameter decreases smoothly as a function of \dot{m} , as shown in Figure 4.2. Below, when we report a value for ΔD (the reduction in the stiffness parameter), we report it as the percent reduction from its initial value, D_{ini} , which is by definition $20 \text{ kPa a}^{1/p}$; $\Delta D=(-0.1)D_{\text{ini}}$ will be reported as a “ ΔD of 10%”.

When the feedback is turned off, we hold the new distribution for the stiffness parameter fixed as the model evolves. These models serve as a reference

against which we compare results from models with the feedback turned on. The reference models are analogous to models explored by Payne and others (2004) in which the geometry and stress fields evolve in response to a perturbation but the distribution of basal resistance does not. Here, when the feedback is turned on, \dot{m} and the stiffness parameter evolve over time in response to the changing geometry and stress field and, in turn, affect the geometry and stress field. We refer to models in which the feedback is turned on as “linked” models. In those models we assume that the pattern of \dot{m} and the stiffness parameter are in equilibrium with the stress field at each time step. Thus, during any time step, we iterate on the value of \dot{m} and the value of the stiffness parameter while holding the geometry constant, until we obtain a consistent solution. Iterations continue until the velocity field no longer changes. Computationally, this is not an additional hindrance, as convergence usually occurs in a few iterations.

RESULTS

We first use a single reference model to provide a generic description for the system evolution after a perturbation is applied. This is convenient because the dominant physical processes are common to both the reference and linked models, but the former avoids the additional complication of a sliding transition that is moving in time. As we discuss below, the feedback affects the magnitude and timescale of the model response but does not significantly change the nature of the response itself. For the reference model discussed below, $p=3$ and the applied perturbation is a ΔD of 10%. In Figures 4.3 and 4.4 we show the evolution of the stress fields and geometry, and in Figure 4.5 we show the evolution of the melting rate. In Figures 4.3-4.5, we focus on the region within several tens of ice thicknesses of the place where the perturbation is initiated.

Figures 4.6 and 4.7 show evolution of the stress and geometry for a similar linked model. Figure 4.5 also shows evolution of the melting rate for that same

model. In Figure 4.8, we show the evolution of the melting rate for several reference and linked models that assume a range of values for ΔD and p . In Figures 4.10-4.12 we examine the far-field effects of perturbations by showing thinning rates as a function of time and distance from the perturbation. This, in turn, provides a larger context for understanding the evolution of melting rates and the transition region over time.

DISCUSSION

Evolution of Geometry and Stress Fields: Reference Model

In Figures 4.3 and 4.4, we show the modeled longitudinal-stress gradients and terms in the depth-averaged stress balance for various times after the perturbation is applied. When the perturbation is applied, longitudinal-stress gradients are positive throughout the entire ice column on the upstream side of the sliding transition and negative throughout the entire ice column on the downstream side ($t=0$ a, Figure 4.3). In response, basal drag is elevated upstream from the transition and depressed downstream from the transition relative to the driving stress. The driving stress shows no immediate response because the surface geometry has had no time to adjust to the new stress state ($t=0$ a, Figure 4.4). For the case shown in Figures 4.3 and 4.4, the longitudinal-stress gradient “impulse” affects the basal drag over a region $\sim 20\times$ the ice thickness on either side of the transition. The melting-rate profile is everywhere increased relative to the initial condition because, on the downstream side of the transition, the sliding speed has increased and, on the upstream side of the transition, both the sliding speed and the basal drag have increased.

From 3 to 5 a after the perturbation has been applied, the longitudinal-stress gradient impulse diffuses; its effects propagate up and downstream and its magnitude decreases ($t=3-5$ a, Figures 4.3 and 4.4). The surface geometry starts to adjust to the new stress field by getting steeper on the upstream side of the

transition, in response to relatively higher basal drag there, and flatter on the downstream side, in response to the relatively lower basal drag there. As a result, the driving-stress profile evolves to more closely match that of the basal drag. The melting rate reflects these changes as well; relative to the melting-rate profile immediately after the perturbation is applied, it continues to increase on the upstream side of the transition but decreases on the downstream side.

Between 10 and 20 a after the perturbation, the surface geometry, through the evolving stress field, begins to come back into equilibrium with the new pattern of basal resistance. The pattern of longitudinal-stress gradients evolves to one that is very different from the initial one ($t=10-20$ a, Figures 4.3 and 4.4). On the downstream side of the transition, the reduction in the basal stiffness parameter results in faster sliding. As a result, less internal deformation of the ice column is needed to pass the steady-state flux; the lower portion of the ice column speeds up across the transition but the upper portion slows down. The result is that, across the transition, the pattern of longitudinal-stress gradients along the surface is similar to that at the bed but rotated by 180 degrees. The reduction in velocity in the upper ice column is of a smaller magnitude than the increase in velocity near the bed. Nevertheless, because it occurs over a large fraction of the ice column, and a fraction of the ice column that is relatively stiff (owing to its smaller effective viscosity), the pattern of longitudinal-stress gradients along the surface more closely resembles its depth-averaged value than does the pattern along the bed. The effect of longitudinal-stress gradients is small except within ~ 5 ice thicknesses on either side of the sliding transition where positive gradients raise the basal drag slightly. Previous authors have made similar observations with respect to equilibrium patterns of longitudinal-stress gradients: Weertman (1957) noted the 180-degree rotation pattern at a jump in basal sliding and Budd (1970) discussed the “smoothing” effect of longitudinal-stress gradients on the basal-drag profile with respect to the driving stress profile.

After 500 a, large-scale adjustments to the velocity fields and surface shape are essentially complete. While there is a decrease in the driving stress and basal

drag across the transition, the gradient in both terms on either side of the transition is essentially the same as prior to the perturbation. The reduction in driving stress and basal drag across the transition reflects the necessary adjustment of the geometry to achieve a new steady-state. Upstream, steeper surface slopes are required to pass the steady-state ice flux through a relatively thinner ice column for which the basal velocity has not changed. Downstream, shallower slopes are required to pass the steady-state ice flux because the basal velocities have increased (owing to the reduction in the basal stiffness parameter). After 500 a, the ice sheet continues to thin at a decreasing rate for several thousand years.

Evolution of Melting Rate: Reference Model

To illustrate how the melting rate upstream from the transition evolves after the perturbation, we track the location of \dot{m}_0 over time. We choose \dot{m}_0 as the important melt rate to track because, for the linked model, it also defines the upstream boundary for the sliding transition. For the reference model, its location provides a preliminary estimate for how the sliding transition will change position when the melt-rate feedback is included in the model. While the model response will differ for the linked case, the dominant physical processes controlling evolution of the melting rates will be the same as for the reference case.

The dashed line in Figure 4.5 shows the location of \dot{m}_0 in the reference model as a function of time after the perturbation. It is convenient to divide the trajectory of \dot{m}_0 into three time periods for which the change in the position of \dot{m}_0 is controlled by three different processes: (1) an initial, short-lived (order tens of years or less) but rapid period of upstream motion, (2) a longer period (several hundred years) of more gradual upstream migration, and (3) a long period (several thousand years) where the position of \dot{m}_0 stabilizes at its most upstream extent and then drifts slowly back downstream. The initial period of rapid upstream motion results from the initial response to the change in sliding speed at the site of the perturbation (interval [1], Figure 4.5 inset): tension across the transition increases the basal friction, sliding speed, and hence the melting rate upstream from the

transition. This initial, rapid, upstream propagation of \dot{m}_0 is short-lived because, as the causative longitudinal-stress gradient decreases in magnitude, its effectiveness at raising the melting-rate to \dot{m}_0 decreases. The linked case, which we discuss below, provides support for this interpretation. The second period of slower but sustained upstream migration reflects the melting rate changing in response to the changing ice-sheet geometry. As thinning propagates upstream from the site of the initial perturbation, the surface slope steepens and the driving stress, basal drag, sliding speed, and melting rate continue to increase slowly (interval [2], Figure 4.5 inset). When this period of thinning begins to subside, driving stress, basal drag, and sliding speed start to decrease from their transient, high values as surface slopes flatten and net thinning of the ice column becomes substantial. In this third period, \dot{m}_0 stabilizes its position temporarily before beginning a slow migration back downstream (interval [3], Figure 4.5). The slow downstream drift is associated with continued, slow thinning of the ice column for several thousand years after the perturbation. After 5 ka, the thinning rate has decreased to very small values and the position of \dot{m}_0 drifts slowly towards a new steady-state location. This location is farther upstream because of the change in geometry accompanying the new steady state: upstream from the transition, surface slope (and thus driving stress, basal drag, and frictional melting) has increased in order to accommodate the steady-state flux through a relatively thinner column of ice (recall that the accumulation rate is held constant).

To summarize, the initial, brief period during which \dot{m}_0 propagates rapidly upstream is associated with an initial, large but transient longitudinal-stress gradient. The latter two periods reflect the adjustment of the ice sheet in response to thinning from the initial perturbation. We provide further support for this interpretation below.

Evolution of Geometry and Stress Fields: Linked Model

Figures 4.6 and 4.7 are analogous to Figures 4.3 and 4.4 but show the evolution of the model stress fields for the linked case. The notable difference with respect to

the reference case is that, rather than remaining fixed, the sliding transition is free to change its location as the melting rate evolves and, in turn, as the stiffness parameter evolves.

The instantaneous response is identical to that shown in Figures 4.3 and 4.4. At 3 a after the perturbation, however, the response of the linked model differs significantly from the reference model. Because the location of the reduction in the stiffness parameter now migrates upstream with m_0 , the longitudinal-stress gradient impulse has jumped upstream a distance of $\sim 15\times$ the ice thickness ($t=3$ a, Figures 4.6 and 4.7). The driving stress (and hence, the surface geometry) has started to adjust to the initial perturbation but lags behind the change in the pattern of basal drag, which has already moved farther upstream along with the causative longitudinal-stress gradient ($t=3$ a, Figure 4.7). At 3 a, the magnitude of the longitudinal-stress gradient is *larger* than at the time of the initial perturbation ($t=3$ a, Figure 4.7). This occurs because the initial perturbation steepens the melt-rate profile, which narrows the width of the transition zone and focuses the stress gradient associated with ΔD over a shorter distance.

At 5 a, the upstream edge of the sliding transition has migrated upstream by approximately $20\times$ the ice thickness. Only now does the longitudinal-stress gradient start to decrease in magnitude and diffuse ($t=5$ a, Figures 4.6 and 4.7). Although upstream migration of the transition zone allows for a sustained perturbation, the longitudinal-stress gradient eventually decreases in magnitude because the ice upstream has already begun to respond by adjusting its geometry (note that the driving-stress profile at 5 a in Figure 4.7 is “catching up with” the basal-drag profile) and its velocity. By 10-20 a, the longitudinal-stress gradient in the transition region has decreased significantly and the geometry has adjusted so that the driving stress and basal drag are nearly equal across the transition region. Associated with this is the same change in the pattern of longitudinal-stress gradients discussed above for the reference case.

By 500 years, large-scale changes are complete and, as in the reference case, the ice sheet continues to slowly adjust to long-term thinning. Relative to the

reference case, significant differences are: (1) the sliding transition is approximately 20 ice thicknesses upstream from its initial location, (2) the sliding transition is wider and, (3) the associated longitudinal-stress gradient has smaller magnitude. All of these differences result from the co-evolution of stresses at the ice-bed interface, the melt-rate profile and the basal-stiffness parameter.

Evolution of Melting Rate: Linked Model

Evolution of the melting rate for the linked model follows that for the reference model (solid line, Figure 4.5). In the linked model, the location of \dot{m}_0 has particular importance with respect to flow dynamics; it is synonymous with the location of the upstream boundary to the sliding transition. This results in an important difference between the two models. There is a longer period during which \dot{m}_0 jumps rapidly upstream through longitudinal-stress gradients because the initial perturbation is sustained for several years as the sliding transition (the region over which the stiffness parameter decreases) moves upstream. The net affect is that \dot{m}_0 propagates farther upstream in the linked case before it begins drifting back downstream. Figure 4.7 confirms that the initial, rapid upstream jump of \dot{m}_0 is due to longitudinal-stress gradients rather than effects associated with changes in the ice sheet geometry: for at least the first 5 a after the perturbation, the change in driving stress lags behind the change in basal drag, which is controlled largely by longitudinal-stress gradients.

Evolution of Melting Rate: All Models

Figure 4.8, analogous to Figure 4.5, shows the position of \dot{m}_0 over time for models in which we vary the value of ΔD from 5% to 15% and the value of p from 1 to 3. It provides additional insight into processes that favor upstream migration of \dot{m}_0 during the three different periods discussed above.

During the initial period of upstream propagation associated with the transient longitudinal-stress gradient, \dot{m}_0 will travel farther upstream under two circumstances: (1) as a result of a larger perturbation, and (2) as a result of a more

uniform, or smaller gradient in the melt-rate profile. The first circumstance is intuitive and clearly demonstrated by Figure 4.8. A larger perturbation leads to a larger initial longitudinal-stress gradient, which affects the basal friction and sliding speed, and hence the melting rate, over a larger distance. In turn, a larger perturbation results from a larger jump in sliding speed across the transition, given by a larger ΔD or, for the same ΔD , by a larger value of p (for $p > 1$ the change in strain rate per change in stress is non-linear (Figure 4.1)). For the second circumstance, consider that (here) the melting rate is a function that increases monotonically with distance from the flow divide. The gradient of this function dictates how far upstream a longitudinal-stress gradient of given value will affect the melting-rate profile: the larger the gradient, the shorter the distance a given longitudinal-stress gradient will be effective at raising the melting rate to \dot{m}_0 , and vice versa. Figure 4.9 illustrates this concept schematically. For initial melt-rate profile (a) or (b) (solid lines), a given perturbation to the melting rate, $\Delta \dot{m}$, at x_0 results in a new melt-rate profile (dashed lines). The melting rate initially at x_0 is farther upstream along the new profile (b) than it is for the new profile (a) because the initial profile gradient for (a) is larger. Thus, conditions that favor a constant melt-rate profile or a melt-rate profile with a small gradient will favor the upstream propagation of perturbations to the melting rate through longitudinal-stress gradients. Because velocities generally increase along flow due to mass balance considerations, the important condition with respect to Equation (4.10) is then a uniform, or decreasing, basal drag along flow. Here, that condition will occur for larger values of p . A limiting aspect of a melt-rate profile with a small gradient is that a given ΔD occurs over a larger spatial distance (Figure 4.2). In that case, the associated longitudinal-stress gradient has a smaller magnitude than for a melt-rate profile with a larger gradient.

The second period of upstream migration, in which \dot{m}_0 responds to increasing surface slopes, is largely controlled by the magnitude of the initial perturbation. A larger perturbation is associated with a larger magnitude of thinning, which has a larger affect on the transient surface slope, driving stress,

basal drag, sliding speed, and melting rate. Because the associated rate of thinning is larger for a larger perturbation, significant thinning of the ice column takes place relatively sooner and the amount of time m_0 spends at its maximum upstream position is relatively shorter: as ΔD and p increase in Figure 4.8, the maximum of the curve of the m_0 versus time becomes increasingly narrow and skewed towards time zero. This and other features of the curves in Figure 4.8 are more easily understood when we consider that the large-scale model response to the perturbation is thinning over time, which we discuss next.

Large-Scale Model Response

After the perturbation, the large-scale response of the model is thinning; the decrease in the stiffness parameter over a portion of the domain increases the sliding speed and removes mass faster than it is replaced through accumulation. Thinning continues for several thousand years as the geometry and stress fields adjust to the new basal conditions. Thinning is then an important control on the long-term trends of melting rates and on the position of the sliding transition. In Figure 4.10, we show the thinning rate over time at a distance of 150 ice thicknesses upstream from the initial perturbation for the same cases shown in Figure 4.8. Qualitatively, the shapes of the curves of thinning rate versus time closely resemble those tracking the position of m_0 over time. This confirms that thinning is important for controlling the position of m_0 , and thus the location of the sliding transition. As ΔD and/or p increases, the curves in both Figures 4.8 and 4.10 increase in amplitude and are more narrowly peaked and skewed towards time zero. It follows that it is important to identify which, if any, of the large-scale model response is due to the feedback discussed above and not simply to overall patterns of thickness change that are common to both the reference and linked models. Put another way, does the linked model lead to any important differences in model evolution other than allowing the location of the sliding transition to migrate upstream over time?

Figures 4.8 and 4.10 also show systematic differences between the reference and linked models: as the value of ΔD and/or p increases, the difference in the curves for the reference and linked models also increases. In Figure 4.8, the maximum upstream extent of \dot{m}_0 is greater for the linked model than for the reference model and this difference increases as ΔD and/or p increases. Figure 4.10 shows similar trends but with respect to thinning rates far upstream from the perturbation. These differences are summarized in Figure 4.11, which shows the percent increase in the maximum thinning rate for the linked versus the reference model. Also shown in Figure 4.11 is the percent decrease in the arrival time of the maximum rate of thinning (plotted as a positive number). The maximum rate of thinning is larger, and occurs sooner, for the linked models than for the reference models. For $p=1$, the largest increase from the reference models to the linked models is $\sim 6\%$, and for $p=3$, the largest increase is $\sim 20\%$. For larger perturbations and higher degrees of non-linearity in the basal sliding relation, larger increases are expected.

The cause for the differences is straightforward. In the linked model, the magnitude of the initial perturbation does not immediately begin to decay but sustains itself for several decades through longitudinal-stress gradients as it propagates upstream. Because the perturbation does not immediately start to decrease in magnitude, the maximum rate of thinning and the net thinning are larger. Because the location of the perturbation itself moves rapidly upstream for a period of time, thinning at some fixed distance upstream starts sooner than if the perturbation were fixed. Figure 4.12 demonstrates both of these concepts by comparing the thinning rate some distance upstream from the perturbation for the reference and linked models discussed in Figure 4.3, 4.4, 4.6 and 4.7 above.

Synthesis

The model demonstrates that a feedback between basal sliding, frictional melting, and stresses in the ice allows the position of a sliding transition to change over time. For the perturbation examined here, the transition initially moves upstream by

as much as 35 ice thicknesses. After several hundred to several thousand years, it begins to migrate back downstream again. After 5 ka, the transition may still be up to 10 ice thicknesses upstream from its initial location. To first order, the position of the transition over time follows the evolution of melting rates over time, even when the feedback itself is omitted from the model.

To initiate the feedback, we start with a perturbation that has a much larger impact on the long-term evolution of the model than the feedback itself. However, as the size of the initial perturbation and/or the value of the stress exponent, p , increases, so does the importance of the feedback. In the most extreme case tested here, longitudinal-stress gradients allow the sliding transition to propagate ~ 25 ice thicknesses upstream in 10 years or less. During this time, the feedback allows the magnitude of the original perturbation to be sustained, or even to temporarily grow in some cases, and to propagate upstream. For cases where there is no feedback, the initial perturbation immediately starts to decay.

The experiments conducted here failed to produce a continued upstream migration of the sliding transition. Rapid, continued upstream migration initially occurs as a result of a large, transient longitudinal-stress gradient, which results in a stress field that is far from steady state with respect to the geometry and surface-mass balance. This large, transient longitudinal-stress gradient decreases rapidly. After a few decades, further upstream migration of the sliding transition is associated with a very different process, that of the slowly changing ice sheet geometry. Driving stress, basal drag, and frictional melting increase slowly for several hundred years as surface slopes increase in response to an upstream propagating wave of thinning. Ultimately, this process thins the ice column to the point that driving stress, basal drag, and frictional melting decrease, causing the transition to migrate slowly back downstream over several thousand years.

The key factor in limiting continued upstream propagation of the sliding transition is the diffusion of the large, transient longitudinal-stress gradient associated with the initial perturbation. Any time after the initial perturbation, the pattern of longitudinal-stress gradients across the transition decreases as the local

geometry begins to adjust. To maintain a large, transient longitudinal-stress gradient across the transition, the transition region itself must move far enough upstream, and quickly enough to outpace topographic diffusion.

On ice sheets, and particularly on ice streams, topographic diffusion is fast due to large thicknesses and small slopes. This provides one potential limit on any continued upstream migration through longitudinal-stress gradients. In addition, upstream propagation of the sliding transition is tied to the melt-rate profile. Any reduction in the ability of longitudinal-stress gradients to raise the melt-rate profile above the threshold value will lead to a reduction in the rate at which the sliding transition propagates. Here, sliding speed and basal drag, and thus frictional melting, decrease moving farther upstream. Thus, a given longitudinal-stress gradient will become increasingly less effective at raising the melting rate above its “background” level and, eventually, upstream propagation of the sliding transition will slow down. The gradient of the melt-rate profile is then important for determining how far upstream the sliding transition can propagate via longitudinal-stress gradients: it will travel farther upstream when the melt-rate profile has a small gradient. Because flow speeds generally increase downstream, uniform or decreasing basal drag along flow is the one condition that favors a melt-rate profile with a small gradient. Regions on an ice sheet where the basal drag is uniform (and small) over many hundreds of km include ice streams and ice plains. These regions are then likely to be effective at transmitting perturbations to the frictional melting rate quickly over great distances.

In the experiments conducted here, two factors may be of additional importance in reducing the rate at which the sliding transition can propagate upstream via longitudinal-stress gradients. First, we have specified that the upstream boundary is always a flow divide at which, by definition, the rate of frictional melting must go to zero. In reality, a wave of thinning propagating upstream would force divide migration and the frictional-melt rate at the former divide location would increase over time as the divide migrated away. The timescale for divide migration to significantly affect the melt-rate profile is,

however, likely to be longer than the timescale over which the sliding transition can propagate continuously via longitudinal-stress gradients. Thus, it seems unlikely that our choice for the upstream boundary condition is an important factor at limiting the rate at which the sliding transition can propagate upstream.

Second, we have assumed that some spatially constant “base” melting rate exists, presumably due to geothermal energy, and allows sliding to occur everywhere in the domain. Here, this base-melting rate should realistically increase moving upstream due to increasing ice thicknesses approaching the flow divide (assuming a constant geothermal flux). Accounting for this effect might help to maintain the rate at which the sliding transition propagates inland, because the magnitude of the longitudinal-stress gradient required to raise the melt rate to its threshold value, and thus to propagate sliding farther upstream, will be reduced.

When the feedback is included in the model, there are important far-field differences. Maximum thinning rates at some distance upstream, for example at a flow divide, (1) will be larger in magnitude and (2) will occur sooner. These differences will be larger for larger perturbations and for a higher value of the stress exponent, p . Here, we have tested a small range of stress exponents and they are of low order (1 and 3). In reality, assuming that a subglacial till can be treated like a power-law fluid, stress exponents in the range of 5-13 may be more appropriate (Rathbun and others, 2005). For some extreme cases, such as the till beneath Whillans Ice Stream in West Antarctica, the appropriate value may be closer to 100 (Kamb, 1991). It then seems likely that the differences presented here between models with and without the feedback are on the low end of differences that might be expected for real ice streams and outlet glaciers. If so, the feedback could have important implications for the magnitude and the speed at which perturbations travel up ice streams and outlet glaciers.

We have applied small perturbation to the basal strength (decreasing it by a maximum of 15%) but we applied that perturbation to a large portion of the model domain very quickly (in 1 year). Real-world analogs for this type of perturbation might include the penetration of a water-filled crevasse to the bed of an ice sheet

followed by the sudden draining of a surface lake, as in Greenland (Zwally and others, 2002), and the rapid movement of “pockets” of subglacial water beneath the ice-stream tributaries in West Antarctica (Gray and others, 2005). In both cases, large areas of the bed would experience rapid increases in lubrication and, presumably, jumps in sliding speed. Other types of perturbations that could induce the “pulling” stress needed to initiate the feedback would occur less rapidly (over tens of years) and therefore might be of lesser magnitude. These include loss of basal traction provided by an ice plain (e.g. Payne and others, 2004) or the collapse and removal of an ice shelf or ice tongue, each of which would be followed by acceleration and thinning of grounded ice (Scambos and others, 2004; Joughin and others, 2004).

It is not clear exactly how the perturbations that have been applied here scale to real-world perturbations. The largest (ΔD of 15%, $p=3$) leads to a net thickness loss at the flow divide, ~ 300 km upstream of the perturbation, of ~ 75 m ($<4\%$). Approximately $2/3$ of this loss occurs during the first 1000 a after the perturbation and $\sim 1/4$ occurs during the first 500 a. Maximum thinning rates at the divide are on the order of 0.05 m a^{-1} . By way of comparison, average thinning rates along the ~ 200 km trunk of Pine Island Glacier, West Antarctica, are on the order of 0.75 m a^{-1} (Shepherd and others, 2001). Along nearby portions of the drainage basin not directly on the glacier trunk, average thinning rates are on the order of 0.10 m a^{-1} .

Our model does not account for the flow resistance provided by drag against valley sidewalls (in the case of an outlet glacier) or against slower moving ice (in the case of an ice stream). In reality, when a sudden reduction in basal resistance leads to a sudden increase in sliding speed, some fraction of the reduced basal resistance is supported at the margins through lateral-stress gradients. Here, longitudinal-stress gradients accommodate a reduction in basal drag by increasing it elsewhere; ultimately, the bed still provides all of the resistance to flow. This omission means that we have overestimated increases in basal friction, and hence overestimated increases in the melting rate, that occur upstream from the sliding

transition after a perturbation. We expect that similar experiments conducted using a three-dimensional model would give results similar to those shown here but that the model response, with respect to propagation of the sliding transition and changes in geometry, would be of smaller magnitude.

We have reduced the link between the basal resistance and the basal-water system to one in which the melt *rate* is the sole control on basal resistance. In reality, the amount of resistance the bed provides is a function of the water content at the bed, in which case water transport (import and drainage) and storage are important. These additional factors could either impede or enhance the positive feedback discussed above. In a “drainage limited” state (Raymond, 2000), changes in the melting rate are immediately accommodated by the basal-water system and the feedback investigated here might never operate at all (the timescale for the basal-water system to adjust to an increase in melt rate is shorter than the timescale over which the increased melt rate leads to a reduction in basal resistance). In this case, the basal-water system would serve to impede the feedback discussed above. On the other hand, if drainage was slow and/or storage capacity was significant, an increase in melt rate might affect basal resistance long after the melt rate decreased to or below former levels (the timescale for the basal-water system to adjust to an increase in melt rate is longer than the timescale over which the increased melt rate leads to a reduction in basal resistance). In this case, the basal-water system would serve to enhance the feedback discussed above.

CONCLUSIONS

A feedback between sliding, frictional melting, and longitudinal-stress gradients allows a slow-to-fast sliding transition to migrate upstream over time, assuming that an appropriate perturbation exists (a “pulling” stress) to initiate the feedback. An initial, short (~10 a) period of very rapid upstream migration is associated with longitudinal-stress gradients and, for the extreme cases explored here, can account

for 70% of the total upstream distance that the transition moves. Upstream migration of the sliding transition increases with the size of the causative perturbation and with the degree of non-linearity assumed in the relation linking basal stress to basal motion. Here, reducing the stiffness of the basal layer by 15% caused the sliding transition to migrate upstream a distance of ~ 35 ice thicknesses in ~ 250 a.

The feedback also has important far-field effects: upstream from the perturbation, maximum thinning rates will be larger and will occur sooner than when there is no feedback. These differences increase as the initial perturbation increases and/or as the degree of non-linearity in the relation linking basal stress to basal motion increases. Here, the maximum differences were on the order of 30% for a small degree of non-linearity (stress exponents of 1 and 3). For real systems with stress exponents likely to be more on the order of 10, much larger differences can be expected.

The model results and the interpretation presented here are contingent on the assumption that basal sliding is a function of the basal-melt rate. It could be more realistic to assume that basal sliding is related to the total amount of water at the ice-bed interface. In that case, details of the basal-water system would become important and future work should focus on examining how these details affect the conclusions made here.

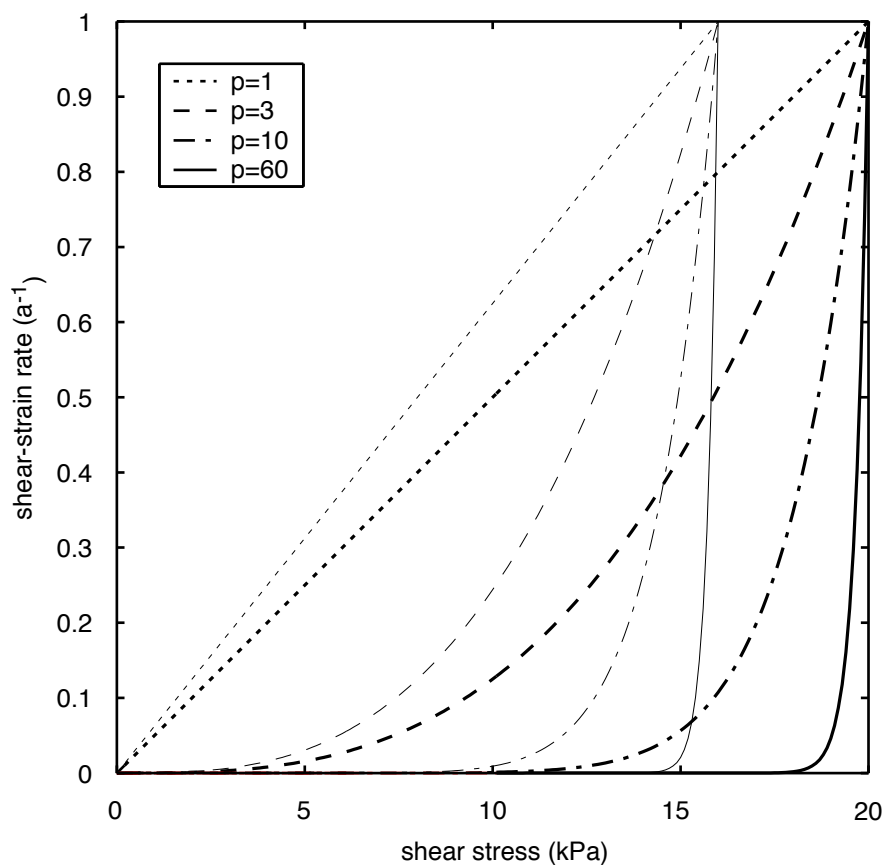


Figure 4.1: Shear strain-rate versus shear stress in basal layer. Heavy lines are for $D=20 \text{ kPa } a^{1/p}$ and thin lines represent a reduction in that value by 20% after passing some melting-rate threshold.

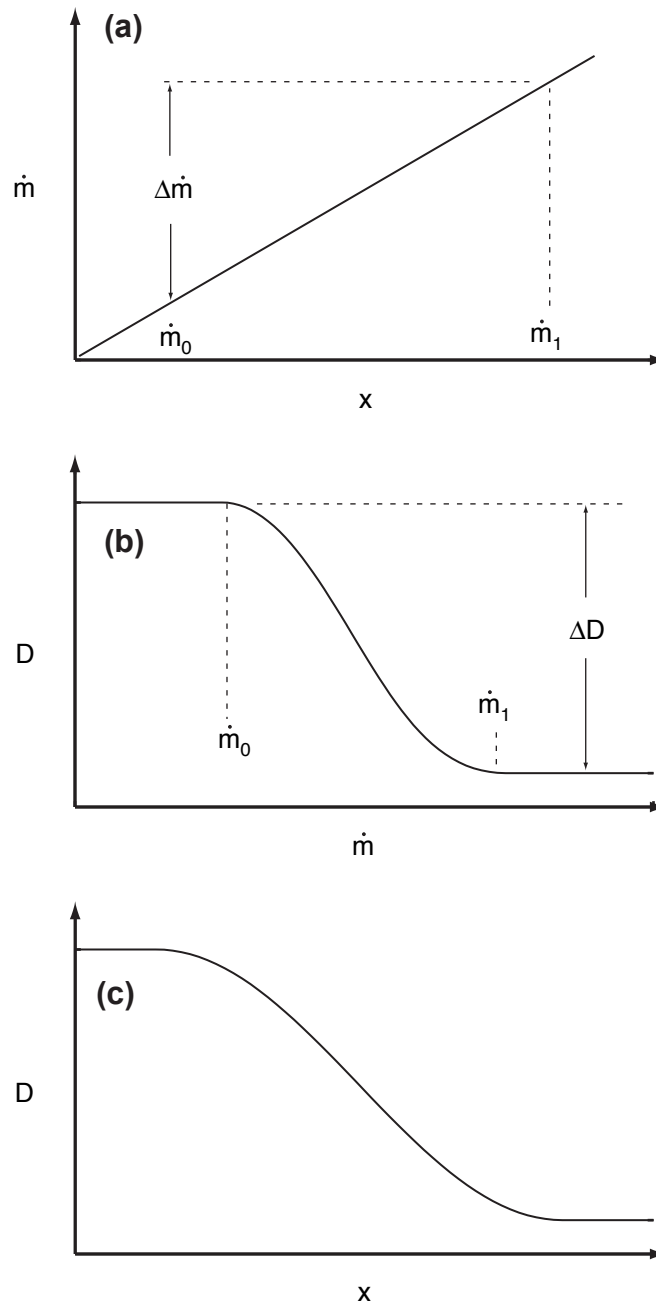


Figure 4.2: Softness parameter as a function of frictional melting rate. Schematic plot of the relationship between (a) the basal melting rate, \dot{m} , and the along-flow coordinate, x (b) the softness parameter, D , and the melting rate, and how these translate to (c) the description of D as a function of the along-flow coordinate.

Figure 4.3: Time series of the longitudinal-stress gradients for the reference model. The along-flow coordinate is given by x , the height above the glacier bed is given by z , ΔD is 10% and $p=3$. The vertical dashed line marks the midpoint of the sliding transition. Vertical and horizontal coordinates are scaled by the initial ice thickness at the transition, at $x=0$. The longitudinal-stress gradient is scaled by the magnitude of the maximum instantaneous longitudinal-stress gradient (that at $t=0$). Note that the colorbar axes span a different range in each panel.

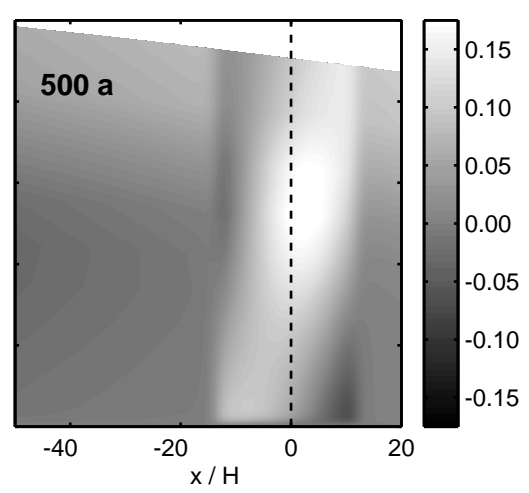
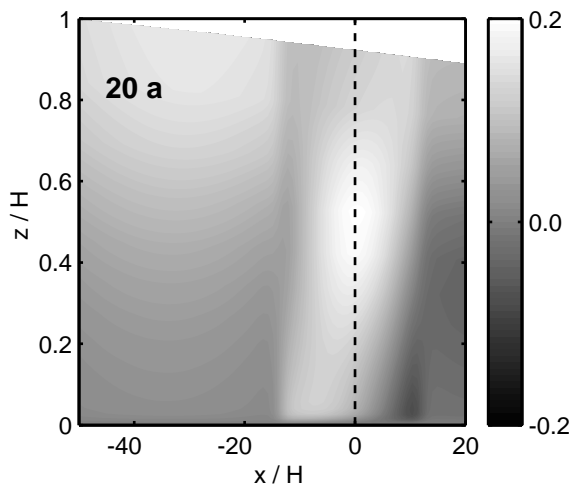
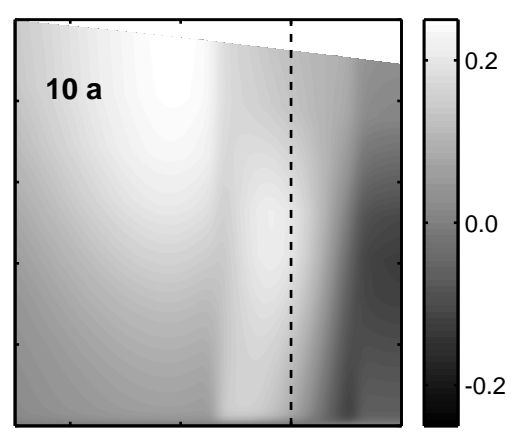
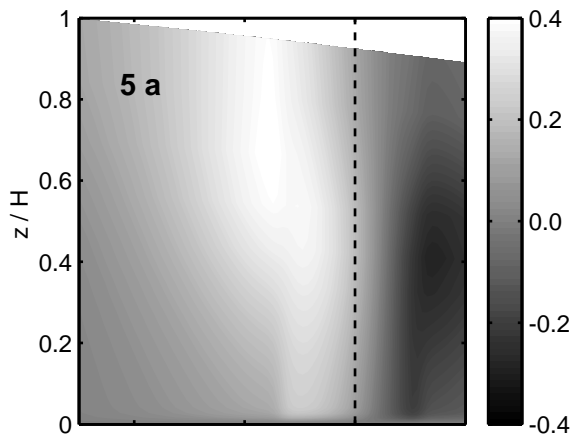
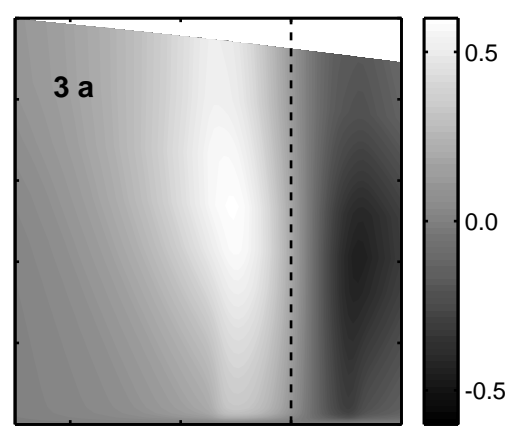
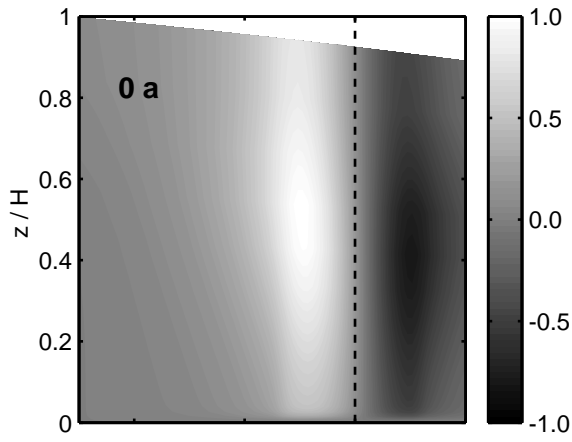
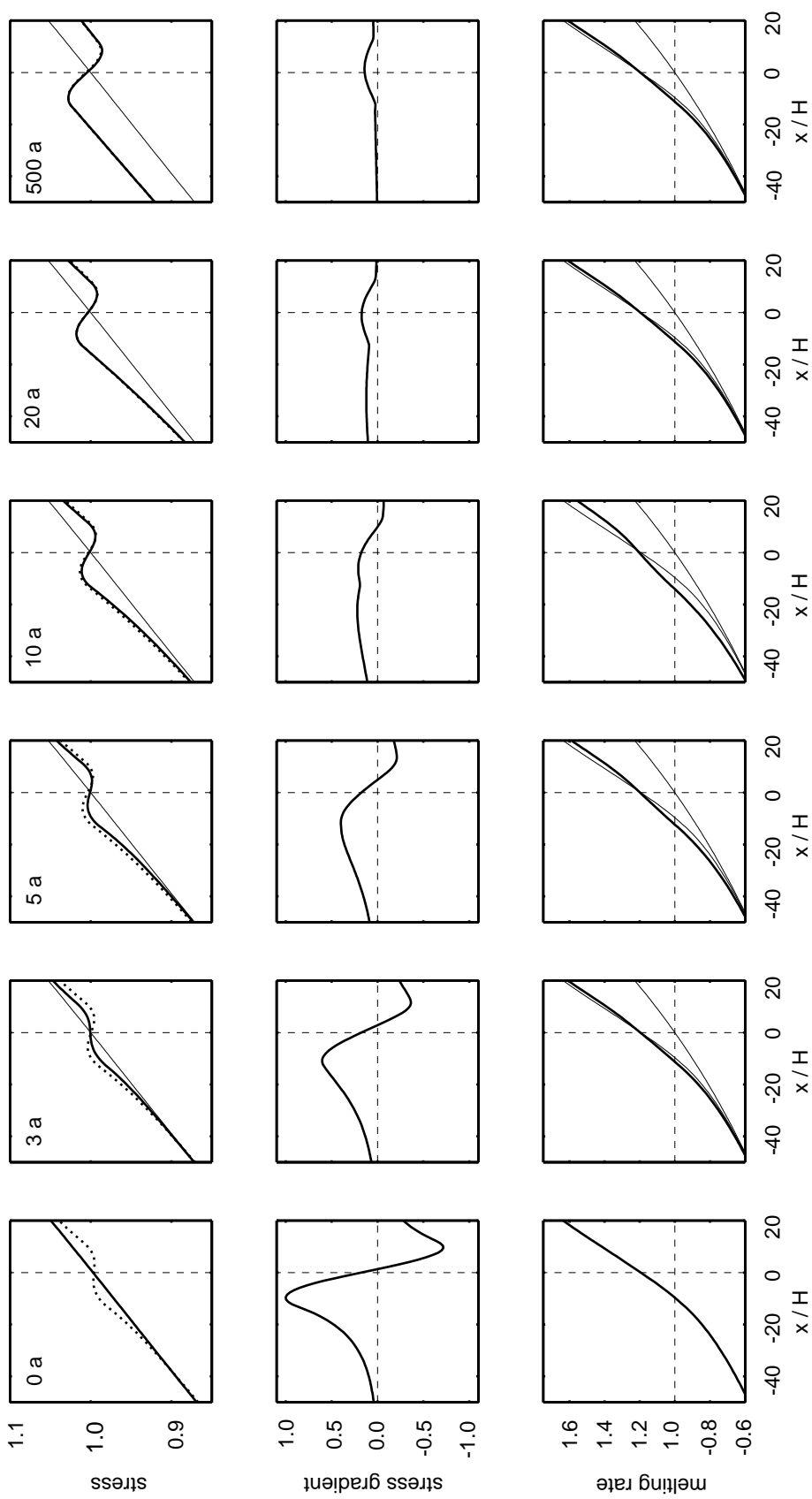


Figure 4.4: Stress balance and melting rate for the reference model. Panels in each column cover the same region and represent the same times and values of ΔD and p as in Figure 4.3. Top row: Driving stress (solid) and basal drag (dashed) scaled by the initial driving stress at $x=0$ (ND on vertical axes denotes non-dimensional values). The thin black line is the steady-state driving stress prior to the perturbation. Middle row: Depth-averaged longitudinal-stress gradient scaled by the magnitude of the maximum instantaneous longitudinal-stress gradient. Bottom row: Frictional-melting rate scaled by the value of the threshold-melting rate. For reference, the two thin lines are the initial (steady state) melting-rate profile and the instantaneous melting-rate profile after the perturbation.



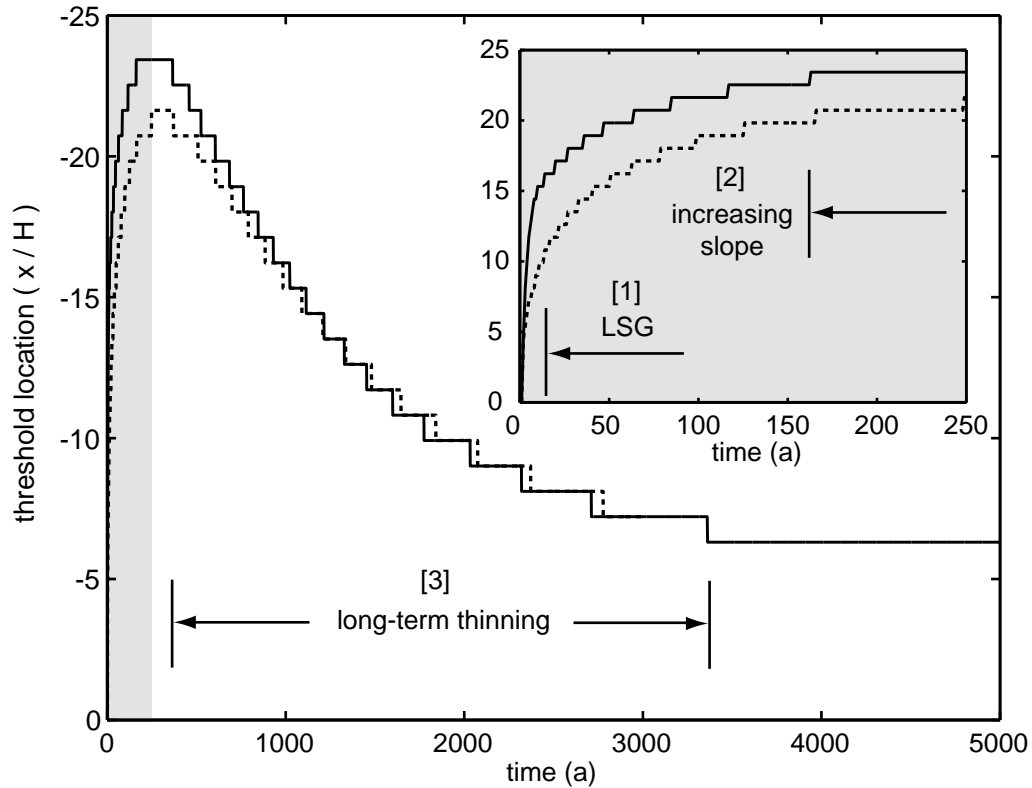


Figure 4.5: Evolution of the melting rate for the reference and linked models. Curves track the location of the threshold-melting rate \dot{m}_0 relative to its initial location. The dashed and solid curves represent results for the reference and linked models, respectively. For the linked model, the location of \dot{m}_0 is synonymous with the location at which the reduction in the softness parameter starts (see Figure 2). Zero on the vertical axis coincides with 0 on the horizontal axis in Figures 3-6. The inset shows details during the first 250 a after the perturbation.

Figure 4.6: Time series of the longitudinal-stress gradients for the linked model. The along-flow coordinate is given by x , the height above the glacier bed is given by z , ΔD is 10% and $p=3$. The vertical dashed line marks the midpoint of the sliding transition. Vertical and horizontal coordinates are scaled by the initial ice thickness at the transition, at $x=0$. The longitudinal-stress gradient is scaled by the magnitude of the maximum instantaneous longitudinal-stress gradient (that at $t=0$). Note that the colorbar axes span a different range in each panel.

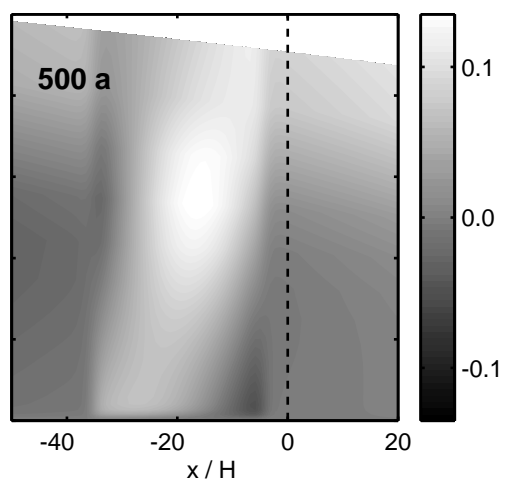
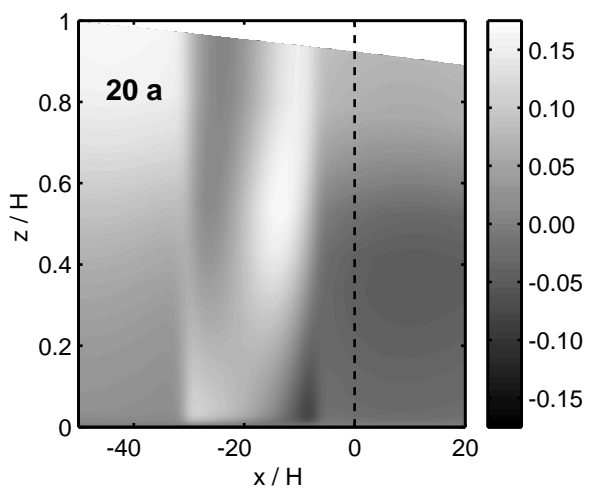
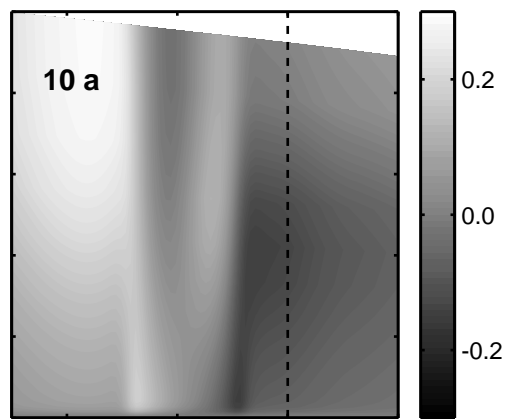
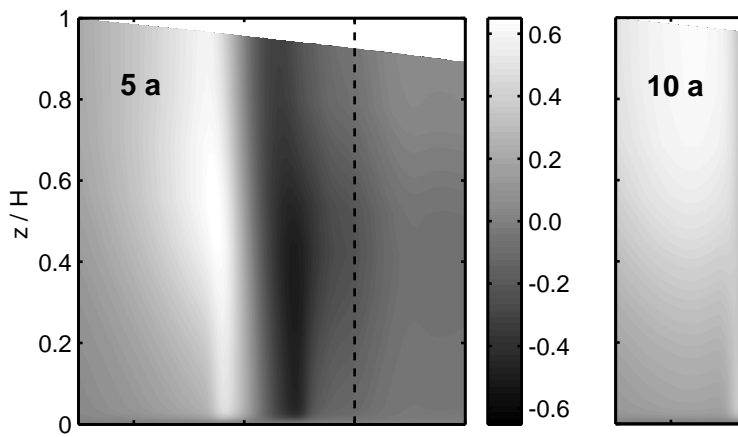
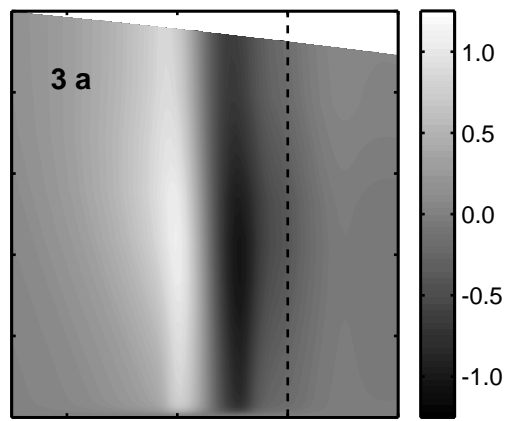
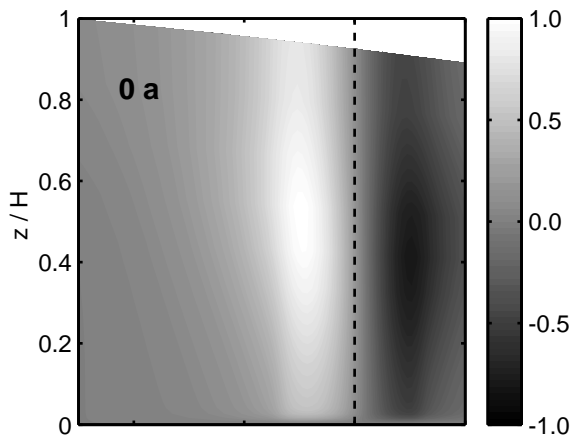
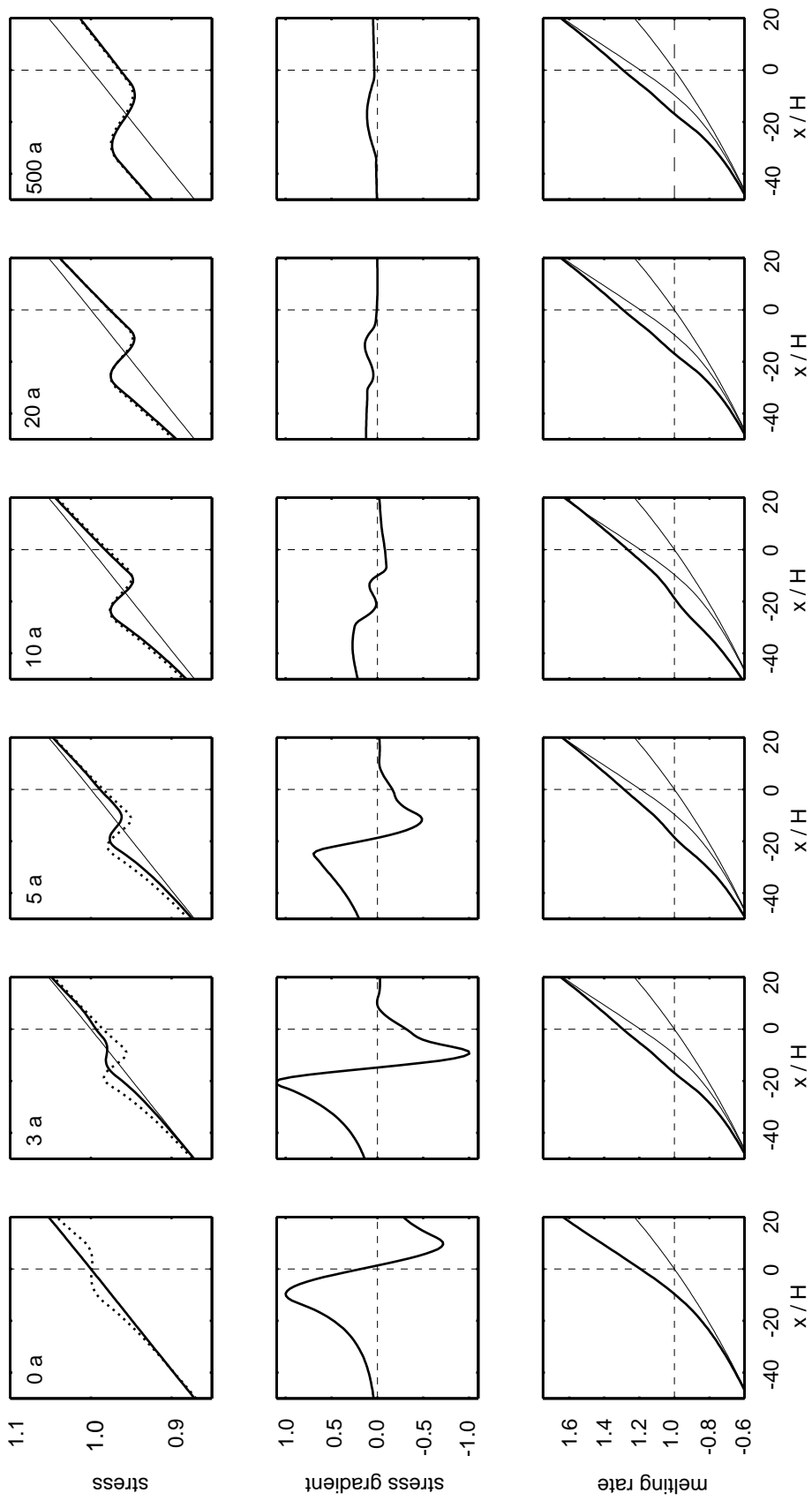


Figure 4.7: Stress balance and melting rate for the linked model. Panels in each column cover the same region and represent the same times and values of ΔD and p as in Figure 4.6. Top row: Driving stress (solid) and basal drag (dashed) scaled by the initial driving stress at $x=0$ (ND on vertical axes denotes non-dimensional values). The thin black line is the steady-state driving stress prior to the perturbation. Middle row: Depth-averaged longitudinal-stress gradient scaled by the magnitude of the maximum instantaneous longitudinal-stress gradient. Bottom row: Frictional-melting rate scaled by the value of the threshold-melting rate. For reference, the two thin lines are the initial (steady state) melting-rate profile and the instantaneous melting-rate profile after the perturbation.



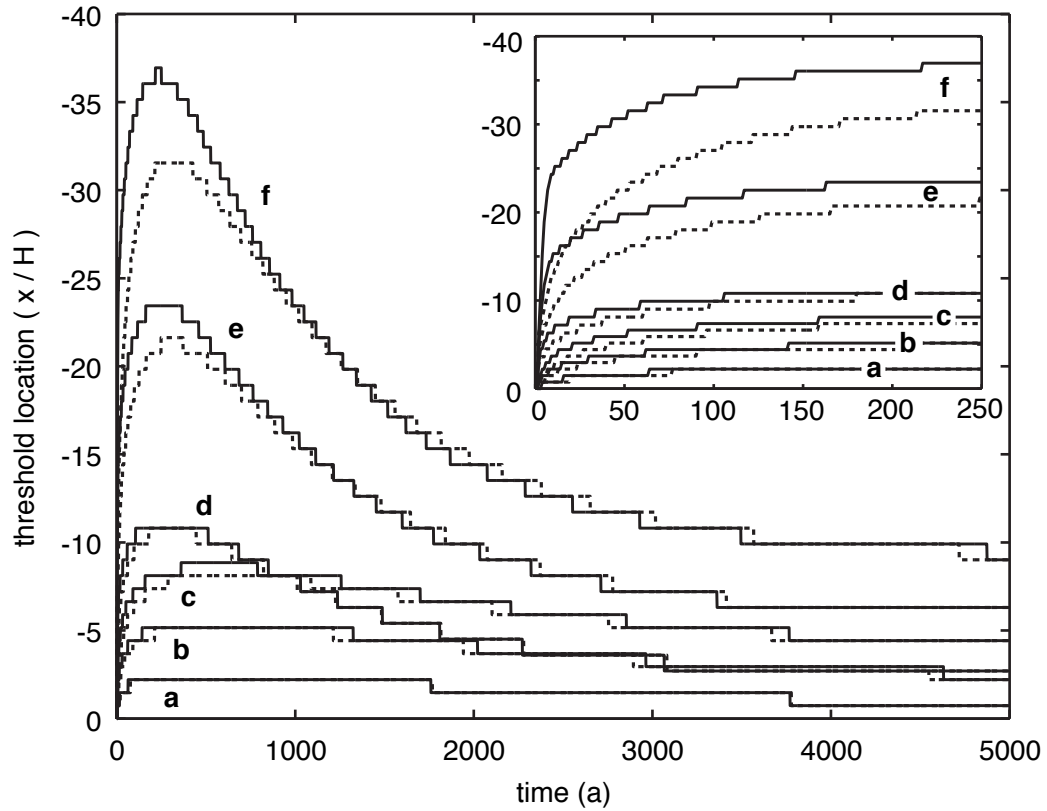


Figure 4.8: Evolution of the melting rate for all models (as in Figure 5). (a) ΔD of 5%, $p=1$ (b) ΔD of 10%, $p=1$ (c) ΔD of 15%, $p=1$ (d) ΔD of 5%, $p=3$ (e) ΔD of 10%, $p=3$ (f) ΔD of 15%, $p=3$. Zero on the vertical axis coincides with 0 on the horizontal axis in Figures 3-6.

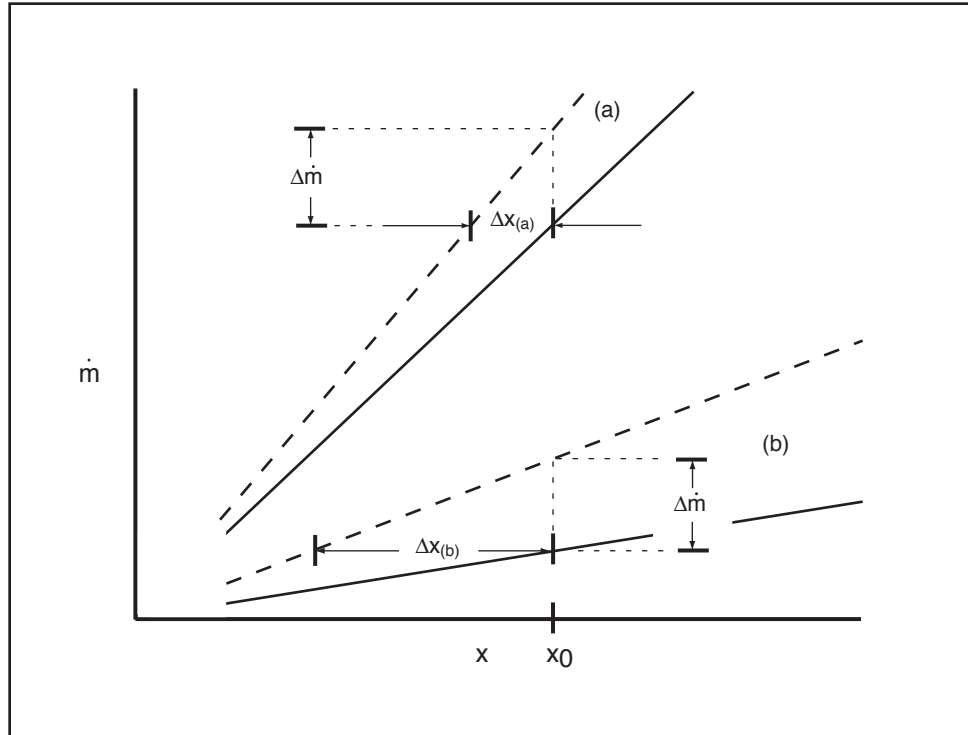


Figure 4.9: Shift of melt-rate profile after a perturbation to the melting rate. Solid lines in (a) and (b) represent two different, initial melting rate profiles that experience the same perturbation to the melting rate, $\Delta\dot{m}$, at location x_0 . After the perturbation (dashed lines), the melting rate initially at x_0 has been displaced upstream by a distance Δx . The horizontal axis encompasses a distance of several tens of ice thicknesses near the location of the melting-rate perturbation.

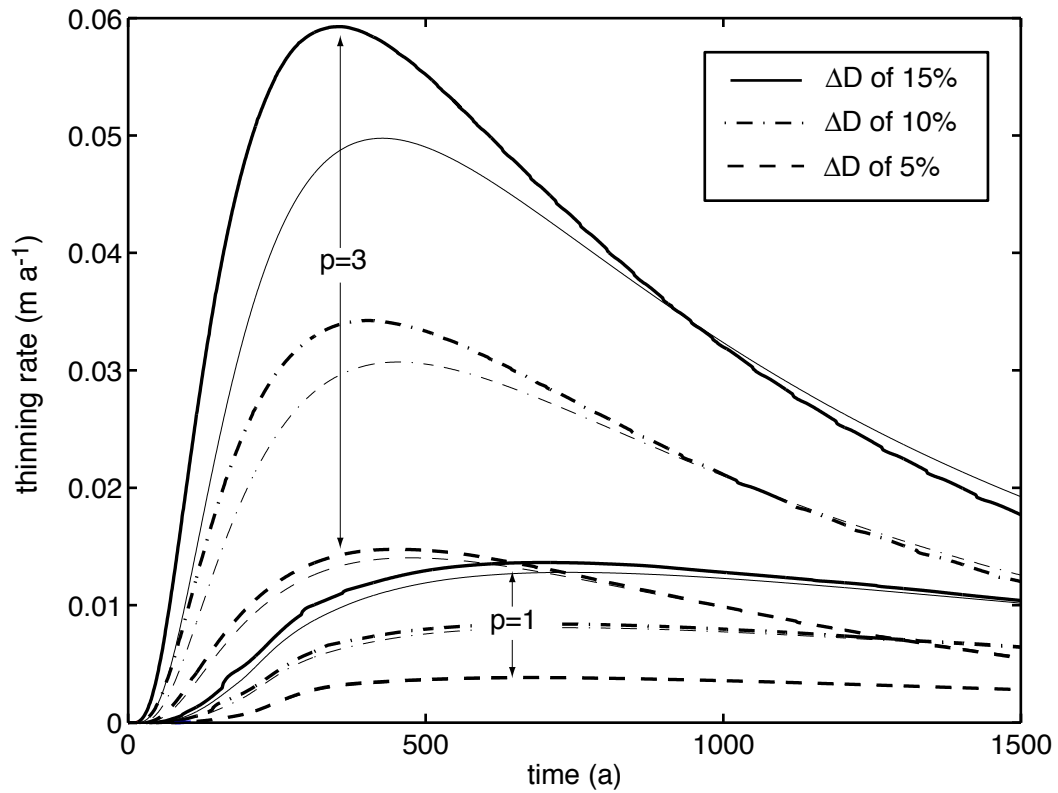


Figure 4.10: Thinning rate as a function of time upstream from the perturbation. Curves represent modeled thinning rates at a distance of $150\times$ the ice thickness upstream from the initial perturbation. Thin lines represent the reference models and heavy lines represent the linked models. Dashed lines represent the response to ΔD of 5%, dash-dot lines represent the response to ΔD of 10%, and solid lines represent the response to ΔD of 15%. Curves for $p=1$ and $p=3$ are labeled.

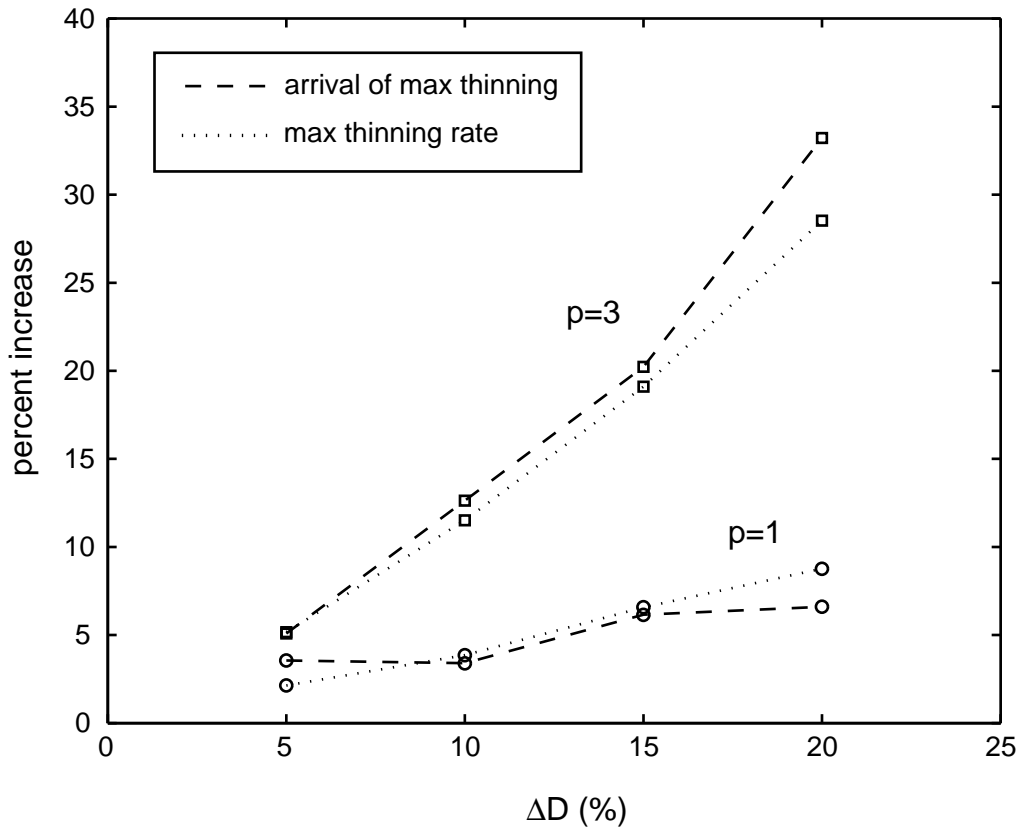


Figure 4.11: Relative magnitude and timing of thinning for reference and linked models. Lines represent the percent difference in the maximum-thinning rate and the timing of maximum-thinning rate for the curves shown in Figure 10. The change in the softness parameter from its initial value is plotted on the horizontal axis. The percent increase in the maximum rate of thinning is plotted on the vertical axis (dotted lines), as is the percent increase in how soon that maximum occurs (dashed lines), for the linked model relative to the reference model (positive numbers denote maximum thinning rates that are larger and occur sooner in the linked model). Circles and squares represent results for $p=1$ and $p=3$, respectively.

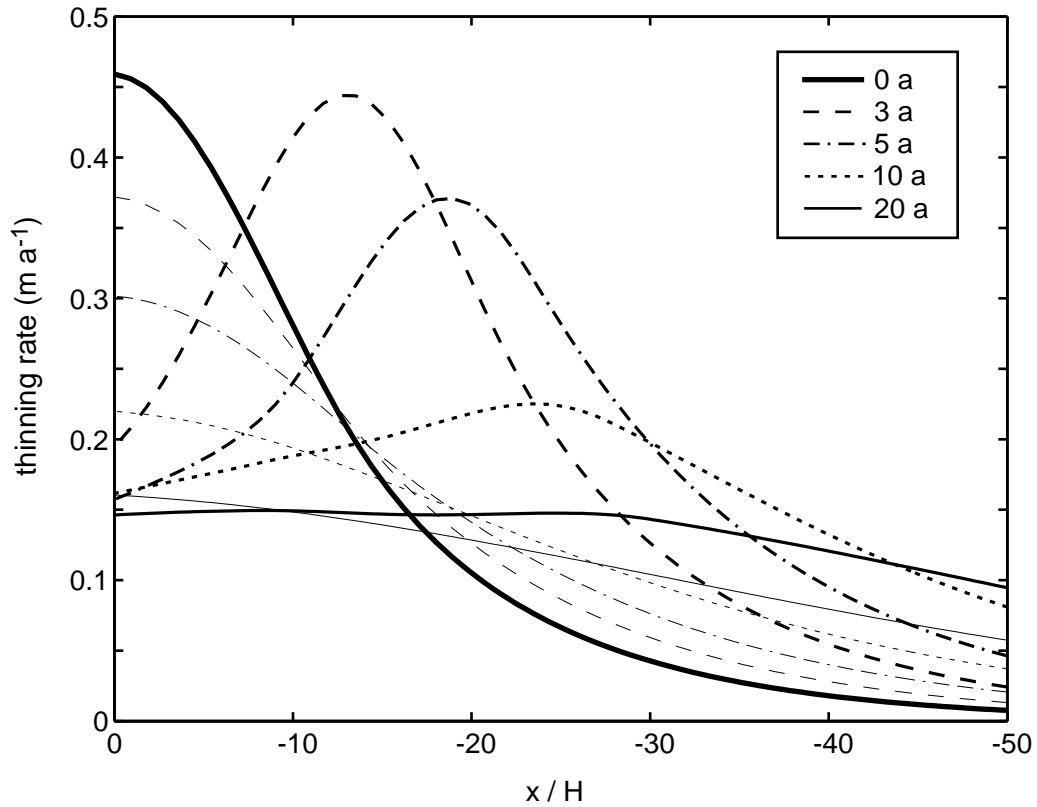


Figure 4.12: Thinning rate as a function of distance upstream from the perturbation. Light lines represent the reference model and heavy lines represent the linked model discussed in Figures 4.3-4.4 and 4.6-4.7 above. The very-heavy solid line represents the thinning rate for the initial perturbation, which is the same for both. Dashed, dash-dot, dotted, and solid lines represent thinning rates at 3, 5, 10, and 20 a after the initial perturbation, respectively.

**MODELING THE DYNAMIC RESPONSE OF A CRATER GLACIER TO
LAVA-DOME EMPLACEMENT: MOUNT ST. HELENS,
WASHINGTON, U.S.A.**

This chapter has been accepted for publication in the *Annals of Glaciology*. It was presented orally by co-author J.S. Walder (USGS Cascades Volcano Observatory, Vancouver, WA) at the International Symposium on Earth and Planetary Ice and Volcano Interactions in Reykjavik, Iceland, held on June 19-23, 2006.

SUMMARY

The debris-rich glacier that grew in the crater of Mount St. Helens after the volcano's cataclysmic 1980 eruption was split in two by a new lava dome in 2004. For nearly six months, the eastern part of the glacier was squeezed against the crater wall as the lava dome expanded. Glacier thickness nearly doubled locally and surface speed increased substantially. As squeezing slowed and then stopped, surface speed fell and ice was redistributed downglacier. This sequence of events, which amounts to a field-scale experiment on the deformation of debris-rich ice at high strain rates, was interpreted using a two-dimensional flowband model. The best match between modeled and observed glacier surface motion, both vertical and horizontal, requires ice that is about 5 times stiffer and 1.2 times denser than normal, temperate ice. Results also indicate that lateral squeezing, and by inference lava-dome growth adjacent to the glacier, likely slowed over a period of about 30 days rather than stopping abruptly. This finding is supported by geodetic data documenting dome growth.

INTRODUCTION

Mount St. Helens is an active volcano with a glacier in its crater. The eruption that began in September 2004 has been largely a quiescent one featuring the growth of a lava-dome complex (Vallance and others, in press). Early in the eruption sequence, a “fin” of solidified magma broke through the surface of the $\sim 1 \text{ km}^2$ glacier and grew southward, intersecting the south crater wall in mid-November 2004 and cleaving the crater glacier into eastern and western halves (Figure 5.1; Walder and others, this volume; in press). The fin then expanded eastward, squeezing the east crater glacier against the east crater wall until mid- to late-April 2005, when dome growth shifted to the west. The response of the east crater glacier to the squeeze event, and its aftermath, was characterized by photography, photogrammetry, and single-frequency, helicopter-deployed Global Positioning System (GPS) stations on the glacier. The east crater glacier underwent a hitherto never-described style of deformation: strain rates were of a similar order of magnitude to those observed in glacier surges (Kamb and others, 1985), but here the causative stresses were oriented *across* flow, rather than *along* flow.

As the squeeze event progressed, the thickness of ice in the upper part of the east crater glacier became 2 to 3 times that in the lower part (Figure 5.2), so if deformation were only by simple shear in the vertical, the difference in surface velocity between the upper and lower portions of the east crater glacier should have been a factor of about 16 to 80 for a flow-law exponent $n = 3$ (van der Veen, 1999, pp. 103-104). The observed velocity difference (Figure 5.2), however, was only a factor of 3 to 4. Walder and others (2005) suggested an explanation: the lower third of the glacier, which was not squeezed, acted as a “dam” that pushed back against the ice upstream. This would lead to a large, longitudinal stress gradient. To assess this hypothesis, we use a two-dimensional, higher-order flowband model to simulate evolution of the east crater glacier.

To produce a best match between the model and the observations during the squeezing event, we assume that the glacier’s large debris content (discussed

below) affects the “stiffness” of the ice as well as its effective density, and we vary these two variables in order to tune the model. Independent data provide bounds on the debris content (and thus the effective density of the ice), thereby allowing us to constrain the rheological properties of temperate glacier ice containing a large fraction of rock debris. In effect, the combination of our flow model and the observations from Mount St. Helens in early 2005 serve as a large-scale experiment on the deformation of debris-laden ice. Unlike in a laboratory experiment (Jacka and others, 2003), however, the glacier contains debris ranging in size from silt and sand up to boulders.

FIELD SETTING

The Mount St. Helens crater glacier formed following the catastrophic eruption of 1980 and the subsequent growth of a lava dome from 1980 to 1986. It is fed by copious avalanching of snow and rock debris from the crater walls. Given these hazardous conditions, our knowledge of the glacier’s development comes almost entirely from occasional visual inspection and photogrammetry. Comparison of sequential digital elevation models (DEMs) revealed that the crater-floor fill accumulated up to mid-1988 was, on average, about 60% rock debris by volume (Mills, 1992). A similar exercise by Schilling and others (2004) showed that by September 2000, the average volumetric rock content of the entire glacier was down to 30%. Crevasses - indicators of flow - were first noticed on aerial photographs taken in September 1996. The general picture presented by these studies, along with field observations by one of us (JSW) and other U.S. Geological Survey scientists, is of crater-floor fill that grades upward from mostly rock - and clearly not glacier ice in a rheological sense - to “dirty” firn and ice.

For purposes of modeling, we wish to consider as “glacier” only the portion of the crater-floor fill that behaves as a creeping solid, and to exclude, as best we can, the lowermost, rock-rich material, which probably behaves as a Coulomb-

frictional material with ice in the interstices. Picking the effective glacier bed is admittedly an uncertain exercise. Our choice is to pick the glacier bed as the crater-floor surface defined by DEMs for October 12, 1986 and November 12, 1986. The rationale for this choice is presented by Walder and others (this volume; in press). Average rock content of the glacier so-defined is about 15% by volume. We recognize that the creeping material may in fact extend below the 1986 surface, in which case the average rock content would be greater.

FLOW MODEL

Model Description

Our flowband model solves the full 2D momentum-balance equations and includes terms to account for converging and diverging flow. The model is based on the Finite Volume Method (FVM) (Patankar, 1980; Versteeg and Malalasekera; 1995) and is described fully in Price and others (2004). Here, we discuss relevant portions of the model including the governing equations, the general solution method, and the parameterizations that account for the effects of changes in flowband width.

For low-Reynolds number flow of a viscous fluid, conservation of momentum in a Cartesian reference frame is expressed as

$$\rho g_i + \frac{\partial \sigma_{ij}}{\partial x_j} = 0, \quad (i, j = x, y, z), \quad (5.1)$$

where x , y , and z are the along-flow, across-flow, and vertical-coordinate directions and repeat indices imply summation. The first term on the left-hand side of Equation (5.1) is the body force, the product of ice density, ρ , and the acceleration due to gravity, g_i . The second term is the stress divergence, where σ_{ij} are components of stress and related to deviatoric stress, τ_{ij} , and the mean compressive stress, P , through

$$\sigma_{ij} = \tau_{ij} - P\delta_{ij}. \quad (5.2)$$

The constitutive relation is written according to Nye's generalization of Glen's flow law,

$$\tau_{ij} = 2\eta\dot{\varepsilon}_{ij}, \quad (5.3)$$

(e.g., van der Veen, 1999, p. 13-15) where ε_{ij} is strain-rate,

$$\dot{\varepsilon}_{ij} = \frac{1}{2} \left(\frac{\partial u_i}{\partial x_j} + \frac{\partial u_j}{\partial x_i} \right), \quad (5.4)$$

η is the effective viscosity,

$$\eta = \frac{1}{2} EB(T) \dot{\varepsilon}_e^{\frac{1-n}{n}}, \quad (5.5)$$

and the u_i represent components of the velocity vector (henceforth called u , v , and w) parallel to the x , y , and z directions, respectively. In Equation (5.5), E is a scalar enhancement factor (equal to 1 for "normal" ice), $B(T)$ is a temperature-dependent rate factor (here taken constant), n is the power-law exponent (here taken equal to 3), and $\dot{\varepsilon}_e$ is the effective-strain rate, given by

$$2\dot{\varepsilon}_e^2 = \dot{\varepsilon}_{ij}\dot{\varepsilon}_{ij}. \quad (5.6)$$

The ice is assumed to be incompressible:

$$\frac{\partial u}{\partial x} + \frac{\partial v}{\partial y} + \frac{\partial w}{\partial z} = 0. \quad (5.7)$$

We solve Equation (5.1) in a boundary fitted, orthogonal, curvilinear-coordinate system. The transformation between this and a standard 2D Cartesian coordinate system is discussed in detail in Price and others (in preparation). The model solutions we discuss below (e.g. velocity fields) have been rotated into a Cartesian coordinate system.

General Solution Method

Integrating Equation (5.7) over a single finite volume (i.e. a single grid cell) gives

$$\rho(u_D A_D - u_U A_U) + \rho(v_L A_L - v_R A_R) + \rho(w_T A_T - w_B A_B) = 0, \quad (5.8)$$

where ρ is density; the subscripts U , D , T , B , L , and R refer, respectively, to the upstream, downstream, top, bottom, left, and right faces of a single cell; and A is the area of the relevant cell face: for example, $A_U = W_U \Delta z_U$, where W_U and Δz_U are the flowband width and volume height, respectively, at the upstream cell face. Equation (5.8) states that the net mass flux into and out of a volume sums to zero. A flowband is bounded by two flowlines and if, for the moment, we take the flowband (and thus volume) width as constant, the second term in Equation (5.8) is zero. Using equations (2) through (6) in Equation (5.1) with an estimated pressure field and solving computationally, we obtain estimated velocity fields u^* and w^* . Inserting these values into the remaining terms from Equation (5.8) we obtain

$$\rho(u_D^* A_D - u_U^* A_U) + \rho(w_T^* A_T - w_B^* A_B) = S, \quad (5.9)$$

where S is non-zero because, in general, our initial estimate for the velocity field will not satisfy continuity. To satisfy continuity the mass source (or sink), S , at each volume is eliminated through an iterative pressure-correction method (Patankar, 1980). A non-zero mass source defines a pressure perturbation that improves upon the estimated pressure and velocity fields. Through Equation (5.9), the updated

velocity field leads to a further improvement in the estimate for the mass source (i.e. one with a smaller magnitude) and a further improvement on the estimated pressure perturbation. Simultaneously, the updated velocity field is used to update the estimated effective-viscosity through Equations (4) and (5). Iterations continue until the solution has converged.

The converged velocity field is projected forward in time to predict the change in the shape of the free surface (and thus the change in the domain geometry) at a future time step. Changes in domain geometry and the redistribution of mass within the (x,z) plane are accounted for when regriding the finite-volume mesh at the start of each time step.

Changes in Flowband Width

Our model accounts for the kinematic and dynamic effects of a changing flowband width, $W=W(x,t)$. During any single time step, spatial changes in flowband width affect the velocity field directly, through continuity, and indirectly, through the dependence of the effective-viscosity on strain rate. The direct effect is accounted for automatically when specifying $W(x,t)$ through Equation (5.8). The indirect effect is accounted for by including a non-zero, transverse-normal strain rate in Equation (5.6), parameterized as

$$\dot{\epsilon}_{yy} = \frac{\partial v}{\partial y} = \frac{u}{W} \left(\frac{\partial W}{\partial x} \right), \quad (5.10)$$

which can be derived from considerations of continuity along a flowband (Waddington, 1981).

To maintain global continuity, special considerations are required when changing the flowband width from one time step to another. While regriding of the domain accounts for mass redistribution in the (x,z) plane (along the glacier centerline), flowband narrowing (or widening) over time leads to mass convergence towards (or divergence from) this plane. When the flowband width changes from

one time step to another, this additional mass must be introduced (or removed) from the model domain. The solution method discussed above offers a natural means for doing this: in any volume affected by a time change in width, the mass source term in Equation (5.9) is augmented by the additional amount

$$S_{W(x,t)} = \rho \cdot \Delta x \Delta z \cdot \left(-\frac{\partial W}{\partial t} \right), \quad (5.11)$$

where $\partial W/\partial t$ is the rate of flowband narrowing ($\partial W/\partial t < 0$) or widening ($\partial W/\partial t > 0$) and $\Delta x \Delta z$ is the area of the volume face through which that mass passes. The negative sign in Equation (5.11) ensures that, at the glacier centerline, convergence due to flowband narrowing is treated as a mass source (and divergence due to flowband widening is treated as a mass sink). When $\partial W/\partial t \neq 0$, mass converging on, or leaving the plane of the glacier centerline is automatically redistributed by the flow field so that global continuity is maintained. As with along-flow changes in width, temporal changes in width add an additional strain rate component to the right-hand side of Equation (5.6). This term is given by

$$\dot{\epsilon}_{\dot{W}} = \frac{1}{W} \left(\frac{\partial W}{\partial t} \right). \quad (5.12)$$

Resistance from Valley Sidewalls

To approximate the effects of drag against valley sidewalls, the body force (the first term on the left-hand side of Equation (5.1)) is multiplied by a shape factor, $F_s \leq 1$. We use shape factor definitions from Nye (1965) assuming an elliptic-shaped channel, a width equal to our specified flowband width, and a specified ice thickness.

Observations (Walder and others, this volume; in press) indicate that as the squeezing event progressed, the surface of east crater glacier bulged markedly, and that a significant fraction of the glacier thickness was not in contact with either the

lava dome or the east crater wall. This effect has to be accounted for to avoid overestimating the effects of side drag. On the basis of cross sections in Walder and others (2006), we estimate that side drag was effective over a vertical distance of about 50 m greater than the pre-eruption, centerline ice thickness.

Initial Conditions

Profiles of the initial glacier-surface and bed elevations are necessary to define the initial domain geometry. We use surface-elevation data from photogrammetrically derived Digital Elevation Models (DEMs), as described in Walder and others. Our analysis is limited to a period of time for which the glacier can be adequately described by a 2D flow model. We choose an initial glacier-surface elevation profile, along the approximate centerline shown in Figure 5.1, from 3 January 2005 (model day 0), by which time east crater glacier was clearly separated from its western counterpart, and compression along the upper portion of the glacier was oriented almost entirely across-flow. Because the DEM for January 3 covers only the upstream ~ 700 m of the glacier centerline, we are forced to estimate a surface-elevation profile for the downstream ~ 600 m of the glacier centerline. For the region along flow from ~ 900 -1300 m we use the next available surface elevation profile, that from 19 April 2005 (model day 107). A comparison of this and other profiles shows that there is very little elevation change along the stagnant, lower portion of the glacier. For the region of the centerline from 700-900 m along flow, we have manually interpolated between the 3 January and 19 April profiles guided by the surface shape in subsequent elevation profiles. Bed elevations along the same profile are held constant and are based on surface elevation of the crater floor in October/November 1986, as discussed above. Figure 5.3 shows these longitudinal elevation profiles as well as the finite volume grid at the start of the model run.

One other necessary initial condition is an estimate for the effective viscosity of the ice, which we take from Equation (5.5) assuming temperate ice and a value of 0.001 day^{-1} for $\dot{\epsilon}_e$.

Boundary Conditions

Deformation of the upper part of east crater glacier was clearly dominated first by the compression applied by the expanding lava dome, and afterwards by relaxation of the greatly thickened ice. In contrast, the speed of GPS station ICY4 (Figure 5.2), downglacier of the squeeze zone (Figure 5.1b), was in fact similar to what one would estimate from a balance-velocity argument (Walder and others, this volume), and the surface elevation of the lower part of the glacier changed very little during the squeeze event. These observations motivate some simplifying assumptions with respect to boundary conditions. First, we assume that over the 193-day period considered here, the glacier's response to traditional mass balance forcing is negligible relative to its response to the squeezing event; in other words, the thickening rate is much larger than anticipated surface elevation changes due to accumulation or ablation. Second, we assume that the entire glacier would be relatively stagnant over this same period of time in the absence of lava-dome intrusion. We therefore simply treat the terminus of the glacier as a zero-flux ($u=0$) boundary. The upstream end of the glacier, which was by definition pinned against the crater wall, is also treated as a zero flux boundary.

Walder and others (this volume; in press) interpreted east crater glacier's striking lack of both a spring speed-up and diurnal velocity fluctuations as evidence for absence of basal sliding. This unusual situation arises because there is no drainage system conveying water along the bed of east crater glacier. Instead, meltwater percolates into the thick rock-avalanche deposits underlying the glacier and then into the volcanic edifice. We therefore assign a zero-slip boundary condition at the glacier bed.

The glacier surface, which is specified as stress free, evolves over time in response to the squeezing event. Its evolution serves as our primary constraint for matching the model output to the observations.

Finally, we must specify the rate at which the contact between the lava dome and the glacier moved, as this effect constitutes a mass source in our

numerical scheme. Relevant data from Walder and others (this volume; in press) include: (i) Measurements using sequential DEMs shows that, on average, the contact over the upper ~ 550 m of the glacier migrated at $\sim 1\text{-}2$ m day⁻¹ between 3 January 2005 and 19 April 2005 (model days 0 to 107). (ii) A GPS station *on* the expanding dome moved eastward at an average rate of ~ 0.8 m day⁻¹ on model days 109 to 111. (iii) Comparison of DEMs for 19 April 2005, 13 May 2005 (model day 131), and 15 June 2005 (model day 164) shows that the contact moved no more than ~ 5 m after model day 107. A consistent interpretation requires that eastward dome growth must have greatly slowed after day 111, and motivates the following simple parameterization of squeezing rate: (i) From its upstream limit to 200 m downstream, the rate of flowband narrowing increases linearly downglacier. (ii) From 200 m to some distance D downstream, the rate of flowband narrowing is held constant at 2 m day⁻¹ from 3 January 2005 (model day 0) through 3 March 2005 [model day 60], and 1 m day⁻¹ from then until 22 April 2005 [model day 110]. (iii) Downstream of D , there is no squeezing and the flowband width is held constant. (iv) The squeezing rate after 22 April [model day 110] decreases exponentially in time, with a characteristic timescale of ~ 7 days, over a period of ~ 60 days. The net displacement of the glacier-dome contact over this period of time is ~ 7 m, which is in good agreement with observations that suggest ≤ 5 m of motion. Observations suggest that $D=550$ m, but we find computationally that mass conservation requires D to be closer to 650 m. That is, with $D=550$ m, not enough mass converges on the glacier centerline near $x=600$ m to build the observed surface bulge (this finding is independent of the sensitivity tests discussed below). We discuss the possible reasons for this discrepancy below.

Other observational constraints

We use DEM-derived surface-elevation profiles (Figure 5.3) as primary targets for flow modeling that steps forward in time. Surface elevation has an uncertainty of a few decimeters (Walder and others, in press) except where the glacier is highly fractured--meaning the uppermost 200 to 300 m long reach of the glacier—and we

do not attempt to match the surface elevations there. As a secondary check, we compare modeled and measured surface velocities on the glacier during the squeezing event. Surface velocities were derived from GPS-measured positions of stations deployed on the glacier surface. The helicopter-deployed GPS stations were designed for volcano monitoring during the eruption (LaHusen, in press) and were available for glacier monitoring only sporadically. Fortuitously, the record at one station encompassed the period of time during which squeezing of the glacier slowed and ultimately stopped.

RESULTS

We explored the sensitivity of modeled surface elevation and velocity fields to choices for bulk density ρ and scalar enhancement factor E . Bulk density obviously depends upon debris content, and it seems likely that E does too, with E decreasing as rock content increases. Our goal is not to fit observations exactly: capturing all of the observed surface detail would require an impractical number of grid cells and/or excessive tuning of the model. Instead, we aim to constrain the most reasonable values for E and ρ based on the overall trends in the misfit between the model and the observations. We tested the model for $0.01 \leq E \leq 1$ and $918 \leq \rho \leq 1700$ (kg m^{-3}) (representing debris content ranging from 0 to ~50% by volume). While we present only a subset of all model results, additional results support the main points discussed below.

Misfit between the modeled and observed surface elevations for a density of 1100 kg m^{-3} and enhancement factors of 1, 0.2, and 0.05 is shown in Figure 5.4. Note that $\rho=1100 \text{ kg m}^{-3}$ corresponds to about 15% rock debris by volume—the value estimated for the glacier as defined with the bed taken as the 1986 crater floor. While the misfit for all models is similar for the first ~50 days, clear trends emerge by day 107: models with $E=1$ lead to a mass deficit in upstream regions and a mass surplus in downstream regions, while models with $E=0.05$ show the

opposite trend. For $E=0.2$, the maximum misfit generally falls within ± 10 m throughout the model run. When comparing modeled and measured surface velocities at ELE4 for the same simulations (Figure 5.5), the reason for trends in surface-elevation misfit in Figure 5.4 becomes obvious. For $E=1$, horizontal velocities in the region of squeezing are too large and ice moves from the “bulge” towards the terminus too quickly. Conversely, for $E=0.05$, velocities in the region of squeezing are too small and too much ice remains in the upper portion of the glacier after the squeezing stops. The model with $E=0.2$ provides a good fit to the velocity at ELE4, and thus we adopt the case $\rho=1100 \text{ kg m}^{-3}$, $E=0.2$ as a benchmark for further discussion. The “decay” in the horizontal velocity over time, which is shown by all models, is a reflection of the decay in the squeezing rate.

Consider next the effect of varying ρ . With $E=0.2$, surface-elevation misfit (Figure 5.4) for $\rho=918 \text{ kg m}^{-3}$ (pure ice) and $\rho=1400 \text{ kg m}^{-3}$ (30% rock debris by volume) is worse than for a density of 1100 kg m^{-3} , but still generally falls within the range of ± 10 m. The same variation in density yields an acceptable fit between measured and modeled surface velocity (Figure 5.5).

While the end-member models tested here - stiff, “heavy” ice ($E=0.05$ and $\rho=1400 \text{ kg m}^{-3}$; dashed line “c” in Figure 5.6) and soft, “light” ice ($E=1$ and $\rho=918 \text{ kg m}^{-3}$; dotted line “a” in Figure 5.6) - result in a fit to the observations that is worse than our favored model, they highlight an important tradeoff between density and enhancement. The observations can be fit by assuming stiff, dense ice *or* by assuming soft, less dense ice because a similar velocity field (not shown) results in either case. If there were no constraint on density other than a lower bound (the density of pure ice), we would find that observations could be fit equally well by assuming combinations of enhancement factor and density ranging from 0.1-0.5 and 918-1700 kg m^{-3} , respectively. In fact, we do we have an independent constraint on bulk density and can therefore use the sensitivity tests to narrow the range of uncertainty in the enhancement factor. Our best estimate for density, as noted above, is 1100 kg m^{-3} , corresponding to about 15% rock debris by volume; the upper bound is $\rho=1400 \text{ kg m}^{-3}$, corresponding to about 30% rock debris by

volume—the average debris content of *all* the crater-floor fill accumulated since 1980. If the density were 1400 kg m^{-3} , the enhancement factor would have to be close to 0.1 to match surface elevation and velocity as closely as our benchmark case ($\rho=1100 \text{ kg m}^{-3}$, $E=0.2$).

Observed and computed surface profiles on several dates are shown in Figure 5.7 for our benchmark case and for the case of pure glacier ice with no enhancement ($E=1$). The pure-ice case gives a surface-elevation profile with a systematic error—too low in the upper reach and too high in the lower reach—that worsens with time.

To explain why the downstream portion of the east glacier remains largely stagnant during the squeezing event while the upstream portion undergoes dramatic changes, Walder and others suggested that ice in the downstream portion of the glacier, which was not squeezed, acted as a “dam” against the ice upstream. We augment their qualitative discussion by using the model to understand quantitatively why a dam would form. In Figure 5.8 we show the horizontal velocity, horizontal-strain rate, and horizontal deviatoric stress from the model on day 50 (21 February 2005), for our benchmark model values. The horizontal axis in Figure 5.8 is approximately centered at the transition from very rapid to no lateral squeezing. Moreover, there is an abrupt decrease in flowband width just downstream of this location, where the east glacier passes through a narrow gap between the 1980-86 lava dome and the east crater wall (Figure 5.1). According to the model, this combination of factors results in highly compressive longitudinal-strain rates and corresponding highly compressive longitudinal stresses. This, in turn, leads to a large, negative, stress *gradient* across this width transition, and for several hundred meters downstream, which results in a force pushing back upstream, resisting the ice flow. In reality, the transition from a narrowing to a steady flowband width may be more gradual than shown here, in which case the overall effect on the strain and stress fields, while less dramatic than shown in Figure 5.8, would be the same.

DISCUSSION

If flow of the debris-laden east crater glacier at Mount St. Helens is properly characterized by Glen's flow law with $n = 3$, then the ice must be much stiffer than debris-free ice, by a factor of 5 to 10, with the stiffness increasing as the rock-debris content rises. This inference from modeling contrasts with discussion of Jacka and others (2003), who reviewed laboratory data and concluded that there is no dependence between deformation rate and debris (sand) content for debris fractions up to 15% by volume. (For sand/silt fractions in excess of 50%, there does seem to be a clear correlation between stiffness and debris content (Mangold and others, 2002).) We speculate that the difference between our conclusion and that of Jacka and others reflects the radical difference between a laboratory experiment and the natural "ice-squeezing" experiment performed by the Mount St. Helens lava dome, and in particular the associated scale effects. In the laboratory, because the grain size of the ice is likely to be comparable to the grain size of the debris, the presence of thin water films at ice/debris interfaces probably facilitates regelation and other deformation mechanisms. Rock debris within the crater glacier, in contrast, spans the grain-size range from silt to boulders, with the grain size of the particulate material commonly much greater than that of the ice; deformation mechanisms that may be effective at laboratory scale may play little role at field scale.

A worrisome note about our results is that matching evolution of the surface shape required that the length of glacier being squeezed within the model to be 100 m longer than suggested by observations. One possible reason for this discrepancy is that the region of squeezing needs to be slightly longer in the model to correct for three-dimensional effects not captured in our two-dimensional model. We assume a very simple flowband geometry in both the region being squeezed and in the region for which the glacier width does not change over time. In reality, both the glacier width and the squeezing rate vary along flow. Our need to adjust the length of the

squeeze zone may reflect our over simplified parameterization of spatial variability of squeezing rate. Another, more speculative possibility is that matching the observed surface elevation profiles does in fact require mass convergence additional to that implied by surface observations of the motion of the dome-glacier contact: for example, magma may have intruded beneath the west margin of the glacier or beneath the glacier itself, slightly downstream from the new lava dome.

By simplifying a three-dimensional flow problem to a two-dimensional flow problem, we have likely missed some details governing the deformation of east crater glacier during growth of the new lava dome. Nevertheless, it is satisfying that the simple approach taken here leads to a good fit to the observations with only a minor amount of model “tuning”. Without the use of a higher-order flow model, this would likely not be the case. Thickening of the upper glacier during growth of the new dome is a straightforward consequence of continuity but the redistribution of this thickened ice is strongly dependent on longitudinal stresses.

CONCLUSIONS

Flow modeling constrained by surface velocity data and independent estimates for glacier bulk density demonstrates that the east crater glacier is significantly stiffer than debris-free glacier ice. Our favored model, in which the ice contains ~15% rock debris by volume, requires a flow-enhancement factor of 0.2 (that is, ice stiffer than normal by a factor of 5) to fit the data. If the ice contains 30% rock debris by volume (the upper bound), an enhancement factor of 0.1 (that is, ice stiffer than normal by a factor of 10) is indicated. The model further makes manifest the existence of strong longitudinal stress gradients in the glacier while it was being squeezed by the growing lava dome.

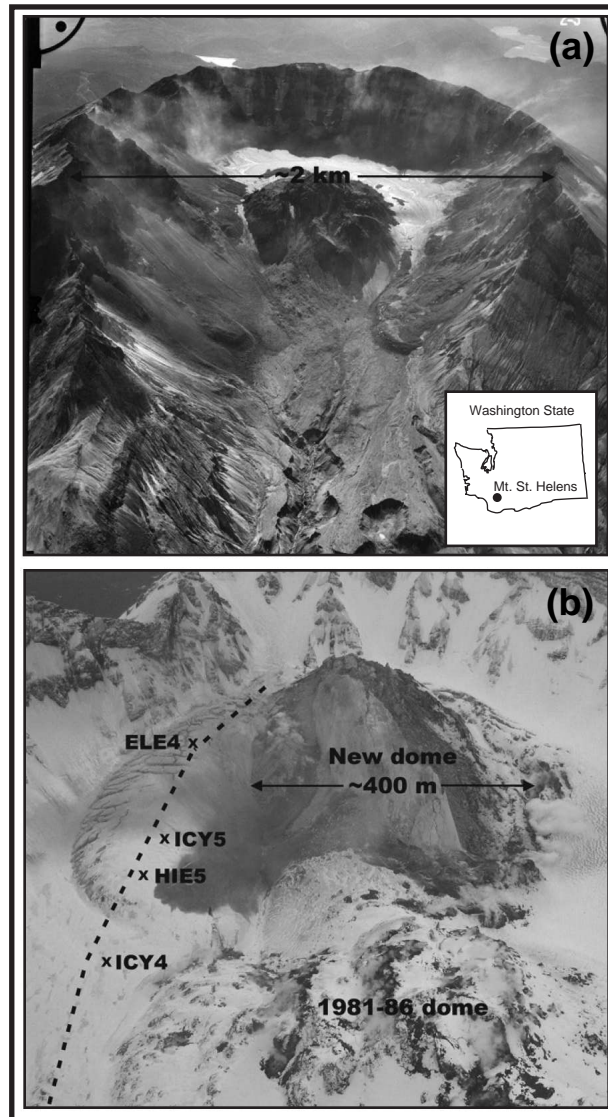


Figure 5.1: Field setting of Mount St. Helens crater glacier. (a) Mount St. Helens in October of 2000, looking south. The crater glacier is partially obscured on the east side of the 1980-86 lava dome by rock-fall debris, and on the west side merges with a rock glacier shed from the crater wall. Photo by S.P. Schilling, USGS. (b) The crater of Mount St. Helens crater on 10 April 2005. View to the south. The dashed line is the approximate centerline of the east crater glacier. Locations of GPS stations are marked with an “x”. Photo by J.J. Major, USGS.

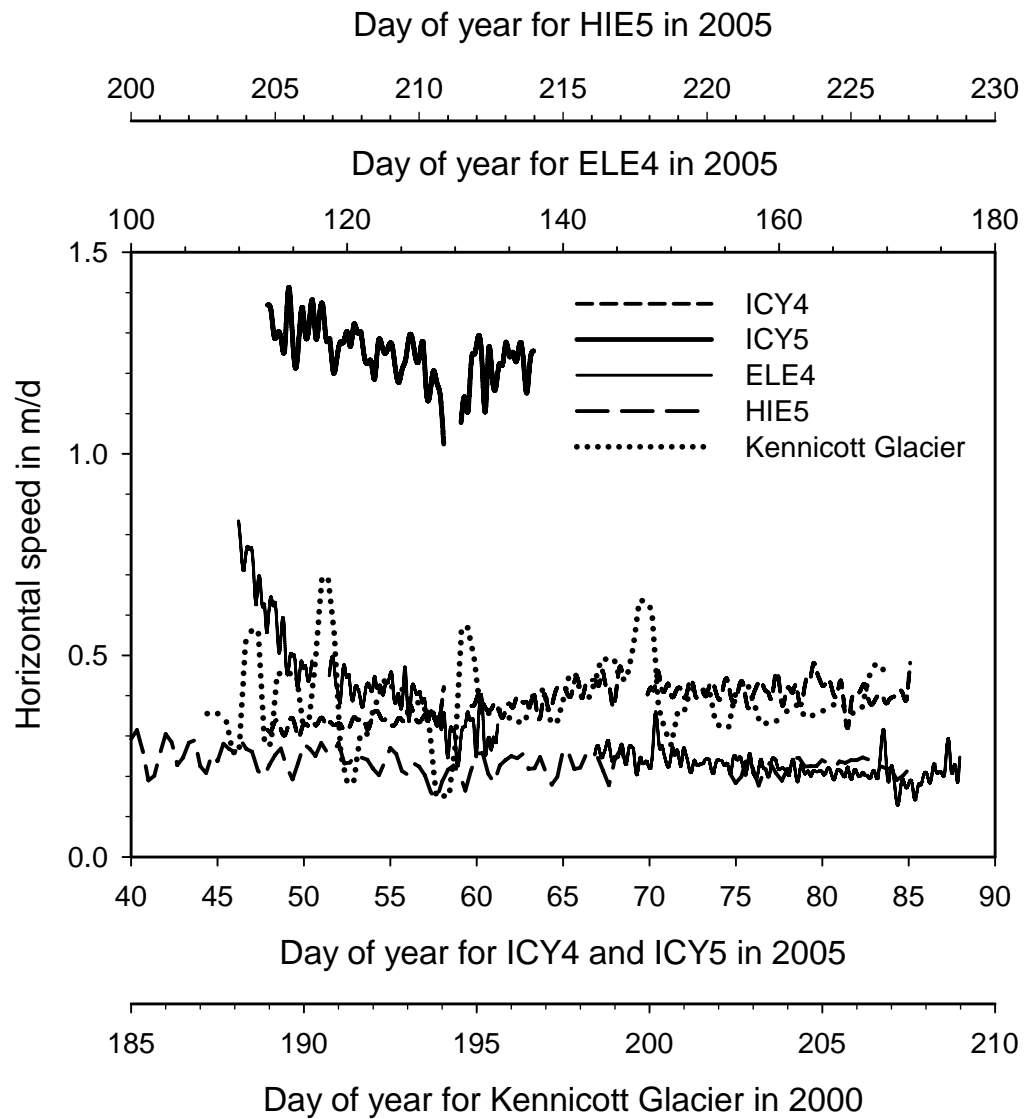


Figure 5.2: Horizontal speed of east crater glacier GPS stations. ICY4 and ICY5 were on the glacier while the lava-dome spine was expanding eastward. ELE4 was fortuitously placed on the glacier about the time that the spine stopped growing. HIE5 was on the glacier in mid-summer. Azimuth of motion for all stations was within 180° of north. For comparison we show surface-speed data (adapted from Anderson and others (2005)) for a target on Kennicott Glacier, a temperate valley glacier in Alaska, during the year 2000. The record for Kennicott Glacier shows large amplitude, commonly diurnal fluctuations not seen at the east crater glacier.

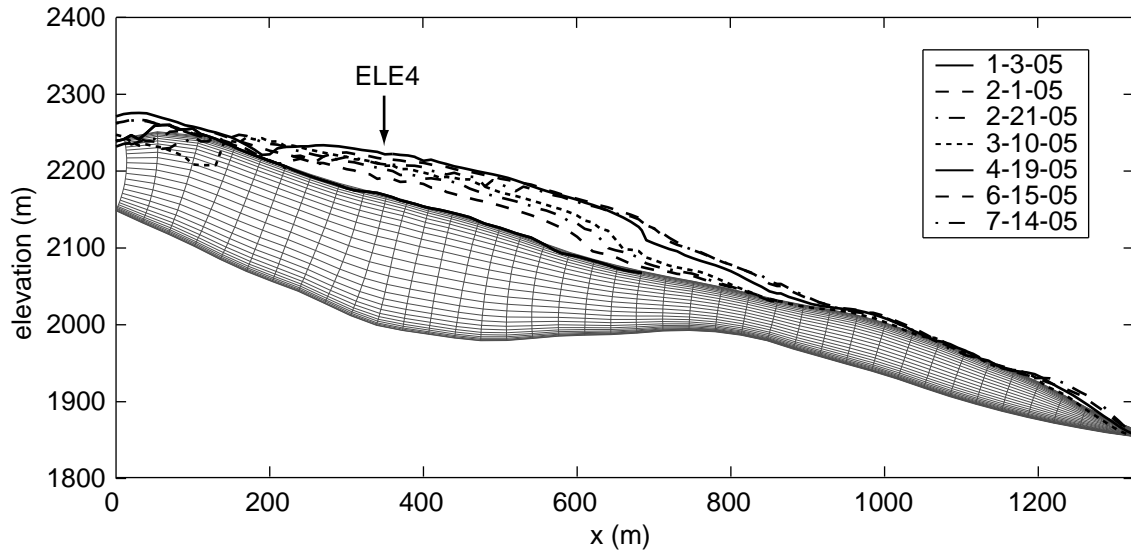
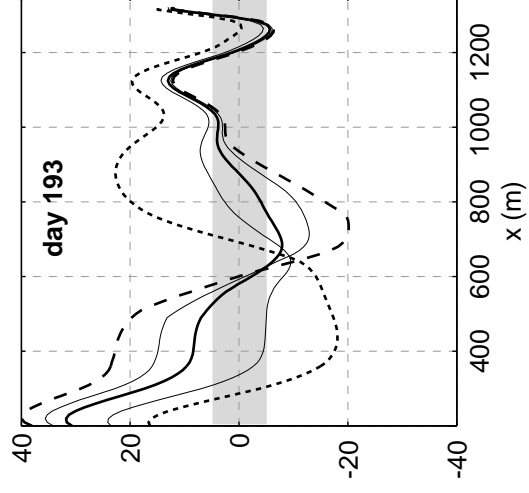
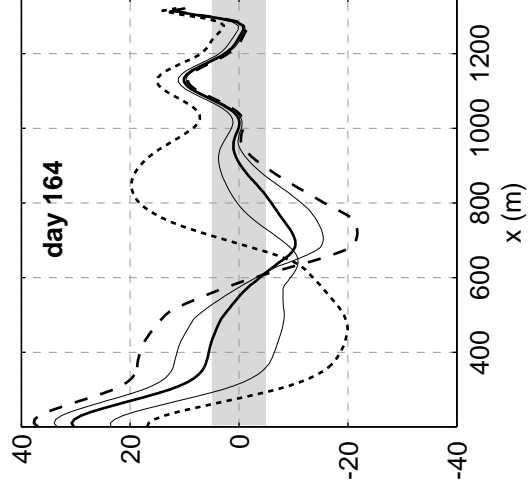
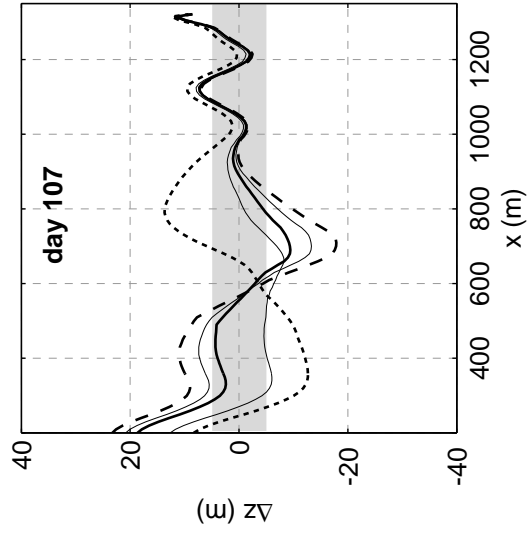
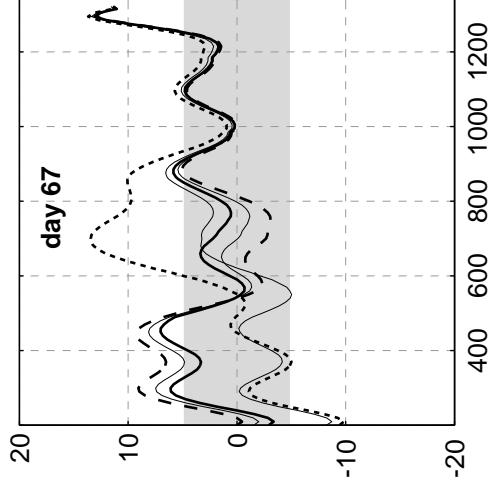
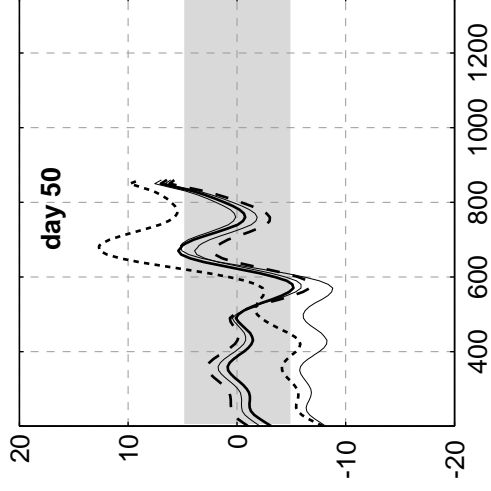
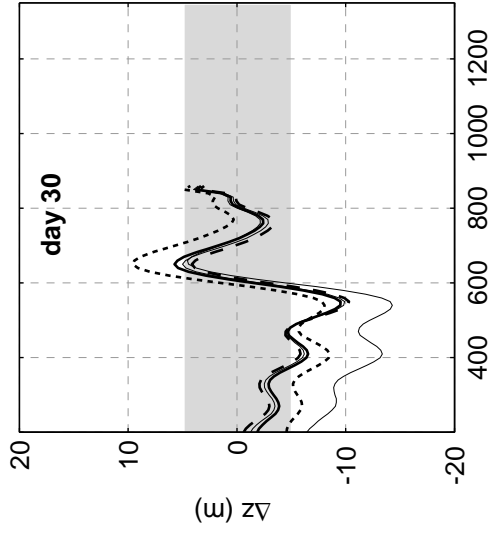


Figure 5.3. Surface elevation profiles along the glacier centerline in Figure 5.1. Line types denote the centerline elevation at various dates during the squeezing event. The fine lines represent the initial FVM grid. The approximate location of the velocity measurement station ELE4 is labeled.

Figure 5.4: Misfit between modeled and observed elevations ($\text{misfit} = \text{elevation}_{\text{model}} - \text{elevation}_{\text{obs}}$) along the glacier surface for $\rho = 1100 \text{ kg m}^{-3}$ and $E = 0.2$ (solid line), $E = 0.05$ (dashed line), and $E = 1$ (dotted line). Thin, solid lines represent results for $E = 0.2$ and $\rho = 918 \text{ kg m}^{-3}$ and $\rho = 1400 \text{ kg m}^{-3}$. The gray-shaded region encompasses an elevation misfit of $\pm 5 \text{ m}$.



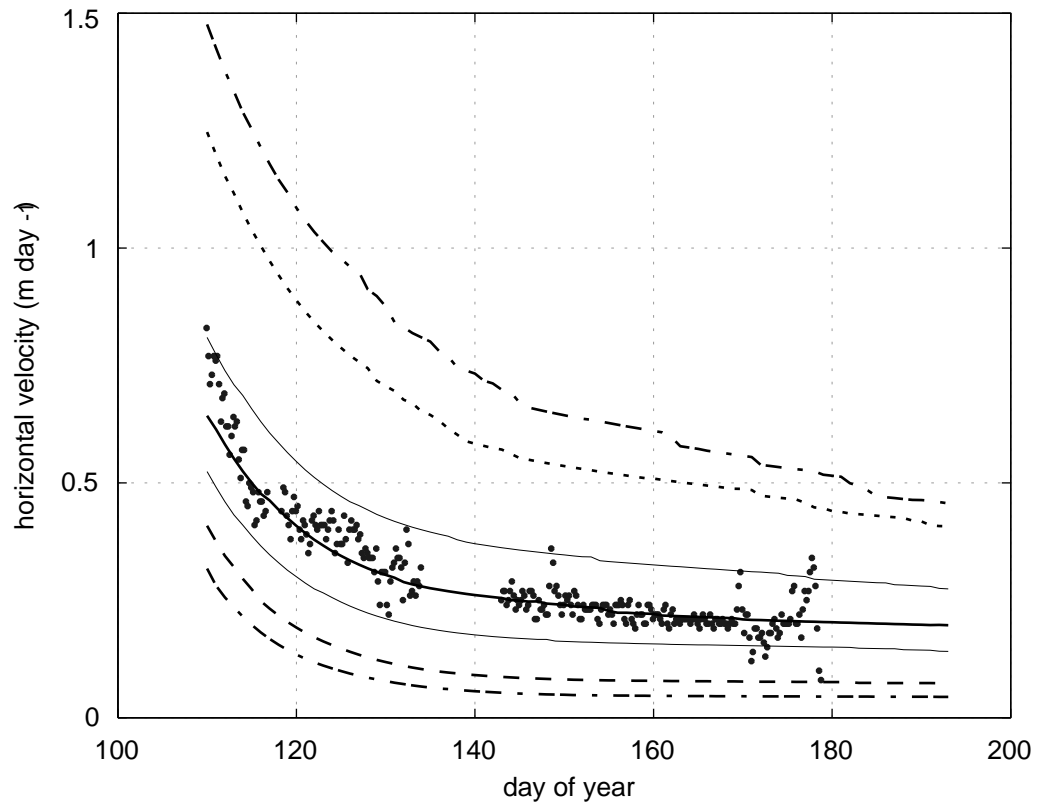


Figure 5.5: Model fit to observed horizontal velocities at ELE4. Gray dots are observations from Walder and others. Solid, dashed, and dotted lines are as in Figure 5.4. The lower dash-dash-dot line is for the end member of stiff, low-density ice ($E=0.05$ and $\rho=918 \text{ kg m}^{-3}$) and the upper dash-dash-dot line is for the end member of soft, high-density ice ($E=1$ and $\rho=1400 \text{ kg m}^{-3}$).

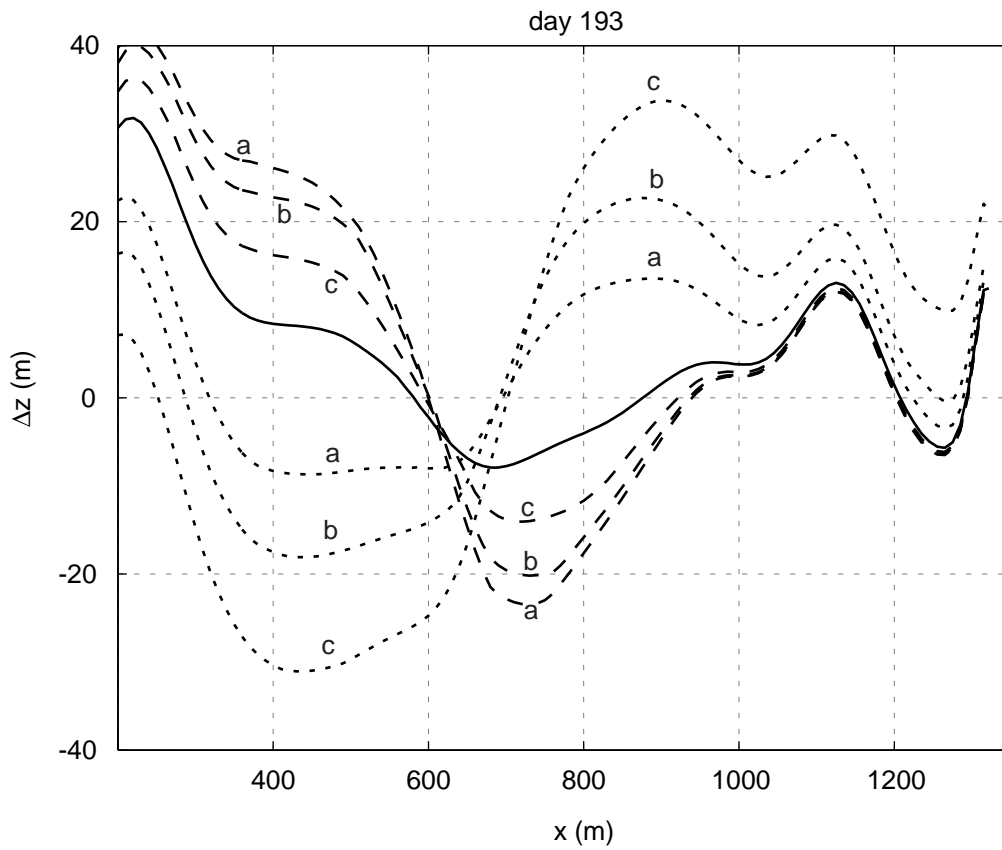


Figure 5.6. Misfit between modeled and observed elevations on day 193. Line types represent model results for relatively stiff ($E=0.05$, dashed) and relatively soft ($E=1$, dotted) ice and for densities of $\rho=918$ (a), 1100 (b), and 1400 (c) kg m^{-3} . The black solid line shows the misfit for the benchmark values of density and enhancement.

Figure 5.7: Model fit to observed surface elevations. Modeled and observed surface elevations are shown by the thin, solid lines and open circles, respectively. The model results shown are for $\rho=1100 \text{ kg m}^{-3}$ and $E=0.2$. For reference, modeled surface elevations using “normal” ice values of $\rho=918 \text{ kg m}^{-3}$ and $E=1$ are shown by dashed lines. The dotted line represents the initial surface elevation profile at the beginning of January 2005.

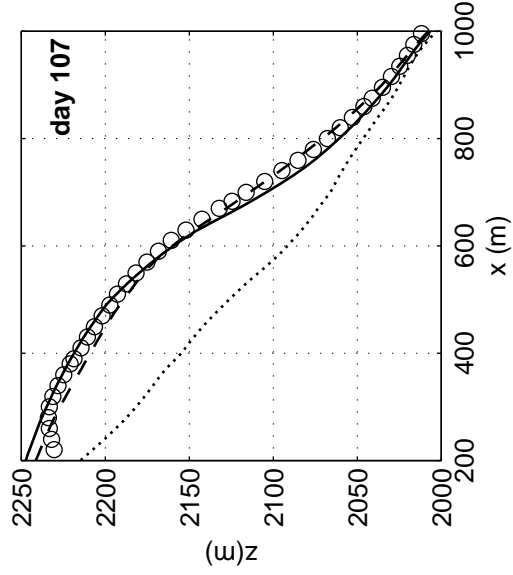
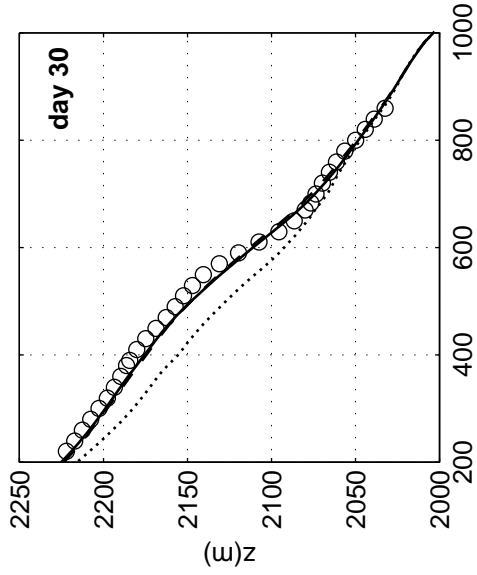
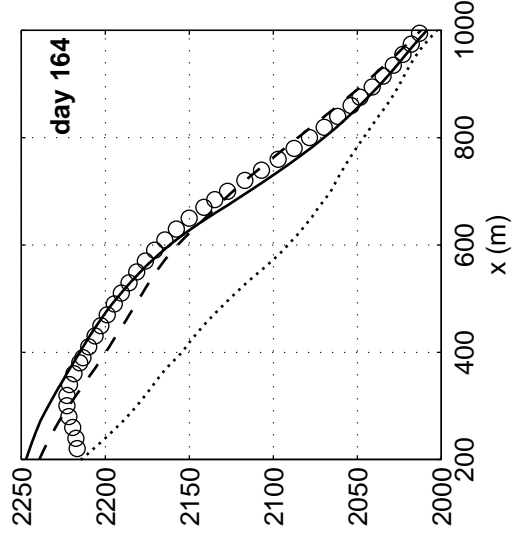
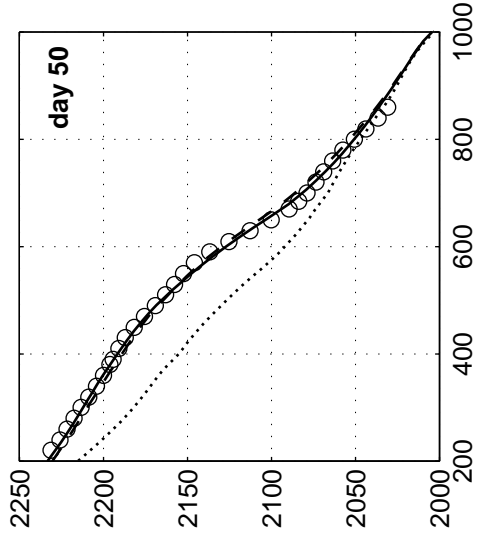
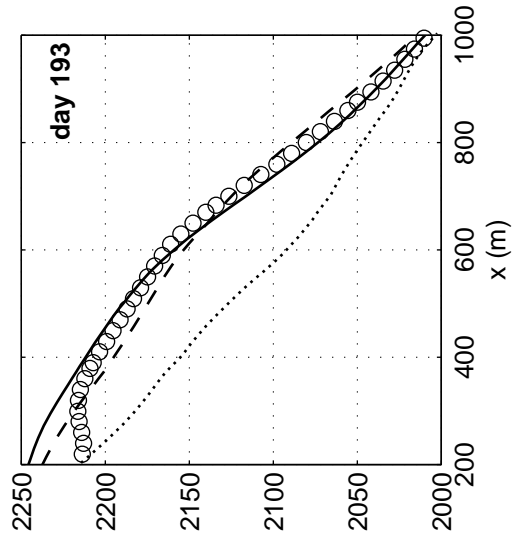
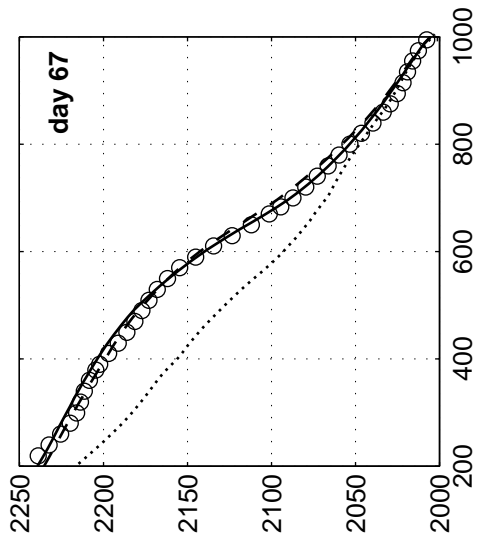
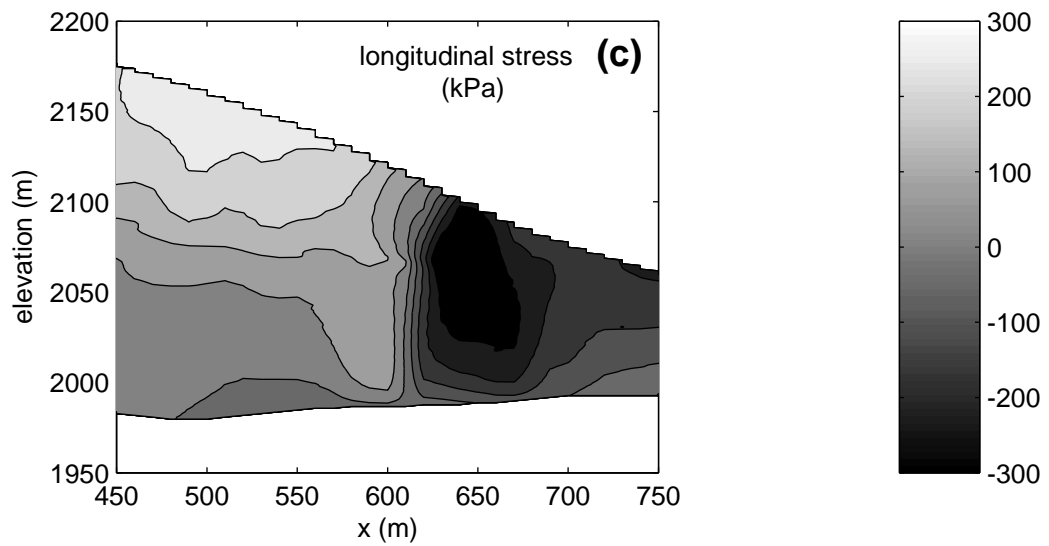
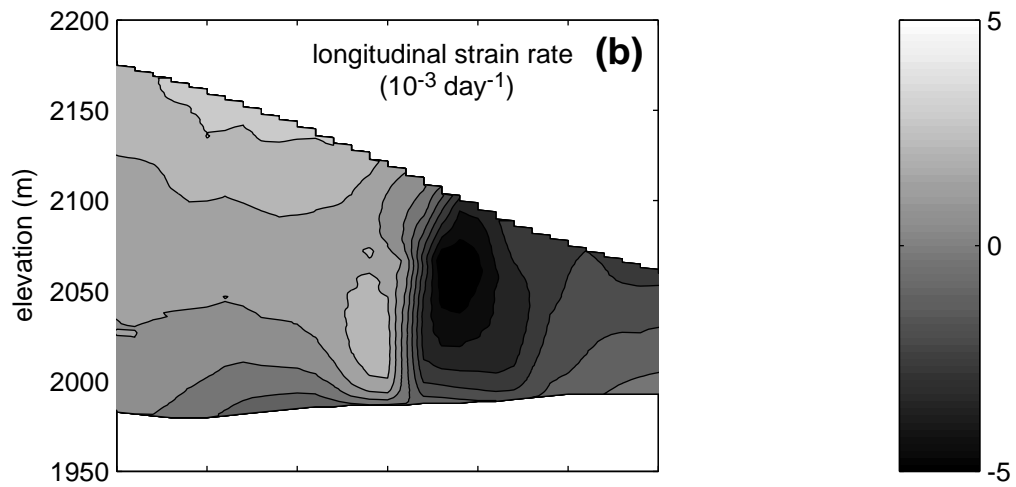
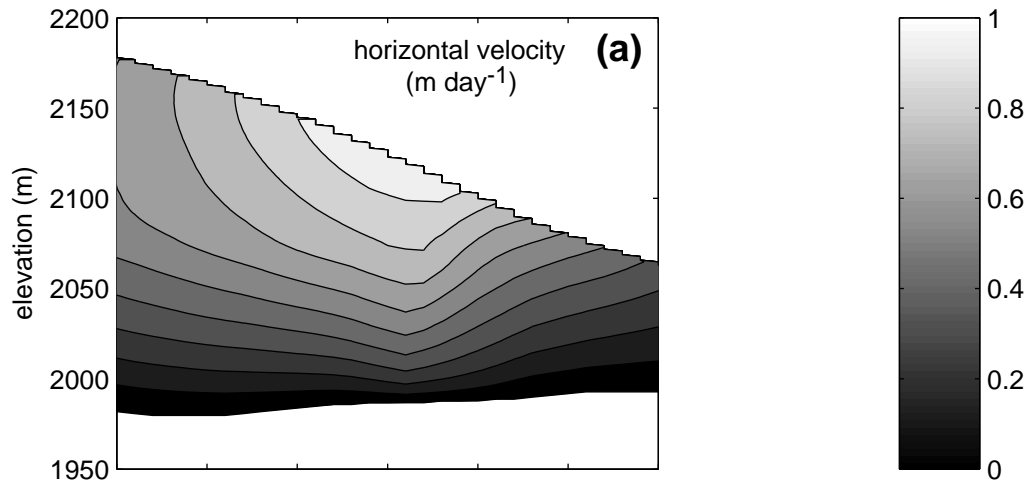


Figure 5.8: Horizontal velocity, strain rate, and stress on day 50 (21, February 2005). (a) Horizontal velocity [contour interval = 0.1 m day^{-1}], (b) longitudinal-strain rate [contour interval = 10^{-3} day^{-1}], and (c) longitudinal-deviatoric stress. [contour interval = 60 kPa] The downstream limit of squeezing is at $x \sim 650 \text{ m}$.



REFERENCES

- Ackert, R.P., D.J. Barclay, H.W. Borns, P.E. Calkin, M.D. Kurz, J.L. Fastook, and E.J. Steig. 1999. Measurements of past ice sheet elevations in interior West Antarctica. *Science*, **286**(5438), 276-280.
- Alley, R.B., P.U. Clark, P. Huybrechts, and I. Jougin. 2005. Ice-Sheet and sea-level changes. *Science*, **310**(5747), 456-460.
- Anderson, J.B., S.S. Shipp, A.L. Lowe, J.S. Wellner, and A.B. Mosola. 2002. The Antarctic ice sheet during the last glacial maximum and its subsequent retreat history: a review. *Quat. Sci. Rev.* **21**, p. 49-70.
- Anderson, R.S., J.S. Walder, S.P. Anderson, D.C. Trabant, and A.G. Fountain. 2005. The dynamic response of Kennicott Glacier to the Hidden Creek Lake outburst flood. *Ann. Glaciol.*, **40**, 237-242.
- Bindschadler, R.A. 1997. Actively surging West Antarctic ice streams and their response characteristics. *Ann. Glaciol.*, **24**, 409-414.
- Bindschadler, R.A. 1998. Future of the West Antarctic Ice Sheet. *Science*, **282**(5388), 428-429.
- Brook, E.J., J.W.C. White, A.S.M. Schilla, M.L. Bender, B. Barnett, J.P. Severinghaus, K.C. Taylor, R.B. Alley, E.J. Steig. 2005. Timing of millennial-scale climate change at Siple Dome, West Antarctica, during the last glacial period. *Quat. Sci. Rev.* **24**, 1333-1343.
- Budd, W.F. 1970a. The longitudinal stress and strain-rate gradients in ice masses. *J. Glaciol.* **9**, 19-27.
- Budd, W.F. 1970b. Ice flow over bedrock perturbations. *J. Glaciol.* **9**, 29-48.

- Conway, H., B.L. Hall, G.H. Denton, A.M. Gades and E.D. Waddington. 1999. Past and future grounding-line retreat of the West Antarctic Ice Sheet. *Science*, **286** (5438), 280-283.
- Cuffey, K.M., R.B. Alley, P.B. Grootes, J.M. Bolzan, and S. Anandakrishnan. 1994. Calibration of the $\delta^{18}\text{O}$ isotopic paleothermometer for central Greenland, using borehole temperatures. *J. Glaciol.*, **40**(135), 341-349.
- Dahl-Jensen, D. 1989. Steady Thermomechanical Flow along two-dimensional flow lines in large grounded ice sheets. *J. Geophys. Res.*, **94**(B8), 10355-10362.
- Denton, G.H., Prentice, M.L., Burckle, L.H., 1991. Cainozoic history of the Antarctic Ice Sheet. In: Tingey, R.J. (Ed.), *The Geology of Antarctica*. Clarendon Press, Oxford, England, pp. 365-433.
- Denton, G.H., T.J. Hughes. 2002. Reconstructing the Antarctic Ice Sheet at the Last Glacial Maximum. *Quat. Sci. Rev.*, **21**, 193-202.
- DiPrinzio, C.L., L.A. Wilen, R.B. Alley, J.J. Fitzpatrick, M.K. Spencer, and A.J. Gow. 2005. Fabric and texture at Siple Dome, Antarctica. *J. Glaciol.*, **51**(173), 281-290.
- Dzurisin, D., J.W. Vallance, T.M. Gerlach, S.C. Moran, and S.D. Malone. 2005. Mount St. Helens reawakens. *Eos (Trans., Am. Geophys. Union)*, **86**(3), 25 & 29.
- Eiseman, P.R. 1982. Orthogonal Grid Generation. In Thompson, J.F., ed., *Numerical Grid Generation*, Elsevier Science Pub. Co., Inc., New York, 193-233.
- Engelhardt, H. 2004. Ice temperature and high geothermal flux at Siple Dome, West Antarctica, from borehole measurements. *J. Glaciol.*, **50**(169), 251-256.
- Fairbanks, R.D. 1989. A 17,000-year glacio-eustatic sea level record: influence of glacial melting rates on the Younger Dryas event and deep-ocean circulation. *Nature*, **232**(637), 637-742.

- Fisher, D.A., R.M. Koerner, W.S.B. Patterson, W. Dansgaard, N. Gundestrup, and N. Reeh. 1983. Effect of wind scouring on climate records from ice-core oxygen-isotope profiles. *Nature*, **301**(5897), 205-209.
- Fowler, A.C. and D.A. Larson. 1978. On the flow of polythermal glaciers I. Model and preliminary analysis. *Proc. R. Soc. London, Ser. A.* **363**, 217-242.
- Fujita, S., H. Maeno, S. Uratsuka, S. T. Furukawa, S. Mae, Y. Fujii, and O. Watanabe. 1999. Nature of radio echo layering in the Antarctic ice sheet detected by a two-frequency experiment *J. Geophys. Res.* **104**, B6 , p. 13,013 (1999JB900034)
- Gray, L., I. Joughin, S. Tulaczyk, V. B. Spikes, R. Bindshadler, and K. Jezek. 2005. Evidence for subglacial water transport in the West Antarctica Ice Sheet through three-dimensional satellite radar interferometry. *Geophys. Res. Lett.*, **32**, L03501, doi:10.1029/2004GL021387.
- Grootes, P. M., and M. Stuiver. 1986. Ross ice shelf oxygen isotopes and West Antarctic ice sheet history. *Quat. Res.*, **40**, 70-80.
- Hamilton, G.S. 2002. Mass balance and accumulation rate across Siple Dome, West Antarctica. *Ann. Glaciol.*, **35**, 102-106.
- Hawley, R.L., E.D. Waddington, G.W. Lamorey and K.C. Taylor. 2004. Vertical-strain measurements in firn at Siple Dome, Antarctica. *J. Glaciol.*, **50**(170), 447-452.
- Hooke, R. 1998. *Principles of Glacier Mechanics*. Prentice Hall, New Jersey.
- Hutter, K. 1981. The effect of longitudinal stress on the shear stress of an ice sheet: in defense of using stretched co-ordinates. *J. Glaciol.*, **27**, 39-56.
- Hutter, K. 1983. *Theoretical glaciology; Material science of ice and the mechanics of glaciers and ice sheets*. D. Reidel Publishing Company/Tokyo, Terra

Scientific Publishing Company.

- Hvidberg, C. 1996. Steady-state thermomechanical modeling of ice flow near the centre of large ice sheets with the finite-element method. *Ann. Glaciol.*, **23**, 116-123.
- Jacka, T.H., S. Donoghue, J. Li, W.F. Budd, and R.M. Anderson. 2003. Laboratory studies of the flow rates of debris-laden ice. *Ann. Glaciol.*, **37**, 108-112.
- Jacobel R. W., Scambos, T. A., Nereson, N. A., and Raymond, C. F. 2000. Changes in the margin of Ice Stream C, Antarctica. *J. Glaciol.* **46**(152), 102-110.
- Jacobel R.W., T.A. Scambos, C.F. Raymond and A.M. Gades, 1996. Changes in the configuration of ice stream flow from the West Antarctic ice sheet. *J. Geophys. Res.* **101**(B3), 5499-5504.
- Jenssen, D. 1983. Elevation and climatic changes from total gas content and stable isotopic measurements. In G.d.Q. Robin: *The climatic record in polar ice sheets*. 138-144.
- Joughin, I., E. Rignot, C.E. Rosanova, B.K. Lucchitta, and J. Bohlander, 2003. Timing of recent accelerations of Pine Island Glacier, Antarctica. *Geophys. Res. Letters*, **30**(13), 1706, doi:10.1029/2003GL017609.
- Joughin, I., W. Abdalati, and M. Fahnestock. 2004. Large fluctuations in speed on Greenland's Jakobshavn Isbrae glacier. *Nature*. **432**(7017), 608-610.
- Jouzel, J., F. Vimeux, N. Caillon, G. Delaygue, G. Hoffmann, V. Masson-Delmotte, and F. Parrenin. 2003. Magnitude of isotope/temperature scaling for interpretation of central Antarctic ice cores. *JGR*, **108**(D12), 4361, doi:10.1029/2002JD002677, 2003
- Jun, L., T.H. Jacka, and W.F. Budd. 1996. Deformation rates in combined compression and shear for ice which is initially isotropic and after the development of strong anisotropy. *Ann. Glaciol.*, **23**, 247-252.

- Kamb, B. 1991. Rheological Nonlinearity and Flow Instability in the Deforming Bed Mechanism of Ice Stream Motion. *J. Geophys. Res.*, **96**(B10), 16585-16595.
- Kamb, B., Raymond, C.F., Harrison, W.D., Engelhardt, H., Echelmeyer, K.A., Humprey, N., Brugman, M.M., and Pfeffer, T. 1985. Glacier surge mechanism: 1982-1983 surge of Variegated Glacier, Alaska. *Science*, **227**(4686), 469-479.
- Kavanaugh, J.L. and K.M. Cuffey. 2003. Space and time variation of $\delta^{18}\text{O}$ in Antarctic precipitation revisited. *Global Biogeochemical Cycles*, **17**(1), 1017, doi:10.1029/2002GB001910, 2003
- LaHusen, R.G. GPS..... in Sherrod, D.A, and Scott, W.E., eds., *A volcano rekindled: the first year of renewed eruption at Mount St. Helens, 2004-05: U.S. Geol. Surv. Prof. Paper.*
- Licht, K.J. 2004. The Ross Sea's contribution to eustatic sea level during meltwater pulse 1A. *Sedimentary Geology*, **165**, 343-353.
- Mangold, N., P. Allemand, P. Duval, Y. Geraud, and P. Thomas, 2002. Experimental and theoretical deformation of ice-rock mixtures: Implications on rheology and ice content of Martian permafrost. *Planet. Space Sci.*, **50**, 385-401.
- Martín, C., Hindmarsh, R.C., Navarro, A., and Francisco J. 2006. Dating ice flow change near the flow divide at Roosevelt Island, Antarctica, by using a thermomechanical model to to predict radar stratigraphy. *J. Geophys. Res.*, **111**(F1), F01011.
- Mills, H.H. 1992. Post-eruption erosion and deposition in the 1980 crater of Mount St Helens, Washington, determined from digital maps. *Earth Surf. Proc. Landforms*, **17**(8), 739-754.
- Nereson, N.A. 1998. The flow history of SDM and Ice Streams C and D, West Antarctica: Inferences from geophysical measurements and ice flow models. Ph.D. thesis, University of Washington.

- Nereson, N.A. and E.D. Waddington. 2002. Isochrons and Isotherms Beneath Migrating Ice Divides. *J. Glaciol.*, **48**(160), 95-108.
- Nereson, N.A., R.C.A. Hindmarsh, and C.F. Raymond. 1998a. Sensitivity of the divide position at Siple Dome, West Antarctica, to boundary forcing. *Ann. Glaciol.*, **27**, 207-214.
- Nereson, N.A., C.F. Raymond, E.D. Waddington and R.W. Jacobel. 1998b. Migration of the Siple Dome Ice Divide, West Antarctica. *J. Glaciol.*, **44**(148), 643-652.
- Nereson, N.A., C.F. Raymond, R.W. Jacobel and E.D. Waddington. 2000. The accumulation pattern across Siple Dome, West Antarctica, inferred from radar-detected internal layers. *J. Glaciol.*, **46**(152), 75-86.
- Nye, J.F. 1957. The distribution of stress and velocity in glaciers and ice sheets. *Proceedings of the Royal Society of London, Series A*, **239**, 113-133.
- Nye, J.F. 1965. The flow of a glacier in a channel of rectangular, elliptic, or parabolic cross-section. *J. Glaciol.*, **5**(41), 661-690.
- Parizek, B.R., R.B. Alley, and C.L. Hulbe. 2003. Subglacial thermal balance permits ongoing grounding line retreat along the Siple Coast of West Antarctica. *Ann. Glaciol.* **36**, 251-256.
- Patankar, S.V. 1980. *Numerical Heat Transfer and Fluid Flow*. Hemisphere Publishing Corp., New York.
- Paterson, W.S.B. 1994. *The Physics of Glaciers*. Oxford, Elsevier Science Ltd., 110-114.
- Paterson, W.S.B., and E.D. Waddington. 1986. Estimated basal temperatures at Crete, Greenland, throughout a glacial cycle. *Cold Regions Science and Technology*, **12**, 99-102.

- Pattyn, F. 2002. Transient glacier response with a higher-order numerical ice-flow model. *J. Glaciol.*, **48**(162), 467-477.
- Payne, A.J., A. Vieli, A.P. Shepherd, D.J. Wingham, and E. Rignot. 2004. Recent dramatic thinning of largest West Antarctic ice stream triggered by oceans. *Geophys. Res. Lett.*, **31**, L23401.
- Pettit, E.C. 2003. Unique Dynamic Behaviors of Ice Divides: Siple Dome and the Rheological Properties of Ice. Ph.D. thesis, University of Washington.
- Pettit, E.C., H.P. Jacobson, and E.D. Waddington. 2003. Effects of basal sliding on isochrones near an ice divide. *Ann. Glaciol.*, **37**, 370-376.
- Price, S.F. and I.M. Whillans. 2001. Crevasse patterns at the onset to Ice Stream B, West Antarctica. *J. Glaciol.*, **47**(156), 29-36.
- Price, S.F., H. Conway, E.D. Waddington, and R.A. Bindschadler. Investigating feedbacks between basal sliding, frictional melting, and longitudinal-stress transmission. (abstract) AGU Fall Meeting, San Francisco, CA, Dec. 28, 2005.
- Price, S.F., R.A. Bindschadler, C.L. Hulbe, and D.D. Blankenship. 2002. Force balance along an inland tributary and onset to Ice Stream D, West Antarctica. *J. Glaciol.* **48**(160), 20-30.
- Rathbun A., C. Marone, S. Anandakrishnan, R. Alley. 2005. Laboratory Study of Till Rheology. (abstract) WAIS Workshop, Algonkian State Park, Sterling, VA, Sept. 28-Oct. 1, 2005.
- Raymond, C.F. 1983. Deformation in the vicinity of divides. *J. Glaciol.*, **34**(117), 357-373.
- Raymond, C.F. 2000. Energy balance of ice streams. *J. Glaciol.*, **46**(155), 665-674.

- Raymond, C.F., N. Nereson, A. Gades, H. Conway, R. Jacobel, and T. Scambos. 1995. Geometry and stratigraphy of Siple Dome, Antarctica. *Antarct. J. U.S., 1995 Review*, **30**(5), 91-93.
- Raynaud D. and I. M. Whillans. 1982. Air content of the Byrd core and past changes in the West Antarctic Ice Sheet. *Ann. Glaciol.* **3**, 269-273.
- Raynaud, D. and B. Lebel. 1979. Total Gas Content and Surface Elevation of Polar Ice Sheets. *Nature* **281**(5729), 289-291.
- Rignot, E. 2002. Ice-shelf changes in Pine Island Bay, Antarctica. *J. Glaciol.*, **48**, 247-256.
- Scambos, T.A., J.A. Bohlander, C.A. Shuman, and P. Skvarca. 2004. Glacier acceleration and thinning after ice shelf collapse in the Larsen B embayment, Antarctica. *Geophys. Res. Lett.*, **31**, L18402, doi:10.1029/2004GL020670.
- Schilla, A.S.M., J.W.C. White, B.H. Vaughn, E. J. Brook, K. C. Taylor, M.L. Bender, B. Barnett, E.J. Steig, and R. B. Alley. *In preparation*. The Stable Isotope Record from Siple Dome, West Antarctica: Clues to the Role of Orbital Forcing and El Nino-Southern Oscillation in the Pacific Sector of Antarctica.
- Schilling, S.P., P.E. Carrara, R.A. Thompson, and E.Y. Iwatsubo. 2004. Post eruption glacier development within the crater of Mount St. Helens, Washington, USA. *Quat. Res.*, **61**(3), 325-329.
- Schwerdtfeger, P. 1963. Theoretical derivation of the thermal conductivity and diffusivity of snow. *IASH*, **61**, 75-81.
- Schytt, V. 1958. The inner structure of the ice shelf at Maudheim as shown by core drilling. *Norwegian-British-Swedish Antarctic Expedition, 1949-1952, Scientific Results 4, Glaciology 2*. Norsk Polarinstitut, Oslo, 115-151.
- Shepherd, A., D.J. Wingham and J.A.D. Mansley, 2002. Inland thinning of the Amundsen Sea sector, West Antarctica. *Geophys. Res. Letters*, **29**(10), 1364.

- Shepherd, A., D.J. Wingham, J.A.D. Mansley and H.F.J. Corr, 2001. Inland thinning of Pine Island Glacier, West Antarctica. *Science*, **291**, 862-864.
- Spencer, M.K. 2005. Understanding paleoclimate change through firnification modeling. Ph.D. thesis, The Pennsylvania State University.
- Steig, E.J., J.L. Fastook, C. Zweck, I.D. Goodwin, K.J. Licht, J.W.C. White, and R.P. Akdert. 2001. West Antarctic ice sheet elevation changes. *In* Alley R.B. and R.A. Bindschadler, eds., *The West Antarctic Ice Sheet: Behavior and Environment*, Ant. Res. Series., **77**, 75-90.
- Stone, J.O., G.A. Balco, D.E. Sugden, M.W. Caffee, L.C. Sass III, S.G. Cowdery, C. Siddoway. 2003. Holocene Deglaciation of Marie Byrd Land, West Antarctica. *Science*, **299** (5603), 99-102.
- Taylor, K., R.B. Alley, D.A. Meese, M.K. Spencer, E.J. Brook, N.W. Dunbar, R. Finkle, A.J. Gow, A.V. Kurbatov, G.W. Lamorey, P.A. Mayewski, E.J. Meyerson, K. Nishiizumi, and G.A. Zielinski. 2005. Dating the Siple Dome (Antarctica) ice core by manual and computer interpretation of annual layering. *J. Glaciol.*, **50**(170), 453-461.
- Todd, C., J. Stone, H. Conway, G. Bromley, and B. Hall. Evolution of Reedy Glacier from the Last Glacial Maximum to the present. (abstract) WAIS Workshop, Algonkian State Park, Sterling, VA, Sept. 28-Oct. 1, 2005.
- Tulaczyk, S., B. Kamb and H. Engelhardt. 2000. Basal Mechanics of Ice Stream B, West Antarctica. I. Till Mechanics. *J. Geophys. Res.*, **105**, 463-481.
- U.S. Icecore Working Group, 1992. *In* R.B. Alley ed. Science Plan for WAISCORES deep ice core drilling in West Antarctica. Developed at a workshop convened by the U.S. Icecore Working Group, held at the Rosenstiel School of Marine and Atmospheric Science, University of Miami, October 14-15, 1991

- Vallance, J.W., S.P. Schilling, R. Thompson, and J. Messerich (in press). Growth of the recumbent dome at Mount St. Helens, 2004-2005. in Sherrod, D.A, and Scott, W.E., eds., *A volcano rekindled: the first year of renewed eruption at Mount St. Helens, 2004-05: U.S. Geol. Surv. Prof. Paper.*
- Van der Veen, C.J. 1999. *Fundamentals of Glacier Dynamics*. A.A. Balkema Publishers, Rotterdam, Netherlands.
- Van der Veen, C.J. and I.M. Whillans. 1989. Force Budget: I. Theory and Numerical Methods. *J. Glaciol.*, **35**(119), 53-60.
- Vaughan, D.G., H.F.J. Corr, C.S.M. Doake and E.D. Waddington. 1999. Distortion of isochronous layers in ice revealed by ground-penetrating radar. *Nature*, **398**(6725), 323-326.
- Versteeg, H.K. and W. Malalasekera. 1995. *An introduction to Computational Fluid Mechanics: The Finite Volume Method*. Pearson Education Ltd., Essex, England.
- Waddington, E.D. 1981. *Accurate modeling of glacier flow*. Ph.D. Thesis, University of British Columbia, Department of Geophysics and Astronomy.
- Waddington, E.D., H. Conway, E.J. Steig, R.B. Alley, E.J. Brook, K.C. Taylor, and J.W.C. White. 2005. Decoding the dipstick: Thickness of SDM, West Antarctica, at the Last Glacial Maximum. *Geology*, **33**(4), 281-284.
- Walder, J.S., S.P. Schilling, J.W. Vallance, and R.G. LaHusen (in press). Effects of lava-dome growth on the crater glacier of Mount St. Helens, in Sherrod, D.A, and Scott, W.E., eds., *A volcano rekindled: the first year of renewed eruption at Mount St. Helens, 2004-05: U.S. Geol. Surv. Prof. Paper.*
- Walder, J.S., S.P. Schilling, J.W. Vallance, and R.G. LaHusen (in press). Effects of lava-dome growth on the crater glacier of Mount St. Helens. *Ann Glaciol.*
- Wang, W.L. and R. C. Warner. 1999. Modelling of anisotropic ice flow in Law Dome, East Antarctica. *Ann. Glaciol.*, **29**, 184-190.

- Wang, W.L. H.J. Zwally, C.L. Hulbe, M.J. Siegert, and I. Joughin. 2003. Anisotropic ice flow leading to the onset of Ice Stream D, West Antarctica: numerical modeling based on the observations from Byrd Station borehole. *Ann. Glaciol.*, **39**, 397-403.
- Weertman, J. 1957. On the sliding of glaciers. *J. Glaciol.* **3**(21), 33-38.
- Whillans, I.M. and S.J. Johnsen. 1983. Longitudinal variations in glacial flow: theory and test using data from the Byrd Station Strain Network, Antarctica. *J. Glaciol.*, **29** (101), 78-97.
- Zumberge, M.A., D.H. Elsberg, W.D. Harrison, E. Husmann, J.L. Morack, E.C. Pettit, and E.D. Waddington. 2002. Measurement of vertical strain rate and velocity at Siple Dome, Antarctica, with optical sensors. *J. Glaciol.*, **48**(161), 217-225.
- Zwally, H.J., W. Abdalati, T. Herring, K. Larson, J. Saba, K. Steffen. 2002. *Science*. **297**(5579), 218-222.

APPENDIX A

DISCRETE, ORTHOGONAL, CURVILINEAR COORDINATE SYSTEM**The fundamental equation for orthogonal trajectories**

Expanding Equation (34) in Chapter 2 with g_{ij} associated with $(x_1, x_2) = (x, \hat{z})$ (the non-orthogonal, *initial* coordinates) and with \bar{g}_{lk} associated with $(y_1, y_2) = (\hat{x}, \hat{z})$ (the orthogonal, *final* coordinates) gives

$$g_{11} \frac{\partial x}{\partial \hat{x}} \frac{\partial x}{\partial \hat{z}} + g_{12} \left(\frac{\partial x}{\partial \hat{x}} \frac{\partial \hat{z}}{\partial \hat{z}} + \frac{\partial \hat{z}}{\partial \hat{x}} \frac{\partial x}{\partial \hat{z}} \right) + g_{22} \frac{\partial \hat{z}}{\partial \hat{x}} \frac{\partial \hat{z}}{\partial \hat{z}} = 0. \quad (\text{A1})$$

In the new, orthogonal coordinate system we require that $\frac{\partial \hat{z}}{\partial \hat{x}} = 0$ (i.e. the \hat{x}, \hat{z} coordinate curves are perpendicular and thus independent from one another), in which case Equation (A1) becomes

$$\left(g_{11} \frac{\partial x}{\partial \hat{z}} + g_{12} \frac{\partial \hat{z}}{\partial \hat{z}} \right) \frac{\partial x}{\partial \hat{x}} = 0. \quad (\text{A2})$$

Dividing through by $\frac{\partial x}{\partial \hat{x}}$ gives

$$g_{11} \frac{\partial x}{\partial \hat{z}} + g_{12} \frac{\partial \hat{z}}{\partial \hat{z}} = 0, \quad (\text{A3})$$

which, when we note that $\frac{\partial \hat{z}}{\partial \hat{z}} = 1$, becomes

$$\frac{\partial x}{\partial \hat{z}} = \frac{-g_{12}}{g_{11}}. \quad (\text{A4})$$

Equation (A4) is equivalent to Equation (38) in Chapter 2, the fundamental equation for orthogonal trajectories. By Equation (36) in Chapter 2, the tangent vectors in the non-orthogonal, initial coordinate system are given by

$$\frac{\partial \mathbf{r}}{\partial x} = \frac{\partial}{\partial x} (x, \hat{z} \cdot (s(x) - b(x)) + b(x)) = (1, \hat{z} \cdot (s' - b') + b') = \mathbf{e}_1 \quad (\text{A5})$$

and

$$\frac{\partial \mathbf{r}}{\partial \hat{z}} = \frac{\partial}{\partial \hat{z}} (x, \hat{z} \cdot (s(x) - b(x)) + b(x)) = (0, s - b) = \mathbf{e}_2, \quad (\text{A6})$$

where primes denote derivatives w.r.t. x . Through Equation (35) in Chapter 2, Equations (A5) and (A6) provide the numerator and denominator on the RHS of Equation (A4),

$$g_{11} = \mathbf{e}_1 \cdot \mathbf{e}_1 = 1 + (\hat{z} \cdot (s' - b') + b')^2 \quad (\text{A7})$$

and

$$-g_{12} = -\mathbf{e}_1 \cdot \mathbf{e}_2 = (\hat{z} \cdot (s' - b') + b')(s - b). \quad (\text{A8})$$

The ratio of Equation (A8) and (A7) gives Equation (39), the integrand needed for obtaining the \hat{z} coordinate curves.

Discrete orthogonality

For flux balance between neighboring volumes, gradients in the dependent variable at an interface must be characterized entirely by the values that variable takes on at its profile endpoints. With respect to a discrete grid, this is equivalent to requiring that the line segment describing the orientation of an interface be orthogonal to the line segment connecting the two volume center points that share that interface. Figure A1 illustrates this concept. The grid point $(x, z)_{ij}$ denotes an interface center that is common to the two volumes with centers at $(x, z)_{i-1, j}$ and $(x, z)_{i+1, j}$. In the discrete sense, the grid points $(x, z)_{i, j-1}$ and $(x, z)_{i, j+1}$ define the east face of the

volume centered at $(x,z)_{i-1,j}$ and the west face of the volume centered at $(x,z)_{i+1,j}$. Orthogonality at the common interface center, $(x,z)_{i,j}$, requires that unit vectors paralleling the line segments defined by points $(x,z)_{i+1,j}$ and $(x,z)_{i-1,j}$, and points $(x,z)_{i,j+1}$ and $(x,z)_{i,j-1}$, have a dot product of 0. We define this condition as “discrete orthogonality”. The staggered grid requirement (Figure 1) then results in the overall requirement that each internal grid point obey discrete orthogonality. Individual volumes within the grid are then each defined by a total of 9 grid points: 4 corner points, 4 interface center points, and one center point. The positions of these points are constrained by orthogonality and by the locations of points defining neighboring volumes.

We note that our definition for “discrete orthogonality” is very similar to Eisman’s (1982) definition for “central-difference orthogonality”. In the event that uniform grid spacing is used, the two definitions are identical. The procedure described herein would then also be suitable for generating orthogonal, curvilinear grids for finite-difference schemes.

Integration of the fundamental equation

The \hat{z} coordinate curves are obtained by integrating the fundamental equation between \hat{x} coordinate curves (curves of constant \hat{z}). The integration scheme used here is a modified Euler-predictor-corrector,

$$\mathbf{x}_{j+1} = \mathbf{x}_{j-1} + \mathbf{a}(\hat{z}_{j+1} - \hat{z}_{j-1}), \quad (\text{A9})$$

where \mathbf{x}_{j+1} and \mathbf{x}_{j-1} are row vectors of final and initial x coordinates, respectively, and \mathbf{a} is a row vector describing the direction of travel in (x,z) space, from \mathbf{x}_{j-1} to \mathbf{x}_{j+1} . Equation (A9) is a discrete, vector form of Equation (40) in Chapter 2. The subscript j indicates which \hat{x} coordinate curve the set of x coordinates lie upon. For example, the row vector of initial points \mathbf{x}_{j-1} lies on the curve \hat{x}_{j-1} (defined by

$\hat{z}_{j-1}=C_{-1}$). The solution to the integration is the row vector \mathbf{x}_{j+1} , which has a vector of corresponding z coordinates given by

$$\mathbf{z}_{j+1} = \hat{z}_{j+1} \left[\mathbf{s}(\mathbf{x}_{j+1}) - \mathbf{b}(\mathbf{x}_{j+1}) \right] + \mathbf{b}(\mathbf{x}_{j+1}), \quad (\text{A10})$$

the vector analog of Equation (33) in Chapter 2. Given some starting \mathbf{x}_{j-1} , the goal is to determine the location of \mathbf{x}_{j+1} such that our definition of discrete orthogonality is obeyed at the intermediate points given by $\mathbf{x}_j, \mathbf{z}_j$.

To meet this requirement, the “slope” vector \mathbf{a} , with components a_i , is weighted according to

$$a_i = w_i \left. \frac{\partial x}{\partial \hat{z}} \right|_{i,j-1} + (1 - w_i) \left. \frac{\partial x}{\partial \hat{z}} \right|_{i,j+1}. \quad i=1, 2, 3, \dots, k \quad (\text{A11})$$

The index i indicates which of the k \hat{z} coordinate curves we are integrating along and the values for $\left. \frac{\partial x}{\partial \hat{z}} \right|$ at any index i are given by Equation (39) in Chapter 2. The weight, w_i , takes on a value between 0 and 1. For $w_i=1$, Equation (A9) becomes a simple Euler-predictor. This is the value used for “shooting” off of the lowermost domain boundary, the \hat{x} coordinate curve defined by $b(x)$ and coinciding with $\hat{z}=0$. Along this boundary the initial values for \mathbf{x} are known (specified) and there is no curve $\hat{z}_{j-1}=C_{-1}$. For this initial step, Equations (A9) and (A10) are modified by substituting j for $j+1$. The vectors we obtain after this step, \mathbf{x}_j and \mathbf{z}_j , define the locations of all volume centers and interface centers along the lowermost row of volumes in the grid (Figure A2). From this set of points, the next row (Figure A3) of points, and all rows of remaining points defining the \hat{z} curves are found as follows:

- (1) With all $w_i=0.5$, Equations (A9), (A10), and (A11) are used to predict a “trial” location for the points $\mathbf{x}_{j+1}, \mathbf{z}_{j+1}$.

(2) A vector of discrete-dot products, \mathbf{d}_j , is calculated for the points $\mathbf{x}_j, \mathbf{z}_j$. For an internal grid point $(x_{i,j}, z_{i,j})$, the intersection of curves \hat{x}_i and \hat{z}_j , this calculation is based on the line segment connecting the points (x_j, z_{j+1}) and (x_j, z_{j-1}) and the line segment connecting the points (x_{j+1}, z_j) and (x_{j-1}, z_j) (as in Figure A1). For points along a domain boundary this calculation is done similarly but uses mixed centered and one-sided differences (e.g. at the bottom boundary we calculate a centered difference in x and a forward difference in z).

(3) An orthogonality tolerance, ϵ , is chosen. Here, we have arbitrarily chosen a value of 10^{-10} . If any point, d_i , within the vector \mathbf{d}_j is such that $|d_i| > \epsilon$, a Newton-Raphson iteration is used to find the perturbation necessary to adjust the appropriate x_i within the \mathbf{x}_{j+1} vector (and thus to also adjust the appropriate z_i in the \mathbf{z}_{j+1} vector) so that $|d_i| \leq \epsilon$. Thus, Equations (A9)-(A11) are iterated on until the points $\mathbf{x}_{j+1}, \mathbf{z}_{j+1}$ satisfy $|\mathbf{d}_j| \leq \epsilon$ for the points $\mathbf{x}_j, \mathbf{z}_j$.

(4) The calculation advances and continues by (i) replacing the points $\mathbf{x}_j, \mathbf{z}_j$ with the points $\mathbf{x}_{j+1}, \mathbf{z}_{j+1}$, (ii) replacing the points $\mathbf{x}_{j-1}, \mathbf{z}_{j-1}$ with the points for $\mathbf{x}_j, \mathbf{z}_j$, and (iii) returning to step (1) above and predicting a new trial location for the points $\mathbf{x}_{j+1}, \mathbf{z}_{j+1}$.

The above procedure applies to all internal grid points. No separate calculation is needed for the final row of coordinates, since these will simply be the last set of $\mathbf{x}_{j+1}, \mathbf{z}_{j+1}$ coordinates to be calculated and adjusted for orthogonality.

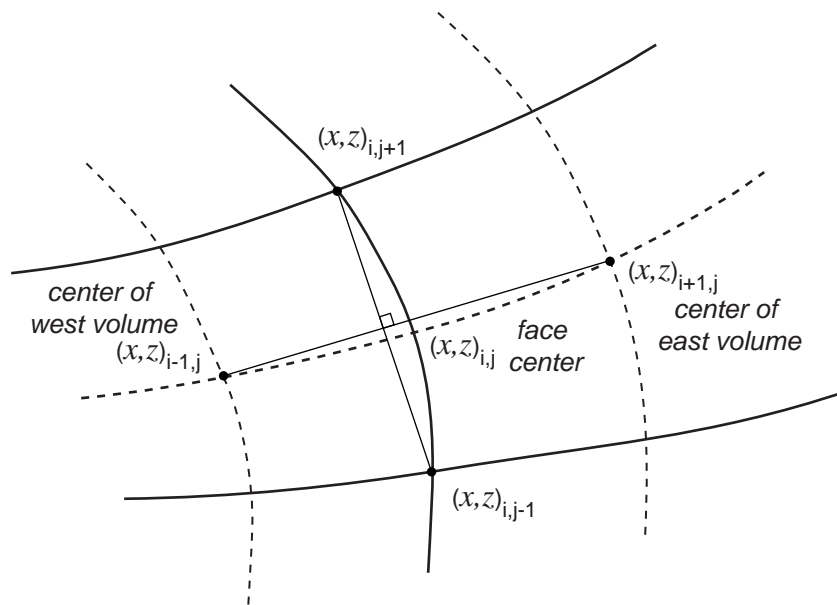


Figure A.1: Illustration of discrete orthogonality at interface $(x, z)_{i,j}$. The interface $(x, z)_{i,j}$ is shared by the finite volumes at the points $(x, z)_{i-1,j}$ and $(x, z)_{i+1,j}$.

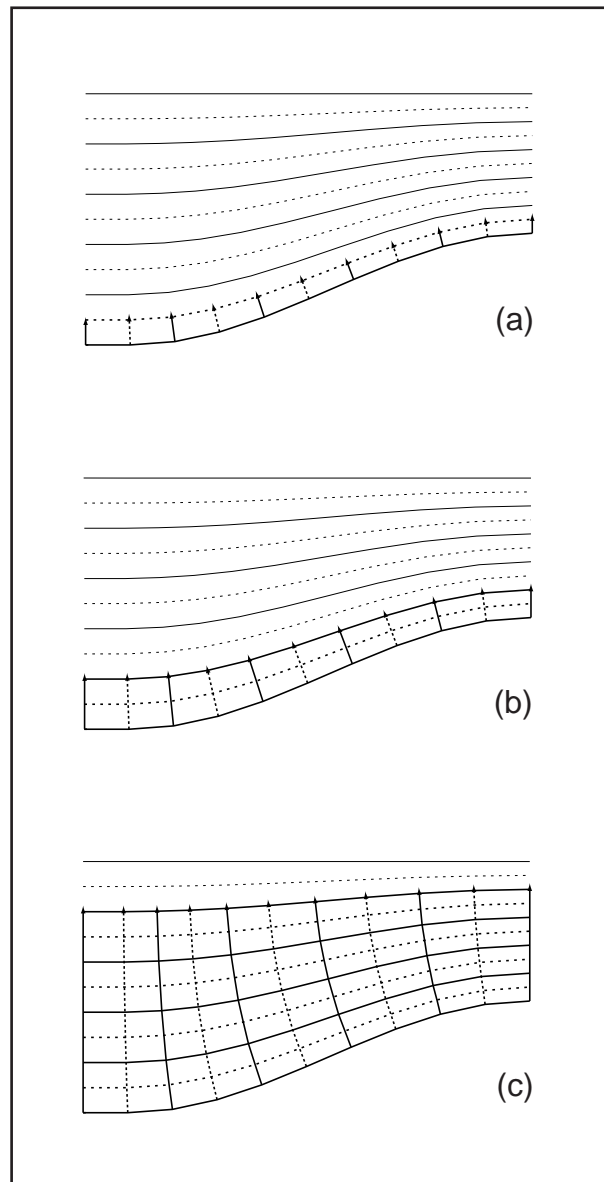


Figure A.2: Section of a curvilinear grid demonstrating integration procedure. (a) First integration, starting from the lowermost domain boundary, $b(x)$ ($\hat{z}=0$). After the first integration the volume centers and interface centers have been defined for the lowermost row of volumes in the grid. (b) Second integration, after which the upper corners and upper interface centers are defined for the lowermost row of volumes in the grid. (c) Further integrations, which define successively higher rows of volumes in the grid.

NON-STEADY AND ADVECTIVE TERMS

Non-steady term

Including the non-steady term in Equation (21) in Chapter 2 requires that we also integrate over the time step, Δt . For the case of no advection ($u=w=0$), Equation (21) in Chapter 2 becomes

$$\rho \Delta z \Delta x (\phi_P^1 - \phi_P^0) = \int_t^{t+\Delta t} \left[\Gamma_e \left(\frac{\phi_E - \phi_P}{\delta x_e} \right) \Delta z - \Gamma_w \left(\frac{\phi_P - \phi_E}{\delta x_w} \right) \Delta z + \dots + \bar{S} \Delta x \Delta z \right] dt, \quad (B1)$$

where superscripts indicate the value of ϕ at the current time (ϕ^0) and some future time (ϕ^1). As with the spatial discretization, we must make some assumption for how the dependent variables on the RHS of Equation (B1) vary over the time step. A reasonable approach is to assume a linear variation, for example

$$\int_t^{t+\Delta t} \phi_P dt = [\beta \phi_P^1 + (1 - \beta) \phi_P^0] \Delta t, \quad (B2)$$

where $0 \leq \beta \leq 1$ is an interpolation weight. Substituting this expression, similar expressions for the neighboring values of ϕ , and coefficient definitions analogous to those in Equations (25) in Chapter 2 gives

$$\begin{aligned} a_P \phi_P = & a_E [\beta \phi_E + (1 - \beta) \phi_E^0] + a_W [\beta \phi_W + (1 - \beta) \phi_W^0] + a_U [\beta \phi_U + (1 - \beta) \phi_U^0] + \dots \\ & \dots + a_D [\beta \phi_D + (1 - \beta) \phi_D^0] + b \end{aligned} \quad (B3).$$

In Equation (B3) the superscript “1” has been dropped with the understanding that an unmarked variable refers to the value that a variable takes on at the future time step. In Equation (B3) we have also assumed several new definitions including

$$b \equiv \bar{S} \Delta x \Delta z + a_P^0 \phi_P^0, \quad (\text{B4})$$

$$a_P^0 \equiv \frac{\rho \Delta x \Delta z}{\Delta t}, \quad (\text{B5})$$

and

$$a_P \equiv a_E + a_W + a_U + a_D + a_P^0. \quad (\text{B6})$$

For $\beta=0$, 0.5, or 1, Equation (B3) reduces to one of three commonly used forms for forward-time marching when solving parabolic, partial-differential equations. $\beta=0$ results in the explicit scheme, $\beta=0.5$ results in the semi-implicit, “Crank-Nicholson” scheme, and $\beta=1$ results in the fully-implicit scheme. Here, we choose the fully-implicit scheme, such that in all Equations like Equation (B3), $\beta=1$.

Advective-diffusive flux

When treating the advective term in Equation (21) in Chapter 2, it is convenient to first combine the advective and diffusive fluxes into a single flux term,

$$J_i = \rho u_i \phi - \Gamma \frac{\partial \phi}{\partial x_i}, \quad (\text{B7})$$

in which case the steady form of Equation (21) in Chapter 2 is given by

$$\frac{\partial J_i}{\partial x_i} = S. \quad (\text{B8})$$

Integration of Equation (B8) over the shaded finite volume shown in Figure 2 gives

$$J_e \Delta z_e - J_w \Delta z_w + J_u \Delta x_u - J_d \Delta x_d = \bar{S} \Delta x_p \Delta z_p. \quad (\text{B9})$$

For an orthogonal coordinate system, the flux across the interfaces is “one-dimensional”: no interface-parallel velocity components or gradients are required to quantify the interface flux. In this case, and assuming a known flow field (see Appendix C for further discussion on solving the momentum equations), the analytical expression for the advective-diffusive flux across interface e in Figure 2 is

$$J_e = F_e \left(\phi_P + \frac{\phi_P - \phi_E}{\exp(Pe_e) - 1} \right) \quad (\text{B10})$$

(Patankar, 1980). Pe_e is the Peclet number at interface e , given by

$$Pe_e = \frac{F_e}{D_e} = \frac{\rho u_e \Delta z_e}{\Gamma_e \delta x_e^{-1} \Delta z_e}, \quad (\text{B11})$$

the ratio of the advective (F_e) and diffusive (D_e) mass-flow rates across interface e .

Because calculation of the exponential term in Equation (B10) is computationally intensive, it is beneficial to use a simpler, approximating function instead. An alternative that provides an excellent fit to the actual expression is the “power-law” approximation of Patankar (1980),

$$J_e = F_e \phi_P + \left[D_e A_e(|Pe_e|) + \|-F_e, 0\| \right] (\phi_P - \phi_E), \quad (\text{B12})$$

where

$$A_e(|Pe_e|) = \left\| 0, (1 - 0.1|Pe_e|)^5 \right\|. \quad (\text{B13})$$

In Equations (B12) and (B13), $\|a, b\|$ denotes that the larger of the two values, a or b , is to be used when evaluating the enclosed expression. The variable A_e is simply

the area of the interface at e . The advective-diffusive flux at interfaces w , u , and d are evaluated from similar expressions.

Final discretization equation

Including the non-steady and advective terms in the discretized, two-dimensional equation for the scalar variable ϕ gives

$$a_P \phi_P = a_W \phi_W + a_E \phi_E + a_D \phi_D + a_U \phi_U + b, \quad (\text{B14})$$

where

$$a_E = D_e A_e (|Pe_e|) + \|-F_e, 0\|, \quad (\text{B15a})$$

$$a_W = D_w A_w (|Pe_w|) + \|F_w, 0\|, \quad (\text{B15b})$$

$$a_U = D_u A_u (|Pe_u|) + \|-F_u, 0\|, \quad (\text{B15c})$$

and

$$a_D = D_d A_d (|Pe_d|) + \|F_d, 0\|. \quad (\text{B15d})$$

a_P and b are as defined in Equations (B4-B6).

In Equation (B15), the advective and diffusive mass-flow rates per unit time are given by

$$F_w = \rho u_w \Delta z_w, \quad F_e = \rho u_e \Delta z_e, \quad F_u = \rho w_u \Delta x_u, \quad F_d = \rho w_d \Delta x_d, \quad (\text{B16, a-d})$$

and

$$D_w = \frac{\Gamma_w \Delta z_w}{\delta x_w}, \quad D_e = \frac{\Gamma_e \Delta z_e}{\delta x_e}, \quad D_u = \frac{\Gamma_u \Delta x_u}{\delta z_u}, \quad D_d = \frac{\Gamma_d \Delta x_d}{\delta z_d}, \quad (\text{B17, a-d})$$

and the Peclet numbers are given by

$$Pe_w = \frac{F_w}{D_w}, \quad Pe_e = \frac{F_e}{D_e}, \quad Pe_u = \frac{F_u}{D_u}, \quad Pe_d = \frac{F_d}{D_d}. \quad (\text{B18, a-d})$$

APPENDIX C

PRESSURE-CORRECTION METHOD

In general, the pressure field is not known *a priori* and must be solved for like the unknown velocity fields. Following Patankar (1980), the pressure and velocity fields are solved for iteratively using a pressure-correction algorithm (the SIMPLE algorithm, for “Semi-Implicit Method for Pressure Linked Equations”).

Starting with a guessed pressure field, P^* , the discretized equations for u and w (Equation (30) in Chapter 2 and its counterpart for the vertical velocity field) are solved to obtain guessed velocity fields, u^* and w^* . A correction to the guessed pressure field, P' , gives corrections to the guessed velocities, u' and w' , and results in updated estimates

$$P = P^* + P', \quad u = u^* + u', \quad w = w^* + w'. \quad (\text{C1, a-c})$$

In terms of guessed pressures and velocities, Equation (29) in Chapter 2 is

$$a_p u_p^* = \sum_1^m a_m u_m^* - (P_e^* - P_w^*) \Delta z_p + \bar{B}_x \Delta z_p \Delta x_p. \quad (\text{C2})$$

Subtracting Equation (C2) from Equation (29) in Chapter 2 gives the following expression for u' ,

$$a_p u_p' = \sum_1^n a_n u_n' - (P_e' - P_w') \Delta z_p. \quad (\text{C3})$$

In Equation (C2) and (C3) we have used lowercase subscripts to emphasize that the pressures apply at the *interfaces* of the u and w calculation volumes. If we, for the

moment, ignore the first set of terms on the RHS of Equation (C3) (this omission is discussed further below) we have

$$a_p u'_p = -(P'_e - P'_w) \Delta z_p, \quad (C4)$$

which can be rearranged to

$$u'_p = -(P'_e - P'_w) \frac{\Delta z_p}{a_p} = -(P'_e - P'_w) d_p^u. \quad (C5)$$

The ratio $\Delta z_p/a_p$ defines the coefficient d_p^u , where the subscript and superscript on d indicates that the a_p and Δz_p values are those associated with the velocity calculation volume, u_p . The coefficient d_p^u serves as constant of proportionality between a pressure perturbation and the corresponding perturbation to the velocity field. Substituting Equation (C5) into Equation (C1b) gives

$$u_p = u_p^* - (P'_e - P'_w) d_p^u, \quad (C6)$$

an expression for the corrected velocity u_p . A similar expression is derived for the vertical component of velocity,

$$w_p = w_p^* - (P'_u - P'_d) d_p^w. \quad (C7)$$

The right-hand sides of Equations (C6) and (C7) describe the velocity correction at an interface as a function of the bounding pressure corrections. Still needed is an expression for the pressure correction itself, as a function of the velocity field. The link between the two is Equation (3) in Chapter 2, the incompressibility condition. In 2D ($\partial v/\partial y=0$), integration of Equation (3) in Chapter 3 over the shaded finite volume in Figure 2 gives

$$(u_e - u_w)\Delta z_p + (w_u - w_d)\Delta x_p = 0. \quad (\text{C8})$$

where the lowercase subscripts indicate velocities that apply at pressure volume interfaces. Substituting the appropriate interface velocities from Equations (C6) and (C7) into Equation (C8) gives

$$a_p P'_p = a_E P'_E + a_W P'_W + a_U P'_U + a_D P'_D + S. \quad (\text{C9})$$

In Equation (C9), uppercase subscripts indicate that we are referencing values that apply at the centers of pressure calculation volumes.

The coefficients in Equation (C9) are given by

$$a_E = \rho d_e^u \Delta z_e, \quad a_W = \rho d_w^u \Delta z_w, \quad a_U = \rho d_u^w \Delta x_u, \\ a_D = \rho d_d^w \Delta x_d, \quad a_p = a_E + a_W + a_U + a_D. \quad (\text{C10,a-e})$$

As with the interface velocities, the $j \times k$ arrays for Δx , Δz , and d^* at interfaces are obtained by sub-sampling the appropriate rows (or columns) from the larger arrays (for example, d_w^u consists of the first j columns from the array d_p^u and d_u^w consists of the last k rows of the array d_p^w).

The source term in Equation (C9) is the integrated continuity equation based on the guessed velocities,

$$S = (u_e^* \Delta z_e - u_w^* \Delta z_w) + (w_u^* \Delta x_u - w_d^* \Delta x_d). \quad (\text{C11})$$

S has units of mass per unit time and represents the degree to which the guessed velocity fields satisfy continuity. Volumes that serve as mass sources (or sinks) have $S \neq 0$ and thus $P' \neq 0$. Successive iterations of the linked pressure and velocity equations, in which the corrected velocity field becomes the guessed velocity field

at the start of the next iteration, move the guessed pressure and velocity fields towards satisfying continuity. When the guessed velocity field satisfies the continuity equation for every volume, $S=0$, $P'=0$, as do u' and w . When $P'=0$, the pressure and velocity fields do not change with further iterations and a converged solution has been reached. In practice, iterations are halted after the maximum mass residual within all of the individual volumes has fallen below some threshold value.

If $P'_e = P'_w$ in Equation (C6), the velocity perturbation will be zero. Thus, when the velocity at a boundary is specified, a zero-gradient is the necessary boundary condition on P' . If the pressure at a boundary is to be specified then the value of the pressure perturbation at that boundary is set to 0.

The pressure-correction procedure can be summarized as follows:

- (1) Guess a pressure field (e.g. hydrostatic pressure).
- (2) Using the current, guessed pressure field, calculate a guessed velocity field.
- (3) Integrate the continuity equation to obtain the pressure-correction source term.
- (4) Solve for the pressure correction (Equation (C9)).
- (4) Correct the pressure and velocity fields (Equations (C1a), (C6) and (C7)).
- (5) Integrate the continuity equation using the corrected velocity field.
- (6) Check if the pressure-correction source term is ~ 0 .
 - (a) If yes, the current pressure and velocity fields have converged.

(b) If no, return to step (2) and continue iterating.

Relaxation

If the change in a dependent variable between iterations is too large, the solution may diverge or oscillate indefinitely, rather than converge. In this case, *relaxation* may be necessary to damp the change in a dependent variable from one iteration to the next. For example, consider the pressure perturbation written as

$$P' = \lambda P'_{new} + (1 - \lambda) P'_{old}, \quad (C12)$$

where the subscripts denote values calculated during the current (new) and previous (old) iterations. For $0 < \lambda < 1$, the changes in the pressure perturbation will be *under-relaxed*; they will be more gradual than without relaxation. Under-relaxation is commonly employed to avoid a diverging solution. The pressure-correction method discussed above generally requires under-relaxation to both the pressure ($\lambda \sim 0.5$) and velocity perturbations ($\lambda \sim 0.8$). Further discussion on the implementation of relaxation is given in Patankar (1980).

An Alternate, Improved Solution Method

The pressure-correction method described above ignores the fact that the velocity correction in any volume depends not only on the pressure correction in neighboring volumes, but also on the velocity corrections in neighboring volumes (hence the “Semi-IMplicit” in SIMPLE). This omission is allowable because the method leads to a set of pressure and velocity fields that satisfy continuity and thus, the governing equations. This simplification, however, has important, negative consequences. Because the velocity field must be corrected by changes in the pressure field alone, the resulting pressure corrections are large and, quite often, lead to a diverging solution. The remedy is a large degree of under-relaxation to

changes in the pressure field. A converged solution is reached but strong under-relaxation results in very slow convergence.

An improvement to the SIMPLE algorithm, the SIMPLER (“SIMPLE-Revised”) algorithm (Patankar, 1980), acknowledges and corrects for this shortcoming. If we first divide Equation (29) in Chapter 2 by the coefficient a_p we obtain

$$u_p = \frac{\sum_1^n a_n u_n + \bar{B}_x \Delta x_p \Delta z_p}{a_p} - \frac{(P_e - P_w) \Delta z_p}{a_p}. \quad (\text{C13})$$

If we then define

$$\hat{u}_p = \frac{\sum_1^n a_n u_n + \bar{B}_x \Delta x_p \Delta z_p}{a_p}, \quad (\text{C14})$$

Equation (C14) can be written as

$$u_p = \hat{u}_p - (P_e - P_w) d_p'', \quad (\text{C15})$$

in which the first term on the RHS is the “pseudo-velocity” (the velocity that would exist in the absence of the pressure field). The coefficient d_p'' is the same as defined above in Equation (C5). Equation (C15) and its counterpart for the vertical component of velocity, w , have the same form as Equations (C6) and (C7) above. When these expressions are inserted into the integrated continuity, Equation (C8), we obtain an equation for the pressure field itself,

$$a_p P_p = a_E P_E + a_W P_W + a_U P_U + a_V P_V + S, \quad (\text{C16})$$

where the coefficients are the same as those given in Equations (C10). Similar to Equation (C11) above, the source term for the pressure equation is

$$S = (\hat{u}_e \Delta z_e - \hat{u}_w \Delta z_w) + (\hat{w}_u \Delta x_u - \hat{w}_d \Delta x_d), \quad (C17)$$

the integrated continuity equation based on the interface pseudo-velocities.

Unlike SIMPLE, where the initial pressure field is guessed, the SIMPLER method calculates the initial pressure field from Equation (C16) (and thus requires an initial guess for the pseudo-velocity fields in Equation (C17)). After calculating the pressure field, SIMPLER proceeds in a manner very similar to SIMPLE: (1) The u and w velocity fields are calculated, (2) P' , u' and w' are calculated, and (3) the velocity field is corrected via $u'(P')$ and $w'(P')$. Unlike SIMPLE, however, the pressure field is not corrected. Rather, the corrected velocity field gives updated pseudo-velocities and an updated pressure field for use during the following iteration. Because the pressure field is not corrected with P' , the pressure corrections *do not* require under-relaxation ($\lambda=1$) and the velocity corrections require only *minor* relaxation ($\lambda \sim 0.95$). In general, SIMPLER reduces computation time by ~ 30 - 50% , relative to SIMPLE (Versteeg and Malalasekera, 1995, p.154). Because of this, SIMPLER is the solution algorithm currently implemented within the momentum balance model described above.

For geometries, pressures, viscosities, and velocities relevant to a polar ice sheet, it was found that SIMPLER would not consistently converge to within an arbitrarily chosen degree of accuracy (i.e. convergence halted or became impractically slow near some number >0). Because the magnitude of the pressure field is many orders of magnitude larger than other model fields, it is thought that non-convergence was due to the accumulation of large round-off errors. This problem was overcome by first non-dimensionalizing the momentum equations in the manner suggested by Raymond (1983).

APPENDIX D

FLOWBAND ADAPATION

The model described above was developed with the assumption that the momentum and continuity equations are invariant in the across-flow direction. A simple improvement can be made to adapt this “flowline” (plain strain) formulation to a “flowband” formulation, which allows for the effects of converging or diverging flow. For a flowband with width varying only as a function of the along-flow coordinate, $W=W(x)$, the across-flow gradient in velocity is given by

$$\frac{\partial}{\partial y} v(x,z) = \frac{u(x,z)}{W(x)} \frac{\partial}{\partial x} W(x) \quad (\text{D1})$$

(Waddington, 1981), where v is the across-flow component of velocity. Here, we are not concerned with v itself so much as the across-flow gradient in v , $\dot{\epsilon}_{yy}$, which is given by the LHS of Equation (D1). Thus, Equation (D1) allows us to include the effects of converging or diverging flow in our definition of the effective strain rate, $\dot{\epsilon}_e$ (Equation (6) in Chapter 2). For a flowband of constant width, $\dot{\epsilon}_{yy}=0$ and the flowband and flowline formulations are identical.

Several other minor adjustments are necessary when including a variable flowband width. First, coefficients defined in Equation (25) in Chapter 2 must be multiplied by an additional factor, which is simply the width of the individual finite volume. For example, the coefficient a_E would be defined as

$$a_E = \frac{\eta_e \Delta z}{\delta x_e} W_e, \quad (\text{D2})$$

where W_e is the (defined) width at the east face of the shaded volume centered at P in Figure 2. Similar adjustments are made to coefficients defined in Equation (C10). Second, the guessed (pseudo-) velocities on the RHS of Equation (C11) (Equation (C17)), the source term for the pressure correction (pressure), must also be multiplied by their respective interface widths. Equation (C11) becomes

$$S = \left([u^* W \Delta z]_e - [u^* W \Delta z]_w \right) + \left([w^* W \Delta x]_u - [w^* W \Delta x]_d \right), \quad (\text{D3})$$

where subscripts indicate that all values enclosed by brackets apply at their respective interfaces. Lastly, the specified flux boundary condition must be altered so that the surface accumulation rate is integrated over the flowband length *and* width. In this case, the column-averaged velocity at the eastern boundary, Equation (18) in Chapter 2, becomes

$$\bar{u}_e = \frac{1}{H_e W_e} \int_{x=0}^{x=e} \dot{b}(x) W(x) dx, \quad (\text{D4})$$

where W_e is the flowband width at the eastern boundary.

APPENDIX F

**UNCERTAINTY IN SURFACE TEMPERATURE HISTORY AT SIPLE
 DOME AND THE RESULTING UNCERTAINTY IN MODELED
 TEMPERATURES**

We estimate an uncertainty of $\sim 0.5^\circ\text{C}$ for modeled temperatures at depth based on the model response to perturbations in the surface temperature history. The surface-temperature history is derived from the stable-isotope profile measured along the SDM ice core (Schilla and others, in prep.) using a relation of the form

$$T_S = T_{S0} + (\alpha \cdot \Delta\delta D + \beta), \quad (\text{F1})$$

where T_S is the surface temperature at some time in the past and the terms in parentheses on the right-hand side represent a temperature change relative to T_{S0} , the modern day surface temperature at SDM. The temperature change is calculated as a function of δD , the isotopic ratio of Deuterium measured in precipitation at the core site and α , the “slope” that describes the rate of temperature change per unit change in δD . β accounts for 2nd order corrections to the calculated temperature change, such as those resulting from changes in isotopic concentration at the precipitation source. In general, α is treated as a constant, which is calculated from the modern-day observations of the relationship between surface temperature and δD . In reality, α varies spatially (e.g. Kavanaugh and Cuffey, 2003) and temporally. Jouzel and others (2003) suggest an uncertainty on the order of ± 10 to 20% when applying spatial estimates of α to temperature changes over time. Cuffey and others (1994) estimated that the value changed by a factor of 2 across the glacial-interglacial transition in central Greenland.

To estimate how these uncertainties might affect the surface temperature history at SDM, we use Equation (A1) with $\alpha=8 \times (1.45^{-1})$ and $\beta=0$ to approximate

the surface temperature history of Schilla and others (in prep.). In general, this approximation matches the actual temperature history to within a fraction of a degree. We then assume an uncertainty in the value of α between 20-50%, from which we estimate an uncertainty in the magnitude of ice-age temperatures between 2-4°C. By adding or subtracting 2°C to glacial temperatures, we find that the change in the modeled, modern-day temperature profile is $\leq |0.5^\circ\text{C}|$.

VITA

Stephen F. Price

June 16, 2006

EDUCATION

B.S. (1995), Geological Sciences, The University of North Carolina at Wilmington

M.S. (1998), Geological Sciences, The Ohio State University

Ph.D. (2006), Geophysics, The University of Washington

RESEARCH EXPERIENCE

Research Assistant, The Department of Geological Sciences *and* Byrd Polar
Research Center, The Ohio State University (1/96-9/98)

Programmer/Analyst, SAIC General Sciences Corporation, NASA Goddard Space
Flight Center (9/98-6/01)

Research Assistant, The Department of Earth and Space Sciences, The University
of Washington (6/01-6/06)

TEACHING EXPERIENCE

Teaching Assistant, Juneau Icefield Research Program, University of Idaho and
University of Alaska, S.E., (6/96 - 8/96)

Teaching Assistant, The Department of Earth and Space Sciences, The University
of Washington (6/01-6/06)

PUBLICATIONS

Price, S.F., R.A. Bindschadler C.L. Hulbe, and D.D. Blankenship. 2002. Force
balance along an inland tributary and onset to Ice Stream D, West
Antarctica. *J. Glaciol.* **48**(160), 20-30.

- Price, S.F., R.A. Bindschadler, C.L. Hulbe and I. Joughin. 2001. Post-stagnation behavior in the upstream regions of Ice Stream C, West Antarctica. *J. Glaciol.*, **47**(157), 283-294.
- Price, S.F. and I.M. Whillans. 2001. Crevasse patterns at the onset to Ice Stream B, West Antarctica. *J. Glaciol.*, **47**(156), 29-36.
- Price, S.F. and I.M. Whillans. 1998. Delineation of a catchment boundary using velocity and elevation measurements. *Ann. Glaciol.*, **27**, 140-144.
- Price, S.F. 1998. Studies in the catchment and onset regions of Ice Stream B, West Antarctica. (masters thesis, The Ohio State University.)
- Joughin, I., L. Gray, R. Bindschadler, S. Price, D. Morse, C. Hulbe, K. Mattar and C. Werner. 1999. Tributaries of West Antarctic ice streams revealed by Radarsat interferometry. *Science*, **286** (5438), 283-286.
- Joughin, I., S. Tulaczyk, R.A. Bindschadler, S.F. Price. 2002. Changes in west Antarctic ice stream velocities: Observation and analysis, *J. Geophys. Res.*, **107**(B11), 2289, doi:10.1029/2001JB001029.